# EFFECTS OF LOW DIMENSIONALITY ON PROPERTIES OF THERMOELECTRICS AND STRONGLY ELECTRON CORRELATED MATERIALS

By

Shannon K. Kraemer

## A DISSERTATION

Submitted to
Michigan State University
in partial fulfillment of the requirements
for the degree of

Chemistry – Doctor of Philosophy

2016

#### **ABSTRACT**

# EFFECTS OF LOW DIMENSIONALITY ON PROPERTIES OF THERMOELECTRICS AND STRONGLY ELECTRON CORRELATED MATERIALS

Bv

#### Shannon K. Kraemer

A study of the effects of low dimensionality, in both composites and single phase bulk materials, on thermoelectric properties was carried out. It is proposed that with the correct set of guidelines, bulk composite materials can achieve quantum confinement, inherently increasing the Seebeck coefficient, and lead to an overall increase the figure of merit. For this study, the binary system, Pb<sub>1-x</sub>Na<sub>x</sub>Te-Cd<sub>1-x</sub>Na<sub>x</sub>Te, was chosen based on those guidelines. Several synthetic approaches were employed to produce bulk quantities of nanostructures that mimic the key features of quantum well superlattices, potentially resulting in quantum confined system. This study led to an investigation of the effects of several different synthetic methods, which includes comparing aqueous based techniques such as SILAR versus inert atmosphere ampoule technique, on the thermoelectric properties of the materials. Sol-gel technique was utilized as a new facile method in synthesizing both PbTe and CdTe. The resulting materials were characterized using: thermogravimetric analysis-differential scanning calorimetry, powder X-ray diffraction, low and high temperature Seebeck and resistivity measurements, laser flash analysis, and Hall effect measurements.

An additional study was carried out on the effects of low dimensionality in a lanthanum nickelate family  $T^-Ln_{n+1}Ni_nO_{2n+1}$  (n=3 and  $\infty$ ) known to demonstrate strongly correlated electron behavior. These metastable compounds are commonly formed by reducing a parent compound using low temperature techniques. The final metastable compound contains infinite layer  $NiO_2$  with  $Ni^{1+}$  in

a square planar coordination. The T'-nickelates are of interest, due to the electronic and structural similarities to high temperature superconducting cuprates, where  $Cu^{2+}$  in a square planar coordination,  $CuO_2$ , is a common structural element. The  $NiO_2$  similarity, both isostructural and isoelectronic, to  $CuO_2$  may display similar properties. The first parent compound,  $La_4Ni_3O_{10}$ , was synthesized using traditional solid state techniques, sol-gel and ceramic methods, and was then reduced to  $La_4Ni_3O_8$  using hydrogen gas. The same compound was successfully synthesized with 0.20 Cu dopant,  $La_4Ni_{2.8}Cu_{0.2}O_8$ . The samples were characterized through powder X-ray diffraction, and specific heat. The second parent compound,  $LaNiO_3$ , was synthesized by the same techniques, however, it was reduced to  $LaNiO_2$  using a novel solvothermal reduction technique. The same compound was successfully synthesized for the first time as a Cu doped series  $LaNi_1$ .  $_xCu_xO_2$  where x=0.05, 0.10, 0.15, 0.20, 0.25. The samples were characterized by powder x-ray diffraction for a structural analysis as well as for cell parameters determination.

Copyright by SHANNON K. KRAEMER 2016 Dedicated to my loving parents, Stanley and Robin Kraemer, without whom I would not have made it this far.

#### **ACKNOWLEDGEMENTS**

I would like to thank my advisor, Dr. Viktor V. Poltavets, my lab mates: Dr. Shaun R. Bruno, Dr. Colin K. Blakely, and Dr. Josh D. Davis for all the advice and conversation, my undergraduate researcher, Katherine Wampler, who spent countless hours working and asking questions from a different perspective, Professor Donald T. Morelli and group for their collaboration, endless insight, and help with thermoelectric characterization, and Dr. Richard J. Staples for all his help with X-ray diffraction and instrumentation. This research was supported in part by the National Science Foundation, Grant NSF DMR-1206718.

# TABLE OF CONTENTS

LIST OF TA	BLES	ix
LIST OF FIG	GURES	X
Chapter 1	Introduction to Materials with Low Dimensionality	1
1.1	Introduction to Thermoelectrics	
1.2	Motivation for this Work	5
1.3	Selection of Materials for Bulk Quantum-Confinement	10
1.4	Review of Current Literature Data	11
1.5	Introduction to Square Planar Ni <sup>1+</sup> in LaNiO <sub>2</sub>	15
	REFERENCES	
Chapter 2	Introduction to Synthetic Methods	22
2.1	Pechini Method (Solution-Gelation)	22
2.2	Solid-state Method (Ceramic)	23
2.3	Solvothermal and Gas Phase Reduction of Oxides	23
2.4	Ampoule Synthesis	25
2.5	Successive Ion Layer and Adsorption Reaction	
2.6	Ball Milling	
2.7	Spark Plasma Sintering	27
	REFERENCES	29
Chapter 3	Introduction to Instrumentation	
3.1	Powder X-ray Diffraction Theory and Instrumentation	31
3.2	Scanning Electron Microscopy	36
3.2a	Backscattered Electrons	36
3.2b	Energy Dispersive X-ray Spectroscopy	37
3.2c	Sample Preparation	37
3.2d	High Resolution Scanning Electron Microscopy	38
3.3	Transmission Electron Microscopy	38
3.3a	Sample Preparation	38
3.4	Inductively Coupled Plasma Atomic Emission Spectroscopy	39
3.5	Thermogravimetric Analysis and Differential Scanning Calorimetry	39
3.6	Diffuse Reflectance Infrared Fourier Transform Spectroscopy	40
3.7	Archimedes Density Measurement	41
3.8	Seebeck Coefficient and Resistivity	42
3.8a	Low Temperature Measurements	42
3.8b	High Temperature Measurements	43
3.9	Laser Flash Analysis	44
3.10	Hall Effect Measurements	
	REFERENCES	47
Chapter 4	Synthesis of Bulk Thermoelectric Materials with Low Dimensionality	49

4.1	Synthesis: Successive Ion Layer and Adsorption Reaction	49
4.2	Results and Discussion	50
4.3	Synthesis: Co-precipitation	53
4.4	Results and Discussion	53
4.5	Effect of Ball Milling on Particle Size	55
4.6	Results and Discussion	55
4.7	Synthesis: Sol-gel	57
4.8	Results and Discussion	
4.9	Synthesis: Ampoule Method	68
4.10	Results and Discussion	69
4.11	Conclusions for the Quantum-Confined Thermoelectric Project	73
4.12	Future Work for the Quantum-Confined Thermoelectric Project	76
	REFERENCES	77
Chapter 5	Lanthanum Nickelate T`-Ln <sub>n+1</sub> Ni <sub>n</sub> O <sub>2n+1</sub> Family	79
5.1	Synthesis of La <sub>4</sub> Ni <sub>3</sub> O <sub>10</sub> and La <sub>4</sub> Ni <sub>2.8</sub> Cu <sub>0.2</sub> O <sub>10</sub>	
5.2	Reduction to La <sub>4</sub> Ni <sub>3</sub> O <sub>8</sub> and La <sub>4</sub> Ni <sub>2.8</sub> Cu <sub>0.2</sub> O <sub>8</sub>	
5.3	Synthesis of LaNi <sub>1-x</sub> Cu <sub>x</sub> O <sub>3</sub>	
5.4	Reduction of LaNi <sub>1-x</sub> Cu <sub>x</sub> O <sub>3</sub>	86
5.5	Conclusion for the T`-Lanthanum Nickelate Project	90
5.6	Future Work on the T`-Lanthanum Nickelate Project	
	REFERENCES	
Chapter 6	Conclusions	94

# LIST OF TABLES

	Parameters for selection of materials for the study of core-shell nanoparticle quantum-well superlattices
Table 3.1	Describes the fourteen Bravais lattices
Table 4.1	Summary of parameters used for both sets of SILAR reactions and the powder X-ray diffraction results
Table 5.1	Summary of cell parameters and volumes for hexagonal LaNi <sub>1-x</sub> Cu <sub>x</sub> O <sub>3</sub> series
Table 5.2	Summary of cell parameters and volumes for tetragonal LaNi <sub>1-x</sub> Cu <sub>x</sub> O <sub>2</sub> series

# LIST OF FIGURES

Figure 1.1 Schematic diagram of both the Peltier effect and the Seebeck effect
<b>Figure 1.2</b> Pictorial image of a superlattice.
<b>Figure 1.3</b> Schematic diagram of a band diagram resulting from a quantum-well superlattice 6
<b>Figure 1.4</b> Schematic diagram of the changes in a band diagram as a material goes from bulk to atomic level
<b>Figure 1.5</b> Changes in density of states plots based on the dimension of quantum confinement the material has.
<b>Figure 1.6</b> Thermoelectric measurements and calculated ZT shown for PbTe with SrTe nanoinclusions and Na doping. Reprinted with permission from (19)
<b>Figure 1.7</b> Thermoelectric measurements and calculated ZT for PbS embedded with CdS nanocrystals. Reprinted with permission from (20)
<b>Figure 1.8</b> Carrier concentration, Hall mobility and calculated ZT for PbTe-CdTe doped with PbI <sub>2</sub> . Reprinted with permission from (21).
<b>Figure 1.9</b> Crystal structures of T`-La <sub>n+1</sub> Ni <sub>n</sub> O <sub>2n+1</sub> series. 16
<b>Figure 1.10</b> Square planar orbital diagram for d9 Ni <sup>1+</sup> from LaNiO <sub>2</sub>
<b>Figure 1.11</b> Crystal structure of perovskite LaNiO <sub>3</sub> to the reduced infinite layer LaNiO <sub>2</sub> phase.
Figure 2.1 Schematic diagram of sol-gel synthesis
Figure 2.2 Schematic diagram of spark plasma sintering. 28
Figure 3.1 Energy levels. 32
Figure 3.2 A schematic diagram of Bragg's law.
<b>Figure 3.3</b> A schematic diagram of specular versus diffuse reflectance
<b>Figure 3.4</b> A schematic diagram of a low temperature holder with sample and connections 43
<b>Figure 3.5</b> A schematic diagram of a high temperature holder with sample and connections 43

Figure 3.6	A schematic diagram of Hall effect measurement	45
Figure 4.1	PXRD pattern for sample 3 showing both CdS and PbS phases.	51
Figure 4.2	a. SEM image of sample 3 and b. BSE image of sample 3.	52
	EDS spectrum for sample 3 corresponding to <b>Figure 4.2</b> and showing the sample we composed of CdS.	
Figure 4.4 l	PXRD pattern for co-precipitation method showing both PbTe and CdTe phases	53
Figure 4.5	ΓΕΜ image of co-precipitation, showing both PbTe and CdTe nanoparticles	54
O	PXRD pattern and PM2K calculated size distribution results for the ball milling of burchased PbTe over various milling times.	56
Figure 4.7	ΓΕΜ image, and measurement of particles after four hours of ball milling	57
Figure 4.8	TGA-DSC curve of a lead telluride sol-gel.	58
Figure 4.9	TGA-DSC curve of a lead telluride sol-gel.	59
Figure 4.10	PXRD pattern of PbTe, synthesized by the sol-gel method.	60
Figure 4.11	PXRD pattern of CdTe synthesized by the sol-gel method	60
Figure 4.12	Normalized Kubelka Munk function for raw data for three 1:1 mole ratio of sodiur doped lead telluride to sodium doped cadmium telluride samples synthesized via sol-gel	
Figure 4.13	Normalized Kubelka Munk adsorption coefficient direct gap fit for three 1:1 mole ratio of 2 % sodium doped lead telluride to 2 % sodium doped cadmium telluride samples synthesized via sol-gel.	62
Figure 4.14	HR-SEM images of sample SKBM13_KWSG5_KWSG6 SPS at varying temperatures to determine nano-scale integrity.	63
Figure 4.15	Plot of resistivity versus temperature for 550 °C SPS sample, synthesized via solgel, run three times for comparison.	64
Figure 4.16	Plot of thermopower versus temperature for 550 °C SPS sample, synthesized via sol-gel, run three times for comparison.	65
Figure 4.17	Plot of resistivity versus temperature for SKBM16_SKSG36 synthesized via sol-greater the state of the synthesized via sol-greater the synthesized via synthesized via sol-greater the synthesized via sol-greater the synthesized via synthesi	el 66

<b>Figure 4.18</b> Plot of thermopower versus temperature for SKBM16_SKSG36 synthesized via so	
gel method	56
<b>Figure 4.19</b> Plot of total thermal conductivity versus temperature for SKBM16_SKSG36 synthesized via sol-gel method.	67
<b>Figure 4.20</b> Plot of ZT versus temperature for SKBM16_SKSG36 synthesized via sol-gel method	57
Figure 4.21 PXRD pattern for an ampoule sample showing pure PbTe phase	59
<b>Figure 4.22</b> Plot of resistivity versus temperature for SKBM18_SKAmp23 and SKBM11_SKAmp15 synthesized via ampoule method	70
<b>Figure 4.23</b> Plot of thermopower versus temperature for SKBM18_SKAmp23 and SKBM11_SKAmp15 synthesized via ampoule method	70
<b>Figure 4.24</b> Plot of total thermal conductivity versus temperature for SKBM18_SKAmp23 and SKBM11_SKAmp15 synthesized via ampoule method	
<b>Figure 4.25</b> Plot of ZT versus temperature for SKBM18_SKAmp23 and SKBM11_SKAmp15 synthesized via ampoule method.	
<b>Figure 4.26</b> Graph depicting carrier concentration versus temperature for both SKBM19_SKAmp24 and SKBM11_SKAmp15 synthesized via ampoule method.	72
<b>Figure 4.27</b> Graph depicting carrier mobility versus temperature for both SKBM19_SKAmp24 and SKBM11_SKAmp15 synthesized via ampoule method.	
<b>Figure 5.1</b> PXRD pattern of La <sub>4</sub> Ni <sub>3</sub> O <sub>10</sub> synthesized via sol-gel method.	80
Figure 5.2 PXRD pattern of La <sub>4</sub> Ni <sub>2.8</sub> Cu <sub>0.2</sub> O <sub>10</sub> synthesized via sol-gel method.	80
<b>Figure 5.3</b> PXRD pattern of La <sub>4</sub> Ni <sub>3</sub> O <sub>8</sub> synthesized via sol-gel method and reduced using hydrogen gas.	81
<b>Figure 5.4</b> PXRD pattern of La <sub>4</sub> Ni <sub>2.8</sub> Cu <sub>0.2</sub> O <sub>8</sub> synthesized via sol-gel method and reduced using hydrogen gas.	
$\textbf{Figure 5.5} \ Specific \ heat \ measurements \ for \ La_4Ni_3O_8 \ and \ La_4Ni_{2.8}Cu_{0.2}O_8, \ shown \ respectively. Specific \ heat \ measurements \ for \ La_4Ni_3O_8 \ and \ La_4Ni_{2.8}Cu_{0.2}O_8, \ shown \ respectively. Specific \ heat \ measurements \ for \ La_4Ni_3O_8 \ and \ La_4Ni_2O_8 \$	82
<b>Figure 5.6</b> PXRD pattern of LaNiO <sub>3</sub> synthesized via sol-gel method	84

Figure 5.7 PXRD pattern of LaNi <sub>1-x</sub> Cu <sub>x</sub> O <sub>3</sub> where $x = 0.05$ , 0.10, 0.15, 0.20, and 0.25 synthesized via sol-gel method.
<b>Figure 5.8</b> Plot of volume (Å <sup>3</sup> ) versus x, dopant in LaNi <sub>1-x</sub> Cu <sub>x</sub> O <sub>3</sub> series
<b>Figure 5.9</b> PXRD pattern of LaNi <sub>0.95</sub> Cu <sub>0.05</sub> O <sub>3</sub> reduced using the solvothermal method
<b>Figure 5.10</b> PXRD pattern of LaNi <sub>0.90</sub> Cu <sub>0.10</sub> O <sub>3</sub> reduced using the solvothermal method
<b>Figure 5.11</b> PXRD pattern of LaNi <sub>0.85</sub> Cu <sub>0.15</sub> O <sub>3</sub> reduced using the solvothermal method
<b>Figure 5.12</b> PXRD pattern of LaNi <sub>0.80</sub> Cu <sub>0.20</sub> O <sub>3</sub> reduced using the solvothermal method
<b>Figure 5.13</b> PXRD pattern of LaNi <sub>0.75</sub> Cu <sub>0.25</sub> O <sub>3</sub> reduced using the solvothermal method
<b>Figure 5.14</b> Plot of volume (Å <sup>3</sup> ) versus x, dopant in LaNi <sub>1-x</sub> Cu <sub>x</sub> O <sub>2</sub> series

#### Chapter 1

Introduction to Materials with Low Dimensionality

#### 1.1 Introduction to Thermoelectrics

For a long period of time there has been persistent research in energy materials to ensure that future generations are not left in the dark. When a device is generating work and/or electricity a byproduct is formed known as waste heat. The majority of these devices only work at 30-40% efficiency meaning that up to 60 % of the energy being generated is lost as waste heat. A common form of waste heat that many people may be familiar with is the exhaust from a vehicle. The exhaust is a by-product of using fuel energy to power the vehicle. The United States of America's industrial sector consumes one third of all energy in the United States of America. This industrial sector uses quadrillions of British Thermal Units (Btu) of energy per year; with the potential to save approximately 25% of the revenue spent on energy yearly.<sup>1</sup>

There are a few ways to utilize waste heat, one is diverting the energy to warm buildings and/or sidewalks, however, it becomes harder to utilize waste heat by these means the further the distance from the source of the heat. Due to the difficulty of storing heat other methods of utilizing waste heat must be sought to ensure that the fuels being use to generate energy are not going to waste. One way to utilize waste heat would be to turn it into electricity, this can be done through thermoelectrics.

The thermoelectric effect is a phenomenon in which electricity is generated due to a temperature gradient and vice versa, an electric current can be applied to produce a temperature gradient. This phenomenon is possible through both the Peltier and Seebeck effects as shown below in **Figure**1.1. In the Peltier Effect diagram a current is passed through the circuit, creating a temperature gradient across the material. A heat sink is attached to the warm end so that it remains an ambient

temperature while the cool side remains cold. In the Seebeck effect diagram carriers (electrons and holes) are thermally excited on the hotter end of the device and diffuse to the colder end of the device, creating a potential difference. In a circuit this creates a voltage that can be utilized as electrical output. The Seebeck effect is the desired use of these materials for waste heat application.

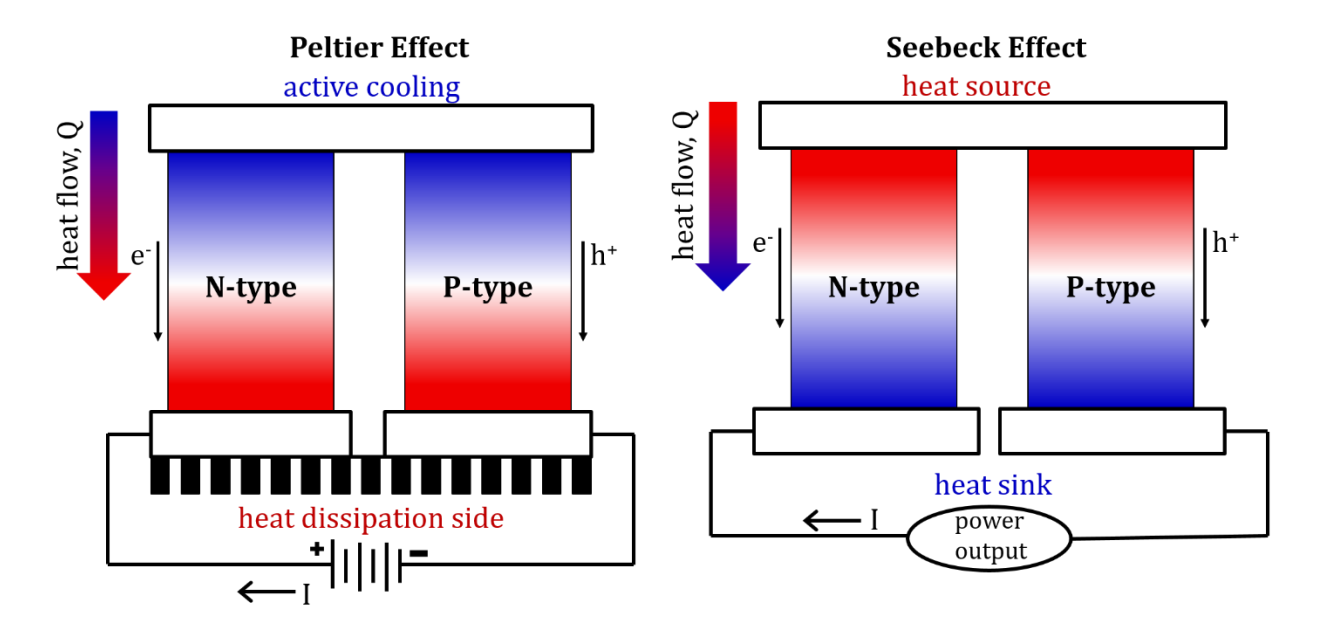


**Figure 1.1** Schematic diagram of both the Peltier effect and the Seebeck effect.

The Seebeck effect phenomenon was first discovered by Johann Seebeck, in 1821, who had joined two differing metal wires together with a compass needle and heated one of the junctions creating a temperature gradient between the two materials. The temperature gradient created an electric current in the loop, deflecting the compass needle. When Seebeck noticed the needle being deflected he thought it was due to a magnetic field rather than an electric current and mistakenly named it the thermomagnetic effect. It was not until a couple years later Hans Christian Ørsted who studied magnetic fields saw this error and rectified it coining the term thermoelectricity. In 1834, Jean Charles Athanase Peltier discovered that the vice versa of the Seebeck effect exists coining it the Peltier effect. He determined that by passing a current through two differing metals

that one junction was cooled while the other was heated. He also determined that this was reversible by changing the direction of the current.<sup>2,3</sup>

Thermoelectric devices have several advantages such as being comprised of solid state parts which allows for little to no maintenance of the devices. The devices are vibration free, and have no acoustical or electrical noise which is beneficial for use in non-industrial settings such as homes. The devices have precise temperature control to within a fraction of a degree, which can be important in certain refrigeration aspects. The devices are chlorofluorocarbon free, which is beneficial for the environment. Thermoelectric devices have shown to have long-term stability, 300,000 hours of steady state operation; as seen in the NASA satellites, voyager 1 and voyager 2.4 These devices work in any physical or gravitational orientation which has been essential for space applications and could play an important role as to how they will be implemented in the industrial sector. Additionally, the devices work on a range of electrical output  $\mu W - kW$  which will be important for the scale of use.

The ability of a thermoelectric material to generate thermoelectric power is determined by the unitless figure of merit (ZT):

$$ZT = \frac{\alpha^2 \sigma}{\kappa_{Total}} T$$
 Equation 1.1

Where  $\alpha$  is the Seebeck coefficient ( $\mu V/K$ ) also referred to as the thermopower (note that sometimes this variable is written as S),  $\sigma$  is the electrical conductivity ( $m\Omega$ -cm)<sup>-1</sup>, and  $\kappa_{Total}$  is the total thermal conductivity (W/m-K). The figure of merit only determines an individual material's ability to generate thermoelectric power and is not to be confused with device efficiency ( $\eta_{max}$ ) which can be calculated using the following:

$$\eta_{max} = \frac{\Delta T}{T_h} \frac{\sqrt{1 + ZT_{avg}} - 1}{\sqrt{1 + ZT_{avg}} + \frac{T_c}{T_h}}$$
 Equation 1.2

where  $T_h$  and  $T_c$  are the hot- and cold-side temperatures,  $\Delta T$  is  $T_h - T_c$ ,  $T_{avg}$  is  $\frac{(T_h - T_c)}{2}$ .

To increase the efficiency of a device the figure of merit must be increased, i.e. the higher the ZT the more efficient the device will work, the more applicable the devices will be in the current market. For decades it was believed that thermoelectric materials could not have a ZT > 1.0, giving these materials an efficiency of ~6 %, making these devices inefficient to be utilized.<sup>5</sup> It was not until the early to mid-1990s that significant advancement was made in the thermoelectric community essentially breaking the glass ceiling of ZT = 1. The ZT has been continually increased with figure of merits increasing to 2 and greater. With a ZT near 2, the efficiency of these devices is predicted to be near 20 %, making them viable for practical applications.<sup>5</sup> While it seems simple to increase the figure of merit it is important to understand how all the terms of the equation are mathematically related, making it difficult to increase the figure of merit significantly. The numerator of **Equation 1.1** is often referred to as the power factor and contains the electrical information about the material. The Seebeck coefficient can be given by:

$$\alpha = \frac{8\pi^2 k_B^2}{3eh^2} m^* T \left(\frac{\pi}{3n}\right)^{2/3}$$
 Equation 1.3

where  $k_B$  is the Boltzmann constant  $(1.38 \times 10^{-23} \text{ m}^2 \text{kgs}^{-2} \text{K}^{-1})$ , e is carrier charge  $(1.6 \times 10^{-19} \text{ C})$ , h is Planck's constant  $(6.63 \times 10^{-34} \text{m}^2 \text{kgs}^{-1})$ , m\* is the effective mass (kg), and n is carrier concentration (cm<sup>-3</sup>).

The denominator consists of the materials thermal information and can be expanded as follows:

$$\kappa_{\text{Total}} = \kappa_{\text{l}} + \kappa_{\text{e}}$$
 Equation 1.4

where  $\kappa_l$  is the thermal lattice contribution and  $\kappa_e$  is the thermal electronic contribution from the movement of carriers. Each of which can be described in more detail as follows:

$$\kappa_{\rm e} = \sigma LT$$
 Equation 1.5

Where L is the Lorentz factor.

$$\kappa_l = \frac{1}{3} (C_v v_s \lambda_{ph})$$
 Equation 1.6

Where  $C_v$  is the lattice heat capacity (J/K),  $v_s$  is the sound velocity (m/s) and  $\lambda_{ph}$  is the phonon mean free path (m).

$$\sigma = ne\mu$$
 Equation 1.7

Where  $\mu$  is the carrier mobility (cm<sup>2</sup>/Vs).

#### 1.2 Motivation for this Work

In the early 1990s it was the Department of Defense (DoD) that encouraged the scientific community to work on thermoelectrics believing that these materials had more potential than was being utilized. This led a large scientific community to work on these materials to come up with the next big idea. Two big concepts spurred from this event; one was new families of bulk materials and the other was applying low dimensionality to these materials.<sup>6</sup> The focus of this research stemmed from the work on low dimensionality, which will be discussed in further detail. In 1992 Mensah and Kangah proposed that a semiconductor superlattice would show an improvement in the efficiency of thermoelectrics.<sup>7</sup> Not too long after in 1993 Hicks and Dresselhaus proposed that quantum-well superlattice structures could significantly increase the Seebeck coefficient while leaving both the electrical and thermal conductivity largely unaffected.<sup>8</sup>

Quantum confinement is referring the restriction of movement for either an electron or a hole by using a potential barrier. This occurs when a direction in space is limited to less than the de Broglie wavelength of an electron or hole, also referred to as the exciton Bohr radius. A quantum-well

refers to a material with quantum-confinement in one directional orientation, while a quantum-wire is confined in two directions, and a quantum dot is confined in all three orientations in space.

A superlattice refers to alternating thin layers of material as depicted in **Figure 1.2**.

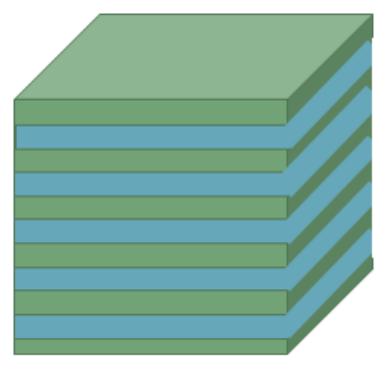


**Figure 1.2** Pictorial image of a superlattice.

By alternating materials, a potential barrier is created between the two materials due to the band gaps of the materials as shown in **Figure 1.3**.

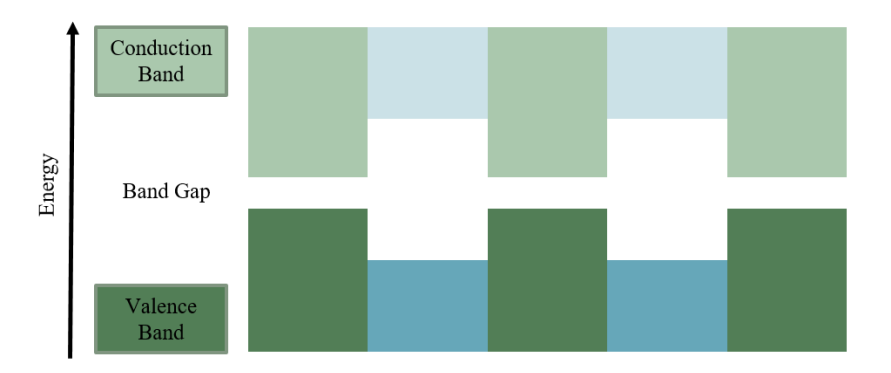


**Figure 1.3** Schematic diagram of a band diagram resulting from a quantum-well superlattice.

When the layers of the material are thin enough to be comparable to the de Broglie wavelength the materials' bands start to form discrete energy levels similar to those seen in atomic materials.

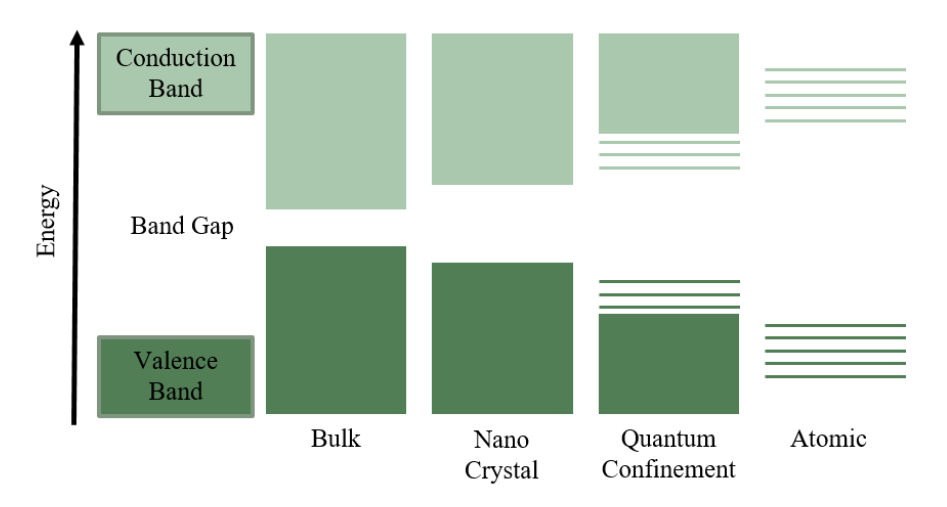


**Figure 1.4** Schematic diagram of the changes in a band diagram as a material goes from bulk to atomic level.

The density of states (DOS) is the number of energy levels available to be occupied at a certain energy. When materials begin to have discrete energy levels the DOS changes drastically as shown in **Figure 1.5**. This change in the DOS allows for the Seebeck coefficient, electrical conductivity, as well as thermal conductivity to be treated quasi-independently.<sup>6</sup> Since this occurs a new relationship must be determined to relate the DOS to the thermoelectric figure of merit.

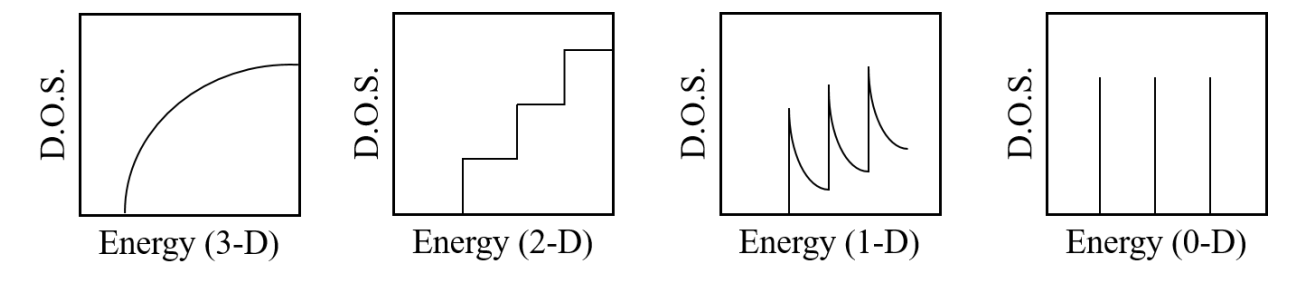


**Figure 1.5** Changes in density of states plots based on the dimension of quantum confinement the material has.

The relationship between the DOS and Seebeck coefficient can be shown through the Mott equation<sup>9</sup>, **Equation 1.8**.

$$\alpha = \frac{\pi^2 k^2 T}{3} \frac{d \ln \sigma(E)}{dE} \bigg|_{E=E_f}$$
 Equation 1.8

Where  $\sigma(E)$  is the electrical conductivity determined as a function of band filling, or Fermi energy,  $E_f$ . If electronic scattering is assumed to be independent of energy, then  $\sigma(E)$  is proportional to the DOS at  $E_f$ .<sup>10</sup> To summarize, the more drastic the change in DOS the larger the Seebeck coefficient value without essentially changing either the electrical or thermal conductivity. It is important to state that this relationship only holds true for metals and highly degenerate semiconductors.

With this change in relationship between DOS and Seebeck coefficient the maximum figure of merit that can be attained is given by the following<sup>10</sup>:

$$Z_{max} \propto \gamma \frac{T^{3/2} \tau_z \sqrt{\frac{m_x m_y}{m_z}}}{\kappa_l} e^{(r+1/2)}$$
 Equation 1.9

where  $\gamma$  is the degeneracy of band extrema,  $m_i$  is the effective mass of the carriers in the *i*-th direction,  $\tau_z$  is the relaxation time of the carriers moving along the transport (z) direction, and r is the scattering parameter.

Hicks and Dresselhaus were amongst some of the first to show that this relationship between the well thickness and an increase in the figure of merit.<sup>8</sup> They modeled this using bismuth telluride ( $Bi_2Te_3$ ), the best thermoelectric during that time with a ZT of 0.52. It was concluded that quantum-well superlattices have the potential to increase the figure of merit by a factor of 13, by decreasing the layer thickness of the thin film.

Only a few short years later in 1996, Hicks et al. published an experimental follow up to their theoretical work. Using Molecular Beam Epitaxy (MBE) the group was able to deposit thin film quantum-well superlattices comprised of lead telluride/europium doped lead telluride (PbTe/Pb $_{0.927}$ Eu $_{0.073}$ Te) onto a barium fluoride (BaF $_2$ ) substrate. The group was able to present calculations for  $\alpha^2$ n versus well thickness for the materials showing the same general trend that

with a decrease thickness there is an increase in  $\alpha^2 n$ . The experimental data was shown be in general agreement with the calculations, however, slightly lower than the calculated values. Using known bulk thermal conductivity, the materials still showed a figure of merit five times greater than bulk material.

Sofo and Mahan were also able to show a calculated relationship between an increase in the figure of merit due to an enhancement of density of states through a superlattice. It was determined by Sofo and Mahan that there was a limit to the well thinness and too thin of a well would lead to band broadening which would not result in an increase in ZT.<sup>12</sup> Khitun et al. modeled a relationship between silicon (Si) thin film layers and germanium Ge quantum dots in a superlattice.<sup>13</sup> Koga et al. experimentally showed an improvement in the figure of merit using Si/Ge layers in a superlattice.<sup>14</sup> Lin et al. demonstrated a similar relationship for bismuth nanowires.<sup>15</sup> Following Hicks et al. experimentally enhancing Seebeck coefficient in PbTe quantum wells in Pb1-xEuxTe/PbTe quantum-well superlattices, Harman et al. experimentally showed an increase in the Seebeck coefficient for several lead telluride materials.<sup>16,17,18</sup>

Several groups during this time demonstrated proof of concept that quantum-confined superlattice materials enhance the Seebeck coefficient, increasing thermoelectric figure of merit. Two problems arose from this proof of concept, first, thin films grown by molecular beam epitaxy are extremely costly, secondly, in addition to the cost of thin films, thermoelectric device which requires several legs of the materials to contribute enough power, not easily accomplished using thin films. The solution would be to apply this proof of concept to bulk materials, which is generally less costly than thin films and secondly provides ample material for building the thermoelectric devices.

## 1.3 Selection of Materials for Bulk Quantum-Confinement

To take a proof of concept idea for thin films and apply it to bulk materials, it requires the identifying of parameters for selection of materials that will allow the new system to be analogues. First, it was important to decide how create a quantum-confinement in bulk materials using particles rather than thin films. To do this it was determined that two possible routes could be pursued; one core-shell nanoparticles and the other two composite nanoparticle systems. Nanoparticles would be utilized, where the core material would be nano sized however, it would not need to be below the magnitude of the materials exciton Bohr radius, and the shell would be formed at or below the size of the magnitude of the materials exciton Bohr radius to quantum confine the material creating a quantum-well superlattice. To accomplish core-shell nanoparticle quantum-well superlattices it is important to select materials that have similar crystal structures as well as cell parameters. Having similar crystal structures as well as cell parameters will allow for the ease of endotaxial growth when forming a shell onto the core particle. The second route comprised of a two composite system would encompass a homogenous mixture of two types of nanoparticles.

Secondly, the materials should vary in band gap values. The difference in the bang gap values allows for a potential barrier to be created between the two materials as discussed earlier. In addition to the difference in band gaps it is important that the conduction bands align for favorable electron mobility in n-type materials or the valence band aligns for favorable hole mobility in p-type materials.

Lastly, it is important that the two materials selected have a low solid solution limit. To control the doping of the material, it is important that the neither of the materials will create a solid solution. When selecting whether a material is n-type or p-type doped it is important that the

material remain one type of dopant. When working with a two band material the Seebeck coefficient is given by the following:

$$\alpha = \frac{\alpha_1 \sigma_1 + \alpha_2 \sigma_2}{\sigma_1 + \sigma_2}$$
 Equation 1.10

It is significant to recognize that if the materials have Seebeck coefficients of opposite signs then the figure of merit will be reduced. If the materials are of the same sign that both the Seebeck coefficient and the figure of merit will be limited.

Based on the above parameters the following materials were selected.

**Table 1.1** Parameters for selection of materials for the study of core-shell nanoparticle quantum-well superlattices.

Compound	Crystal Structure	Unit Cell Parameter (Å)	Band gap at 300 K (eV)	Exciton Bohr radius (nm)
lead telluride (PbTe)	Rock salt	6.46	0.29	46
cadmium telluride (CdTe)	Zinc blende	6.41	1.50	7.5
lead sulfide (PbS)	Rock salt	5.94	0.37	20
cadmium sulfide (CdS)	Zinc blende Wurtzite	5.81	2.53	5.8

Based on these parameters it was determined that cadmium based compounds would act as the core materials while lead based compounds would be used as the shells due to lead based compounds having generous exciton Bohr radii. Although, the materials differ in crystal structures, both the rock salt structure and the zinc blende structure have face centered cubic (FCC) anion lattices, to allow for endotaxial growth.

#### 1.4 Review of Current Literature Data

The literature on thermoelectric materials is immense and continues to expand frequently. Select literature data will be shown and discussed in this section for a comparison to the materials selected for this project. Biswas et al. explored the performance of thermoelectric materials by engineering

multi-tiered architectures, using bulk PbTe with strontium telluride (SrTe) nanocrystal inclusions, and sodium doping.<sup>19</sup> The multi-tiered structures showed an enhancement in ZT, 2.2, by efficiently scattering phonons on multiple length scales. The thermoelectric measurements including the calculated conductivity via resistivity measurement, thermopower denoted by S, total thermal conductivity, and calculated ZT are shown in **Figure 1.6**.

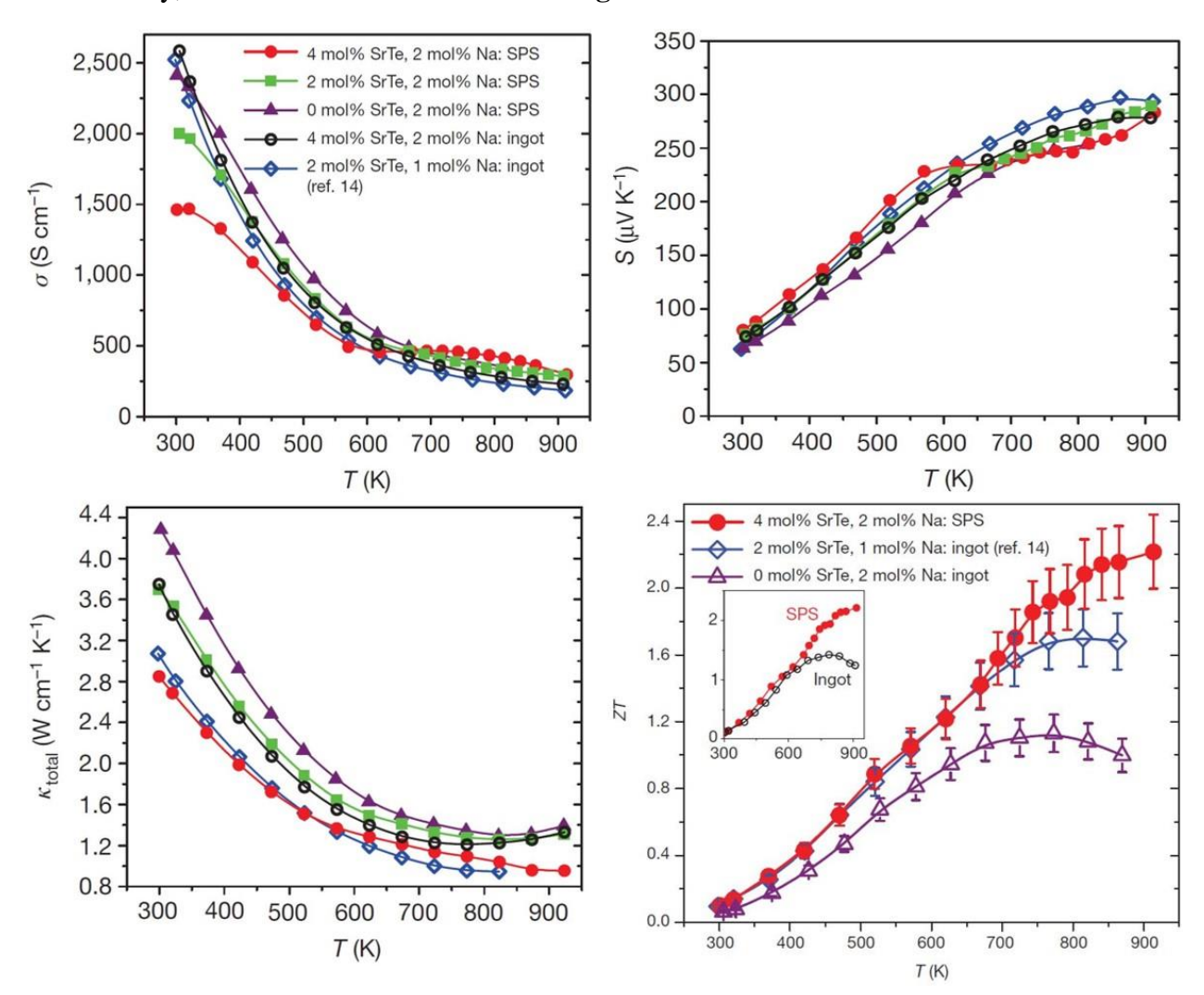


**Figure 1.6** Thermoelectric measurements and calculated ZT shown for PbTe with SrTe nanoinclusions and Na doping. Reprinted with permission from (19).

It was concluded by Biswas et al. that the enhancement in the figure of merit resulted from a lowered thermal conductivity by efficiently scattering phonons as well as generation of carriers at elevated temperatures through sodium dissolution. Overall, Biswas et al. focused on the scattering

of phonons by generating different scales of materials in one sample. This project differs by only utilizing 2 % Na doped PbTe samples without SrTe nanocrystal inclusions.

Zhao et al. investigated the enhancement in thermoelectric performance through endotaxial nanostructuring and valence-band offset engineering, by means of PbS embedded with CdS nanocrystals. <sup>20</sup> This investigation was based on Biswas et al. results of PbTe embedded with SrTe nanocrystals. Sulfide materials were chosen due to sulfur being very earth abundant and more cost friendly for widespread application. The thermoelectric measurements including the calculated conductivity via resistivity measurement, thermopower denoted by S, total thermal conductivity, and calculated ZT are shown in **Figure 1.7**.

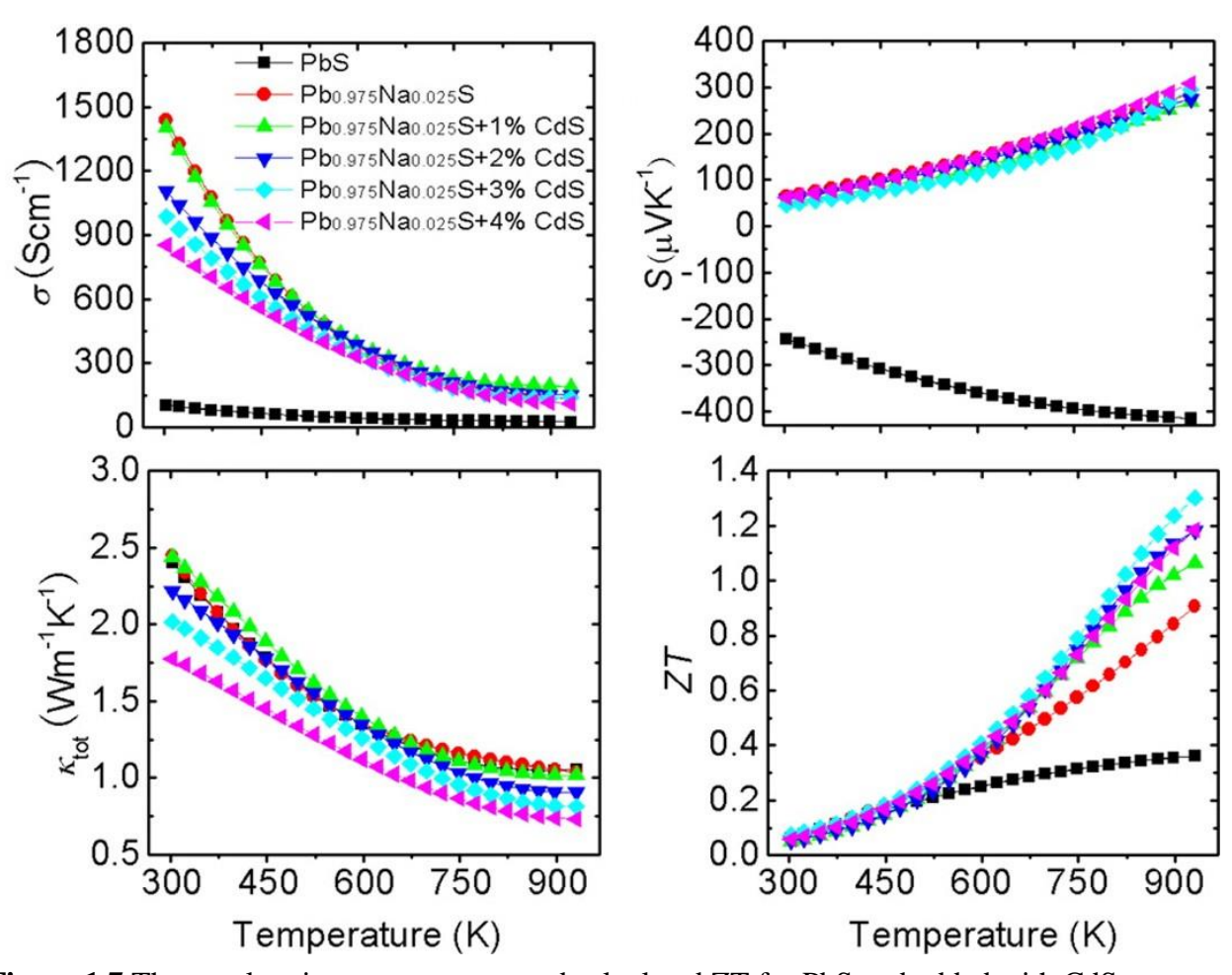


**Figure 1.7** Thermoelectric measurements and calculated ZT for PbS embedded with CdS nanocrystals. Reprinted with permission from (20).

Zhao et al. concluded that in addition to efficient phonon scattering valence band alignment allowed for favorable hole mobility in the material, permitting the ZT of PbS to increase from 1.1 to 1.3. This projects materials differ by attempting to utilize the CdS as a core and PbS as a shell of a core-shell material instead of utilizing PbS as the bulk of the material and CdS as nanocrystal inclusions.

Ahn et al. studied the enhancement of thermoelectric properties through resonant energy levels and nanostructuring via PbTe-CdTe doped with lead iodide (PbI<sub>2</sub>).<sup>21</sup> Previously Heremans et al. reported an enhancement in the thermopower through a distortion of the DOS in the valence band.<sup>22</sup> It was concluded the distortion in the DOS resulted from the dopant introducing resonant energy levels. Ahn et al. results for carrier concentration, Hall mobility, and calculated ZT are shown in **Figure 1.8**.

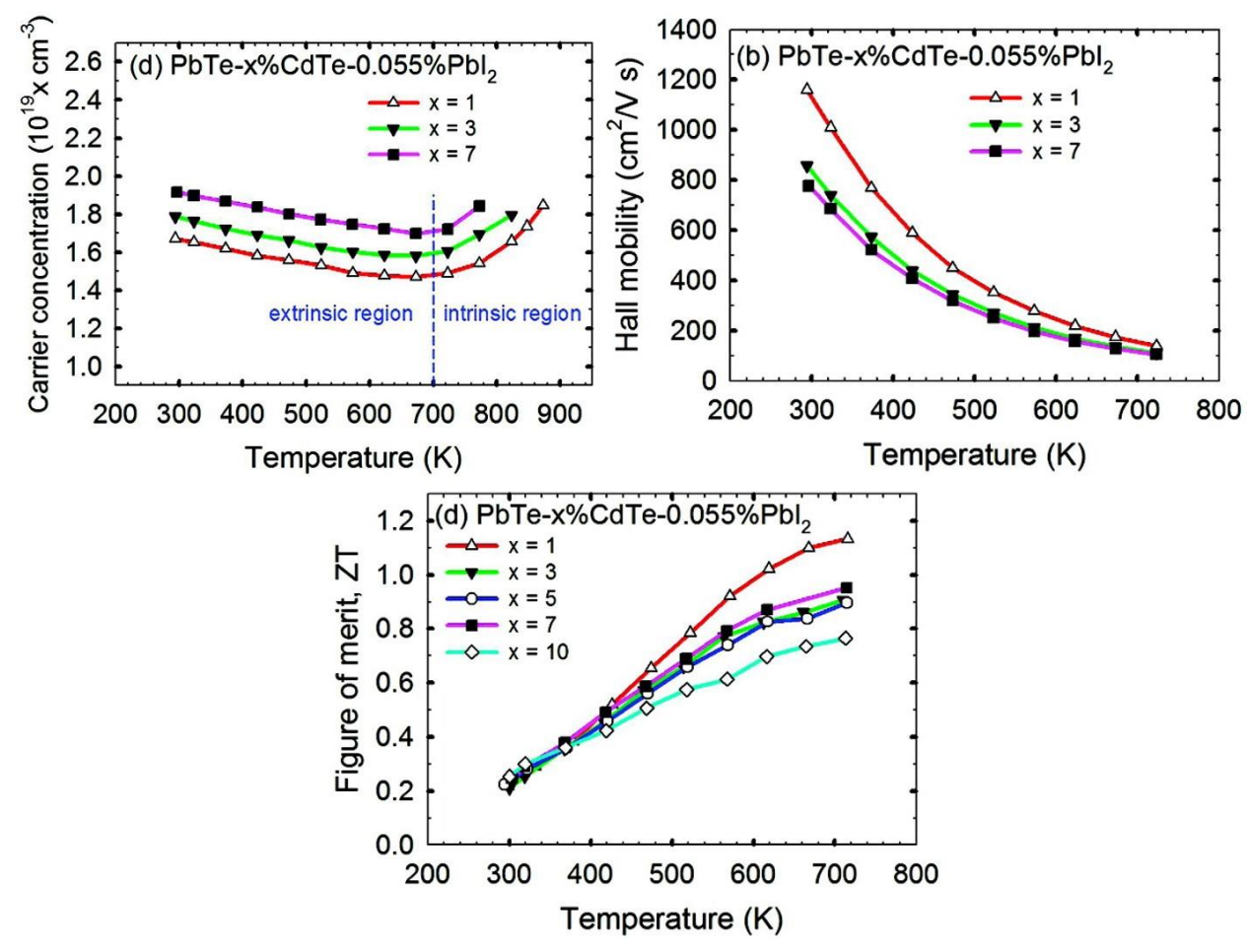


**Figure 1.8** Carrier concentration, Hall mobility and calculated ZT for PbTe-CdTe doped with PbI<sub>2</sub>. Reprinted with permission from (21).

Ahn et al. concluded that either the PbTe-CdTe system did not contain resonant energy levels or that the levels were not attainable through the doping amounts used. It was also noted that the CdTe solubility in PbTe was much lower than reported by the phase diagram, and in actuality was < 1 %. This project differs by not relying on CdTe to dope PbTe conversely to have CdTe be a secondary phase to PbTe in either route of obtaining quantum-confinement in bulk materials.

# 1.5 Introduction to Square Planar Ni<sup>1+</sup> in LaNiO<sub>2</sub>

The family of T`-Ln<sub>n+1</sub>Ni<sub>n</sub>O<sub>2n+1</sub> (Ln = La, Nd; n = 2, 3, and  $\infty$ ) all contain an infinite NiO<sub>2</sub> square planar configuration as shown in **Figure 1.9**. These materials are metastable and are prepared from

low temperature reactions from corresponding Ruddlesden-Popper or perovskite parent compound.

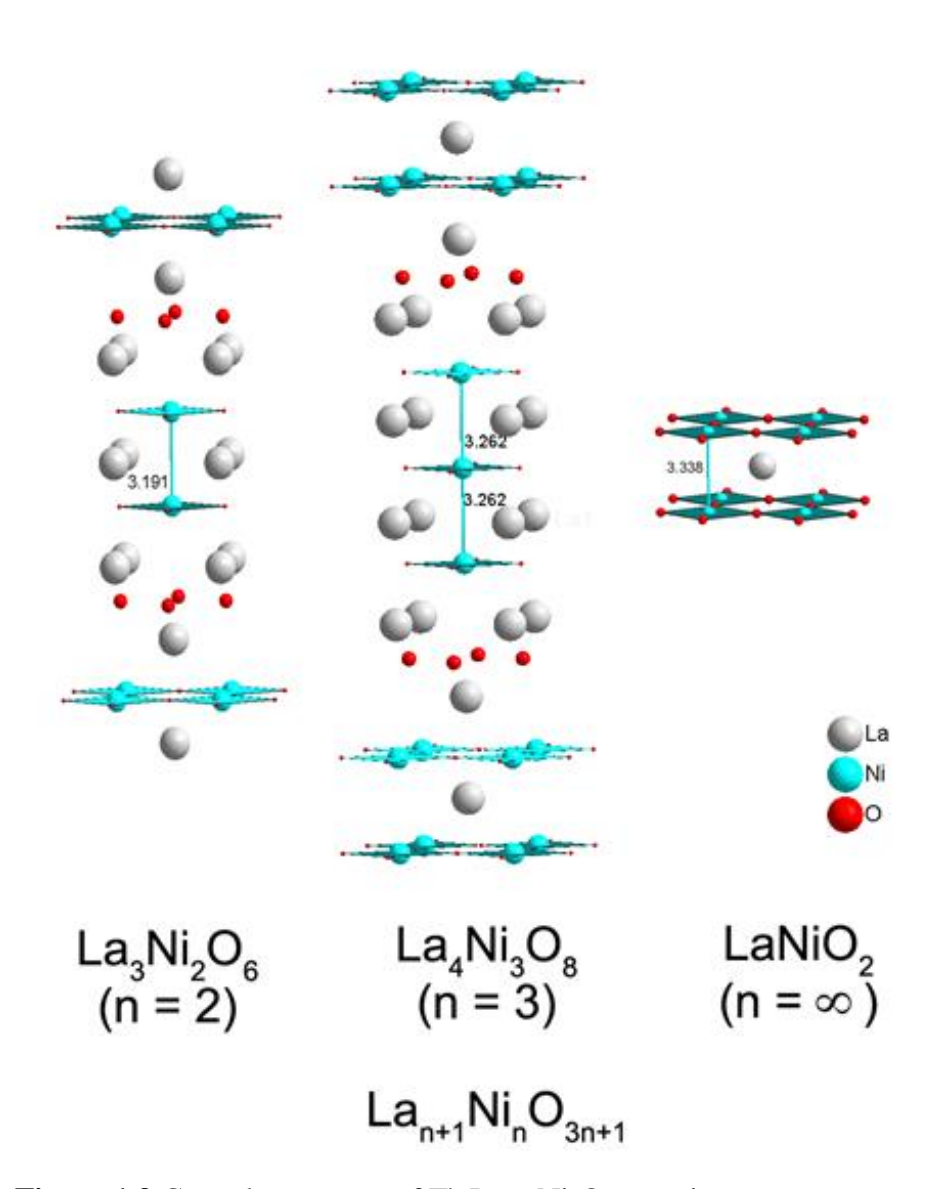


**Figure 1.9** Crystal structures of T`-La<sub>n+1</sub>Ni<sub>n</sub>O<sub>2n+1</sub> series.

The  $Ni^{1+}/Ni^{2+}$  in these compounds are isoelectronic (d9/d8) to the  $Cu^{2+}/Cu^{3+}$  in high temperature superconducting cuprates. Prior superconductors claim to be an analogue to the cuprates, however, the materials do not have the same electronic configuration. The  $T^-Ln_{n+1}Ni_nO_{2n+1}$  series offer the

opportunity to investigate whether mimicking the electronic and structural features of the cuprates would also result in high temperature superconductivity.

The compound, LaNiO<sub>3</sub> was selected due to its reduced phase LaNiO<sub>2</sub> forms a d9 Ni<sup>1+</sup> metal in an infinite square planar configuration with the  $d_{x^2-y^2}$  singly filled and the rest of the d orbitals are doubly filled. The square planar orbital diagram for d9 Ni<sup>1+</sup> is shown in **Figure 1.10**. The Ni in LaNiO<sub>2</sub> is both isoelectronic and isostructural to the d9 Cu<sup>2+</sup> in high temperature superconducting cuprates with infinite layer CuO<sub>2</sub>. <sup>23,24,25</sup>

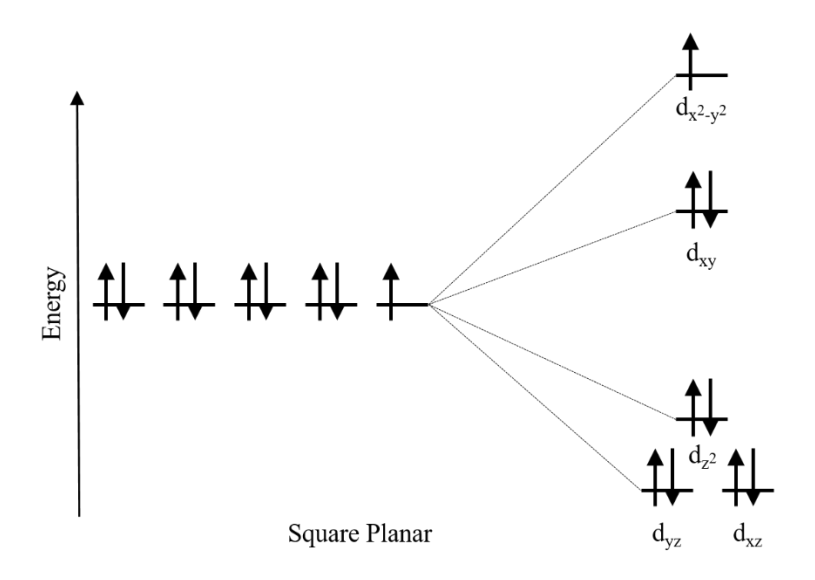


**Figure 1.10** Square planar orbital diagram for d9 Ni<sup>1+</sup> from LaNiO<sub>2</sub>.

The reduced form, LaNiO<sub>2</sub>, was first published by Crespin and Gatineau in 1983.<sup>26</sup> The set up for this reduction was extremely complicated and the K-adsorptions edge shows the possibility of a Ni impurity in the LaNiO<sub>2</sub> sample. This would not be seen by using PXRD due to Ni metal being amorphous at low temperatures. Hayward was the next group to publish pivotal work on this material, which included an ampoule reduction using sodium hydride (NaH).<sup>27</sup> This method still gave mixed impurities in the final sample, however, it was an important step forward in using simple techniques and common reagents. Following this the Koike group did a very similar

reaction to the Hayward group, however, instead of NaH, calcium hydride (CaH<sub>2</sub>) was used as a reducing agent.<sup>28</sup> This method allowed for LaNiO<sub>2</sub> to be the major phase produced, although, Ni metal impurity was still present in the material. Most recently, a "chimie douce" method has been applied to reducing LaNiO<sub>3</sub>, by using a low temperature solvothermal technique.<sup>29</sup> The method employed using different pressure from varying solvents, and varying reducing agents to reduce LaNiO<sub>3</sub> without over reducing to produce Ni metal.

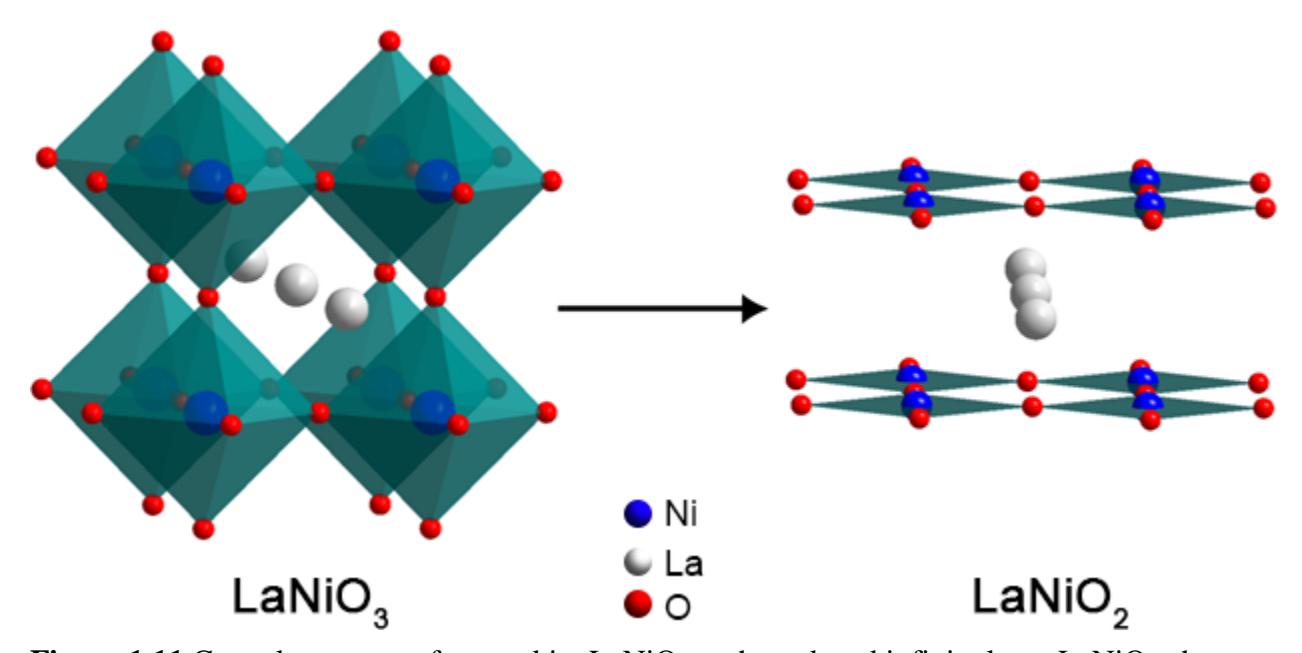


Figure 1.11 Crystal structure of perovskite LaNiO<sub>3</sub> to the reduced infinite layer LaNiO<sub>2</sub> phase.

REFERENCES

#### REFERENCES

- (1) Energetics Incorporated. Technology Roadmap Energy Loss Reduction and Recovery in Industrial Energy Systems; 2004.
- (2) Velmre, E. Thomas Johann Seebeck (1770-1831). *Proc. Est. Acad. Sci.* **2007**, *13* (4), 276–282.
- (3) Peltier. Nouvelles Experiences Sur La Caloricite Des Courants Electrique. *Ann. Chim. Phys.* **1834**, *56*, 371–386.
- (4) Angrum, A.; Medina, E.; Sedlacko, D. Voyager The Interstellar Mission http://voyager.jpl.nasa.gov/.
- (5) Kanatzidis, M. Nanostructures Thermoelectrics . The New Paradigm Mercouri Kanatzidis Department of Energy. **2012**.
- (6) Dresselhaus, B. M. S.; Chen, G.; Tang, M. Y.; Yang, R.; Lee, H.; Wang, D.; Ren, Z.; Fleurial, J.; Gogna, P. New Directions for Low-Dimensional Thermoelectric Materials \*\*. *Adv. Mater.* **2007**, *19* (8), 1043–1053.
- (7) Mensah, S. Y.; Kangah, G. K. The Thermoelectric Effect in a Semiconductor Superlattice in a Non-Quantized Electric Field. *J. Phys. Condens. Matter* **1992**, *4*, 919–922.
- (8) Hicks, L. D.; Dresselhaus, M. S. Effect of Quantum-Well Structures on the Thermoelectric Figure of Merit. *Phys. Rev. B* **1993**, *47* (19), 12727–12731.
- (9) Mott, N. F.; Jones, H. *The Theory of the Properties of Metals and Alloys*; Dover Publications: New York, 1958.
- (10) Sootsman, J. R.; Chung, D. Y.; Kanatzidis, M. G. New and Old Concepts in Thermoelectric Materials. *Angew. Chem. Int. Ed. Engl.* **2009**, *48* (46), 8616–8639.
- (11) Hicks, L.; Harman, T.; Sun, X.; Dresselhaus, M. Experimental Study of the Effect of Quantum-Well Structures on the Thermoelectric Figure of Merit. *Phys. Rev. B. Condens. Matter* **1996**, *53* (16), R10493–R10496.
- (12) Sofo, J. O.; Mahan, G. D. Thermoelectric Figure of Merit of Superlattices. *Appl. Phys. Lett.* **1994**, *65* (21), 2690.
- (13) Khitun, a; Balandin, a; Liu, J. L.; Wang, K. L. In-Plane Lattice Thermal Conductivity of a Quantum-Dot Superlattice. *J. Appl. Phys.* **2000**, 88 (2), 696–699.
- (14) Koga, T.; Cronin, S. B.; Dresselhaus, M. S.; Liu, J. L.; Wang, K. L. Experimental Proof-of-Principle Investigation of Enhanced Z[sub 3D]T in (001) Oriented Si/Ge Superlattices. *Appl. Phys. Lett.* **2000**, 77 (10), 1490–1492.
- (15) Lin, Y.-M.; Cronin, S. B.; Ying, J. Y.; Dresselhaus, M. S.; Heremans, J. P. Transport Properties of Bi Nanowire Arrays. *Appl. Phys. Lett.* **2000**, *76* (26), 3944–3946.
- (16) Harman, T. C.; Taylor, P. J.; Spears, D. L.; Walsh, M. P. Thermoelectric Quantum-Dot

- Superlattices with High ZT. J. Electron. Mater. 2000, 29 (1), L1–L2.
- (17) Harman, T. C.; Taylor, P. J.; Walsh, M. P.; LaForge, B. E. Quantum Dot Superlattice Thermoelectric Materials and Devices. *Science* **2002**, *297* (5590), 2229–2232.
- (18) Harman, T. C.; Walsh, M. P.; LaForge, B. E.; Turner, G. W. Mechanical Properties of Bi X Sb 2– X Te 3 Nanostructured Thermoelectric Material. *J. Electron. Mater.* **2005**, *34* (5), L19–L22.
- (19) Biswas, K.; He, J.; Blum, I. D.; Wu, C.-I.; Hogan, T. P.; Seidman, D. N.; Dravid, V. P.; Kanatzidis, M. G. High-Performance Bulk Thermoelectrics with All-Scale Hierarchical Architectures. *Nature* **2012**, *489* (7416), 414–418.
- (20) Zhao, L.; He, J.; Hao, S.; Wu, C.; Hogan, T. P.; Wolverton, C.; Dravid, V. P.; Kanatzidis, M. G. Raising the Thermoelectric Performance of P Type PbS with Endotaxial Nanostructuring and Valence-Band O Ff Set Engineering Using CdS and ZnS. **2012**.
- (21) Ahn, K.; Han, M.; He, J.; Androulakis, J.; Ballikaya, S.; Uher, C.; Dravid, V. P.; Kanatzidis, M. G. Exploring Resonance Levels and Nanostructuring in the PbTe CdTe System and Enhancement of the Thermoelectric Figure of Merit. *J. Am. Chem. Soc.* **2010**, *132* (11), 5227–5235.
- (22) Heremans, J. P.; Jovovic, V.; Toberer, E. S.; Saramat, A.; Kurosaki, K.; Charoenphakdee, A.; Yamanaka, S.; Snyder, G. J. Enhancement of Thermoelectric Efficiency in PbTe by Distortion of the Electronic Density of States. *Science* **2008**, *321* (5888), 554–557.
- (23) Wen, X. D.; Cahill, T. J.; Gerovac, N. M.; Bucknum, M. J.; Hoffmann, R. Playing the Quantum Chemical Slot Machine: An Exploration of ABX 2 Compounds. *Inorg. Chem.* **2010**, *49* (1), 249–260.
- (24) Al-Mamouri, M.; Edwards, P. P.; Greaves, C.; Slaski, M. Synthesis and Superconducting Properties of the Strontium Copper Oxy-Fluoride Sr2CuO2F2+delta. *Nature* **1994**, *369* (6463), 382–384.
- (25) Skakle, J. M. S. Crystal Chemical Substitutions and Doping of YBa2Cu3Ox and Related Superconductors. *Mater. Sci. Eng. R Reports* **1998**, *23* (1), 1–40.
- (26) Levitz, B. Y. P.; Levitz, B. Y. P. Reduced Forms of LaNi03 Perovskite. *Local Environ.* **1983**, 1195–1203.
- (27) Hayward, M. A.; Green, M. A.; Rosseinsky, M. J.; Sloan, J.; Road, S. P.; Ox, O.; May, R. V. Sodium Hydride as a Powerful Reducing Agent for Topotactic Oxide Deintercalation: Synthesis and Characterization of the Nickel (I) Oxide LaNiO 2. **1999**, 2 (I), 8843–8854.
- (28) Takamatsu, T.; Kato, M.; Noji, T.; Koike, Y. Low-Temperature Synthesis of the Infinite-Layer Compound LaNiO2 Using CaH2 as Reductant. *Phys. C Supercond. its Appl.* **2010**, 470 (SUPPL.1), 2009–2010.
- (29) Blakely, C. K. Ph.D. Dissertation, Michigan State University, 2014.

#### Chapter 2

## Introduction to Synthetic Methods

## 2.1 Pechini Method (Solution-Gelation)

The Pechini method, also referred to as a solution-gelation or sol-gel, was originally designed to synthesize dielectric materials for capacitors. Since it was first patented in 1967 it has been used for a wider range of glass and ceramic materials. The sol-gel method is a wet chemistry method that relies upon mixing stoichiometric ratios of mixed ion precursors to create a gelatin-like polymer. Upon heating the gel-like polymer the matrix is removed and mixed oxides and carbonates are left behind. Through increased heating in an oxygen rich environment a mixed metal oxide is produced.

The sol-gel method includes the addition of stoichiometric ratios of metal salts and/or metal oxides with 2-hydroxypropane-1,2,3-tricarboxylic acid commonly referred to as citric acid (C<sub>6</sub>H<sub>8</sub>O<sub>7</sub>), ethane-1,2-diol commonly referred to as ethylene glycol (C<sub>2</sub>H<sub>6</sub>O<sub>2</sub>), nitric acid (HNO<sub>3</sub>), and water. The addition of nitric acid aids the metals in dissolving into the solution. The citric acid and ethylene glycol form a citrate polymer network, which upon heating above 100 °C to remove excess water forms a gel-like polymer network. Further heating of the gel at temperatures dependent upon the material removes the polymer network and forms metal oxides and/or metal carbonate mixture. The materials can then be treated further to obtain desired materials under appropriate conditions. Specific conditions for samples will be discussed individually upon discussing each sample.<sup>1</sup>

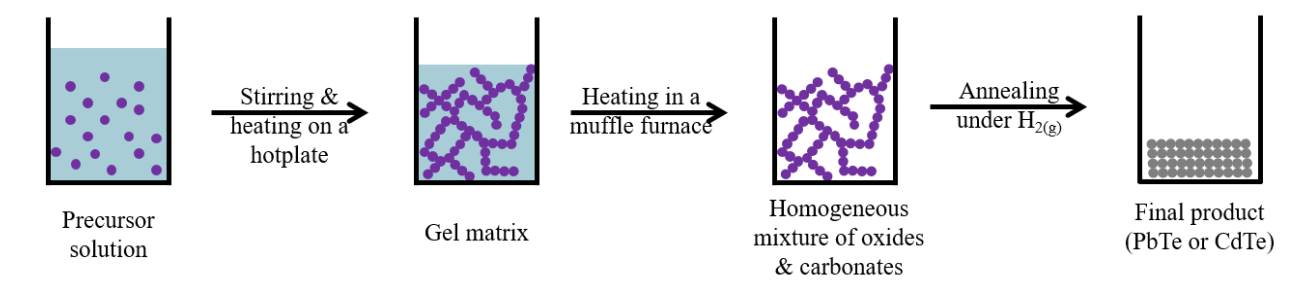


Figure 2.1 Schematic diagram of sol-gel synthesis.

### 2.2 Solid-state Method (Ceramic)

The solid-state reaction, also referred to as the ceramic method, is a synthesis technique widely used in solid state chemistry. The method consists of reacting solid materials either metals, metal oxides, or metal oxoanion precursors. This method is limited by the slow rate of reaction between solids, and therefore these reactions are carried out at high temperature, generally near or above 1000 °C depending on the reaction, to have the reaction occur at an appreciable rate. In addition to the slow rate of reaction, solid-state reactions can be limited in diffusion due to grain boundaries, so materials generally have to be ground with a mortar and pestle to decrease the particle sizes prior to heating. The samples are also generally pressed into a pellet using a die set and press to increase the area of reaction. It is extremely important when doing these reactions that the sample be homogeneous which can again be accomplished by hand grinding the sample. Some samples require repetitive grinding in between heating to increase nucleation sites for the sample to react. Due to the high temperatures and repetitive grinding in this method it is often referred to as the "heat and beat" method. Depending on the type of material being synthesized specific conditions of temperature, time, and atmosphere are varied, the individual parameters will be listed for each specific reaction.<sup>2</sup>

#### 2.3 Solvothermal and Gas Phase Reduction of Oxides

Reduction methods can be utilized to create metastable metal oxides that cannot be directly synthesized. These metastable oxides may contain properties that may not be present in the non-

reduced phases. Several methods for reduction exist however two specific methods will be discussed, a solvothermal technique as well as hydrogen gas technique.

The solvothermal technique utilizes stainless steel autoclaves in which the reactions take place. The reaction takes place in an appropriate solvent and with a metal hydride. The highly reducing metal hydride is mixed in stoichiometric ratios with the sample being reduced. The sample and metal hydride are intimately ground with a mortar and pestle in a glove box prior to being loaded in the autoclave, this is to ensure homogeneous reduction of the sample. After the samples have been heated they are placed back into the glovebox to remove any excess metal hydride and metal hydroxide that has formed. The specific conditions of the reaction including solvent choice as well as metal hydride is dependent upon specific samples and will be discussed extensively in later chapters.

The second method of reduction utilizes 100 % hydrogen gas (H<sub>2</sub>). The use of 100 % H<sub>2</sub> gas can be exceptionally dangerous due to the severe flammability of it, and extreme care is needed to ensure safety. All reactions that took place in hydrogen were done so in a fume hood, and below the autoignition temperature of 500 °C. Another safety precaution was all hydrogen reactions took place in quartz tubes instead of alumina due to the porosity of alumina and potential for a leak into the furnace. The gas was flowed through the tube at a slow rate that was monitored using a bubbler. To ensure the gas was dry it was flowed over phosphorus pentoxide (P<sub>2</sub>O<sub>5</sub>) mixed with glass wool as well as an alumina boat with P<sub>2</sub>O<sub>5</sub> prior to reaching the sample. An alumina boat full of P<sub>2</sub>O<sub>5</sub> was also placed after the sample to react with any of the moisture the sample produced upon reacting with the hydrogen gas. The samples were centered in the furnace for the most controlled heating and were placed in an alumina boat as loose powder to give more surface area to react and reduce. Specific conditions of samples will be explained in more detail during later chapters.

## 2.4 Ampoule Synthesis

Glass and quartz ampoules are another common method for synthesizing samples in material sciences. This method can also be used to reduce samples, however, that will not be discussed within the contents of this thesis. This technique generally works by adding stoichiometric ratios of metals to an ampoule, evacuating the ampoule, flame sealing the ampoule, and then heating the sample to an appropriate temperature. Depending on the temperature the ampoule is being heating to, the ampoule would be either glass for lower temperatures or quartz for higher temperatures. If the sample is known to react with silicon dioxide (SiO<sub>2</sub>) then the ampoule will be carbon coated by combusting acetone in the ampoule. When the samples are heated to appropriate temperatures sometimes the synthesis is controlled by the cooling method. Some samples can be slow cooled just by turning the furnace off and letting return to room temperature while others require quenching to ensure the correct phase is made. The conditions of each sample will be discussed in later chapters.

#### 2.5 Successive Ion Layer and Adsorption Reaction

The Successive Ion Layer and Adsorption Reaction (SILAR) is a method that is used to form thin film layers on single crystal substrates. The reaction forms an ionic or ion-covalent compound  $(C_m A_n)$  on the surface of the substrate through epitaxial growth. The substrate acts as a seed crystal for nucleation of the epitaxial film. The reaction is a heterogeneous chemical reaction at the solid-solution surface interface between absorbed cations  $[CL_p]^{n+}$  and absorbed anions  $[AL_q]^m$  as follows:

$$m[CL_p]^{n+} + n[AL_q']^m \rightarrow C_mA_n \downarrow + mpL + nqL'$$
 Equation 2.1

Where  $L_p$  and  $L_q$ ' are different ligands, but do not necessarily need to be.

The SILAR method takes place in four steps. The reaction works by dipping a substrate into a solution of  $[CL_p]^{n+}$  where a Helmholtz electrical double layer is formed on the surface of the substrate. The cation is in the Helmholtz inner layer while the ligand is in the Helmholtz outer layer. After these two layers is the diffusion layer which is rinsed away using high purity water. It is important to rinse the diffusion layer away because if it remains intact  $C_m A_n$  will precipitate into the solution rather than form an epitaxial film. The substrate is then dipped into a solution of  $[AL_q]^m$  and the anion and its' ligand diffuse into the diffusion layer until the concentration is equal to the concentration in the solution. When the anions enter the Helmholtz outer layer they react with the cations forming the  $C_m A_n$ . The substrate is again rinsed with high purity water to remove any remaining ligands or unreacted ions. The first cycle of the four step reaction is complete; several cycles can be carried out until the desired thickness of the film is acquired.

This project did not include the synthesis of thin films, however, core-shell materials were of interest. The SILAR method was altered to accommodate particles as substrates rather than a single crystal wafer. Instead of dipping a substrate into the solutions, powdered samples were stirred in the solutions and then collected by centrifuging the samples and decanting the excess solution. In between each solution, the sample was stirred in deionized water, centrifuged, and decanted. The individual reactions will be discussed in later chapters in greater detail.<sup>3</sup>

### 2.6 Ball Milling

While ball milling is a known technique for synthesizing materials, it was only applied to this project as a method for homogeneous mixing of powders, grinding of ingots, or used to alter particle size of materials. Ball milling allows for an easier method of mixing material, ensuring that the samples are homogeneously mixed. Milling also allows for easy grinding of ingots that are produced from ampoule synthesis. Ball milling has been shown to reduce particle size, some materials are able to reach nano-sized particles. For this project agate jars were used along with

agate beads to mill instead of stainless steel because stainless steel has shown to leave iron (Fe) in samples. A Fritsch planetary micro mill Pulverisette 7 classic line was used. The time, rotational speed, and number of beads were dependent upon the material and desired outcome from milling. Air sensitive samples were loaded in dried jars in a glovebox under nitrogen and sealed with electrical tape. The jars were then placed on the mill with the desired settings and then returned to the glovebox to be collected.

# 2.7 Spark Plasma Sintering

Spark Plasma Sintering (SPS) was not used as a synthetic technique but as a way to densify powders into pellets to be used for later measurements. SPS was done using a Dr. Sinter spark-plasma-sinter machine 211LX. Samples were prepared by placing a graphite rod into one end of the 10 mm diameter graphite die sleeve, then placing a graphite foil spacer, filling the sleeve with powdered sample, placing another graphite die spacer, and then placing the second rod. The graphite foil spacers were used to protect the integrity of the rods. The die set and sample were then loaded into the uniaxial press, on either side of the set an additional graphite rod and carbon spacer were placed between the press and die set, again to protect the integrity of the instrument. Once the sample is in place, a thermocouple is placed into the center of the graphite die sleeve. The pressure, temperature, hold time, and cooling rate are programmable and were dependent upon the sample being pressed. After being pressed and cooled to room temperature, samples were sanded to remove any graphite foil, and then placed on a diamond saw to be cut into appropriately sized pieces for measurements.

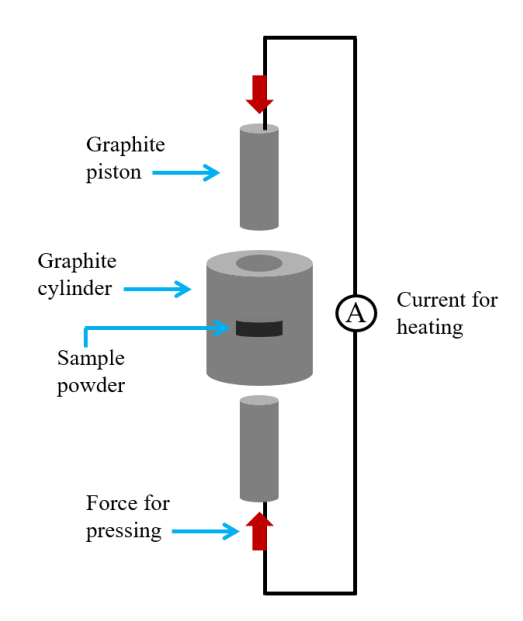


**Figure 2.2** Schematic diagram of spark plasma sintering.

REFERENCES

# **REFERENCES**

- (1) Pechini, M. P. METHOD OF PREPARING LEAD AND ALKALINE EARTH TITANATES AND. 3,330,697, 1967.
- (2) Fahlman, B. D. Materials Chemistry, 2nd ed.; Springer: Dordrecht, 2011.
- (3) Nicolau, Y. F. Solution Deposition of Thin Solid Compound Films by a Successive Ionic-Layer Adsorption and Reaction Process. *Appl. Surf. Sci.* **1985**, *23*, 1061–1074.

#### Chapter 3

#### Introduction to Instrumentation

## 3.1 Powder X-ray Diffraction Theory and Instrumentation

Powder X-Ray Diffraction (PXRD) is a characterization method of structural and phase identification. Diffraction is when light or a wave hits something with periodic ordering and produces constructive interference. Electrons are able to diffract x-rays due to the wavelength of x-rays being the same unit size as the distance between atoms. The strength of diffraction is related to the number of electrons in the atom, the more electrons there are the more intense the diffraction. This allows for x-rays to be used as a way to structurally characterize the periodic arrangement of atoms in materials.

A powder x-ray diffractometer is made up of three basic parts a source, a sample, and a detector. The source is made up of an x-ray tube, a metal filter, and a monochromator. An x-ray tube consists of usually a tungsten (W) filament that is heated with a high voltage to emit electrons. The electrons then strike a metal target, typically copper (Cu) or molybdenum (Mo), and with sufficient energy emit x-rays. Note that all of the PXRD shown in this thesis was produced using Cu  $K_{\alpha}$  with a wavelength of 1.5418 Å. When the metal target is hit a core electron is knocked out of place, this then causes a higher energy level electron to replace it. When an electron decreases in energy levels it has to emit the resulting energy, in this case the energy is from the x-ray region of the energy spectrum.

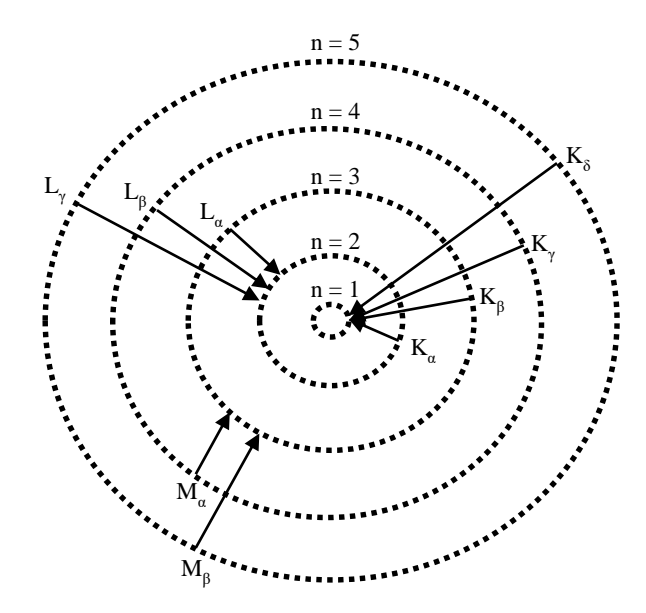


Figure 3.1 Energy levels.

The x-rays emitted will be characteristic of the material and multiple levels of energy can be present causing doublets in the x-ray pattern. To prevent peak doublets from appearing in the pattern a metal filter will be placed to remove the slightly lower energy x-rays. The monochromator is used to ensure than a single wavelength of radiation is used in the incident beam.

A sample for PXRD should be a solid material, however, powder is ideal due to preferred orientation in materials. Preferred orientation is the lack of random orientation of the crystals which can cause changes to the PXRD pattern. To avoid this with powders the samples are packed and the surface of the powder is made smooth, typically with a glass slide.

The detector collects the constructive interference and records the radiation intensities at the varying degrees.

The most basic repeating unit of atoms in any solid with symmetry is called a unit cell. Several repeating unit cells are called a crystal lattice. Unit cell parameters can be described using (a, b, c) as the length of the edges and  $(\alpha, \beta, \gamma)$  as the angles between the edges. The crystal system can be

used to describe the shape of the crystal. There are seven basic crystal lattices that make up the fourteen Bravais lattices that constructs all solids.

**Table 3.1** Describes the fourteen Bravais lattices.

Crystal system	Axial length of the unit cell	Inter axial angles	Number of lattices in the system
Cubic	a = b = c	$\alpha=\beta=\gamma=90^\circ$	3
Tetragonal	$a = b \neq c$	$\alpha=\beta=\gamma=90^\circ$	2
Orthorhombic	$a \neq b \neq c$	$\alpha = \beta = \gamma = 90^{\circ}$	4
Monoclinic	$a \neq b \neq c$	$\alpha=\beta=90^{\circ}\neq\gamma$	2
Triclinic	$a \neq b \neq c$	$\alpha \neq \beta \neq \gamma \neq 90^\circ$	1
Trigonal	a = b = c	$\alpha = \beta = \gamma < 120^{\circ}, \neq 90^{\circ}$	1
Hexagonal	$a = b \neq c$	$\alpha = \beta = 90^{\circ}$ , and $\gamma = 120^{\circ}$	1

Bragg's Law (**Equation 3.1**) relates the angle between in the incident beam and diffracted beam to the spacing between planes of atoms.

$$2d \sin \theta = n\lambda$$
 Equation 3.1

Where d is the spacing between the parallel planes of atoms,  $\theta$  is the angle between the incident beam of x-rays and the reflective x-ray,  $\lambda$  is the wavelength of radiation, and n is the order of Bragg diffraction.

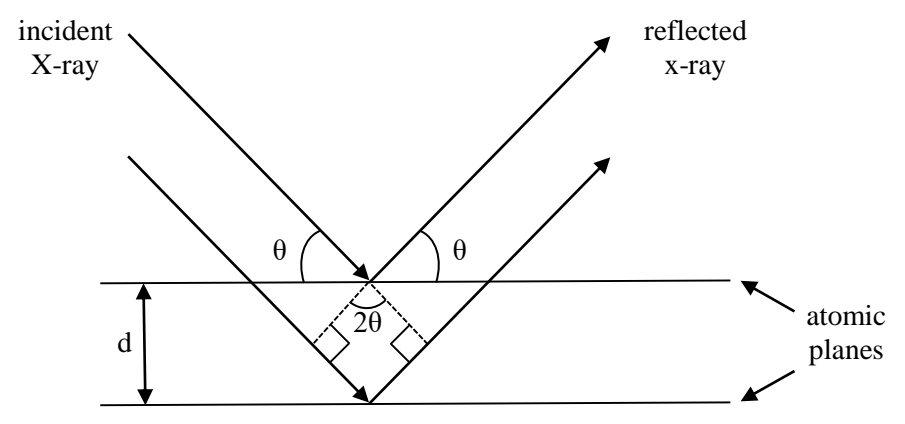


Figure 3.2 A schematic diagram of Bragg's law.

A plane of atoms can then be described using Miller indices (hkl). The Miller indices are the reciprocal vectors of the unit cell; the vector  $d_{hkl}$  is from the origin to the plane of hkl. The  $d_{hkl}$  can then be related to the d-spacing depending on the crystal system.

$$\frac{1}{d_{hkl}^2} = \frac{h^2}{a^2} + \frac{k^2}{b^2} + \frac{l^2}{c^2}$$
 Equation 3.2

This equation becomes much more complicated at the angle of the unit cell change and should be taken into account. For now, only a simple cubic cell will be considered, since all lengths are equal the above equation can be simplified to

$$\frac{1}{d_{hkl}^2} = \frac{h^2 + k^2 + l^2}{a^2}$$
 Equation 3.3

To solve for the Miller indices destructive interference can be taken into consideration. Destructive interference is systematic and which helps determine the crystal system. When taking this into consideration, **Equation 3.3** can be simplified to the following so that only one variable is present to solve for.

$$M^2 = h^2 + k^2 + l^2$$
 Equation 3.4   
  $M = \sqrt{h^2 + k^2 + l^2}$  Equation 3.5

The integer M can then be compared to a table of known values for space groups, which provides the individual values of h, k, and l. While this is proven simple for a cubic system it becomes quite difficult with more complicated crystal systems. Samples are generally matched using a software program such as match!, JADE, or Bruker's DIFFRAC.EVA. These software programs provide ease of matching a sample's diffraction pattern to a Powder Diffraction File (PDF) using the International Centre for Diffraction Database (ICDD).

If a diffraction file is unknown to the data base it can be determined by using Rietveld refinement programs such as Bruker's TOPAS or General Structure Analysis System (GSAS).

The patterns can also give insight into the sample's particle size by using the program PM2K or by using the Scherrer equation, **Equation 3.6**.

$$\tau = \frac{K\lambda}{\beta \cos \theta}$$
 Equation 3.6

Where  $\tau$  is the mean size of the crystalline domains, K is the shape factor,  $\lambda$  is the X-ray wavelength,  $\beta$  is the line broadening at half the maximum intensity (FWHM), and  $\theta$  is the Bragg angle of diffraction. Initially, K is solved for using a standard where  $\tau$  is known, both lanthanum hexaboride (LaB<sub>6</sub>) and corundum (Al<sub>2</sub>O<sub>3</sub>) are common standards with known crystallite sizes. The K value from the standard is then placed into the Scherrer equation and mean crystalline size can be solved for. The Scherrer equation is generally limited to a crystallite size of 0.1  $\mu$ m, which can prove to be difficult with solid state chemistry samples that are generally heated to high temperatures (> 500 °C) which commonly produced micron-sized crystals. While the Scherrer equation can provide some insight to samples it has several limitations that can be overcome by using PM2K software. PM2K software gives a distribution of sizes in the sample and is not limited by the size of the crystals.<sup>1</sup>

## 3.2 Scanning Electron Microscopy

Scanning electron microscopy (SEM) is a structural characterization that shows the surface morphology of a material using secondary electrons. Secondary electrons are produced using the same method as electrons in PXRD by heating a W wire using a high voltage. The difference is instead of using those electrons to hit a target to create x-rays they are concentrated into a beam using negative charges. The beam is then passed through the column and focused using electromagnetic lenses. An Everhart-Thornley detector is used to detect secondary electrons. It is comprised of mainly two parts, a scintillator and a Faraday cage. The Faraday cage is the outermost part of the detector and carries a low positive voltage, 300 volts, to attract the low energy secondary electrons. Once inside the cage the electrons are then attracted to the high positive voltage, 12,000 volts, of the scintillator. The Faraday cage is used so that the high positive voltage of the scintillator does not disturb the electron beam or the images would be blurred. Once the electrons strike the scintillator they emit a photon of light that is then transmitted through a photomultiplier tube. This produces the image the image of the material viewed on a digital screen. SEMs have the ability to show distinct features in the range of 3 nm to 1 mm.<sup>2</sup>

#### 3.2a Backscattered Electrons

Backscattered electron is an option on most SEMs to determine the depth of the materials in the sample. Backscattered electrons are high energy electrons that are a form of elastic scattering, where the electrons leave the same side of the sample they entered. While all materials produce both inelastic and elastically scattered electrons a different type of detector is needed for each since the Everhart-Thornley detector is usually off to the side and the small positive voltage of the Faraday cage is not enough to attract the high energy BSE that are not already traveling in that direction. To detect BSE a scintillator or semiconductor type detector is placed directly over the sample. Heavier elements will produce more back scattered electrons causing a lighter appearance

in the image, while lighter elements will produce fewer creating a darker image. BSE resolution is lower than SE resolution, which will be less than the guaranteed resolution given by the manufacturer. While BSE offers lower resolution it does offer less artifacts appearing in the image due to the high energy of the electrons that are collected to create the image.

# 3.2b Energy Dispersive X-ray Spectroscopy

Energy dispersive x-ray spectroscopy is a form of spectroscopy that is dependent on materials having discrete energy levels. It uses a form of inelastic scattering in which an electron in the k shell of the material is knocked out by the highly energized electrons. An outer electron will then drop down in energy to replace the electron that has been knocked out. The energy released from the electron dropping in energy is distinct for each element making it possible to elementally characterize the material. The spatial resolution of EDS is less than the resolution of both SE and BSE and is around 5 µm.

#### 3.2c Sample Preparation

For samples to be analyzed using SEM they should be electronically conductive although there are ways around this. Samples should also not contain any solvent, for it can be pulled from the sample in the high vacuum and damage the SEM. For powdered materials that are conductive the sample prep is as simple as pouring loose powder over a carbon sticky tab that has been adhered to a metal stub. Solid conductive materials can be adhered to the metal stub using carbon cement. Non-conductive materials should be coated with a conductive material such as, gold, osmium, or carbon. Depending on what information is needed from the sample, the appropriate coating should be selected. All samples for this project were conductive powders, therefore, no coating was used on any of the samples.

## 3.2d High Resolution Scanning Electron Microscopy

High Resolution Scanning Electron Microscopes (HR-SEM) offers higher resolution (1.0 - 1.5 nm) of the samples using a field emission gun. Samples are prepared the same way for this instrument. Gold sputtering should be avoided when using this instrument because the gold nanoparticles are visible. A JEOL 7500F Field Emission Scanning Electron Microscope was used to obtain nanoparticle information for some samples in this thesis.

### 3.3 Transmission Electron Microscopy

Transmission Electron Microscopy (TEM) is similar to SEM in the type of electron source used, however, TEM uses higher energy electrons to emit through the sample. This form of microscopy is still a structural characterization, however, not a topography based one. TEM is mainly used for particle size determination, viewing particle agglomeration, and can be used for single crystal x-ray diffraction. TEMs have a resolution power of 0.2 nm. This method can also be paired with EDS which was discussed in 3.2b.<sup>3</sup>

# 3.3a Sample Preparation

Sample preparation for TEM can be more challenging than other microscopy techniques. Due to the high resolution of the instrument, the samples prepared must be small in size, less than 1  $\mu$ m. In addition to the size constraint if particle size analysis is going to be taken into account then the sample must also be dispersed. Typically, a powdered sample is dispersed in a low boiling point solvent. Then a carbon-coated copper grid is either dipped into the solution or a drop of solution is placed onto the grid. The grids must be handled with care as they are easily bent and the carbon-coating can easily be torn. The grid must be completely dry before being placed into the TEM, just as in SEM the high vacuum can pull the solvent off of the sample holder and damage the instrument. Depending on the solvent and sample, some grids will be heated at low temperatures to ensure that the solvent has been removed from the sample.

## 3.4 Inductively Coupled Plasma Atomic Emission Spectroscopy

Inductively Coupled Plasma Atomic Emission Spectroscopy (ICP-AES) is a technique that characterizes the concentration of metals in a material in the parts per billion to parts per million range. The technique uses an argon (Ar) plasma to excite the metals which are sprayed into the plasma. The metals then emit a characteristic wavelength that corresponds to its particular element, as the material returns to ground state. The intensity of the emission corresponds to the concentration of the metal.

All samples and standards need to be in liquid form so that they can be sprayed into the plasma. Samples are typically dissolved in an acidic solution, typically 2 % nitric acid (HNO<sub>3</sub>), to be comparable to the standard samples that are prepared. Since some samples are stable enough that that is too dilute an acid to dissolve them the samples were dissolved in aqua regia, a four-part mixture of hydrochloric acid (3 part) and nitric acid (1 part). These solutions where then diluted down to 2 % to be compatible with the standards.

Varying concentrations of standard solutions are prepared and measured using the ICP-AES to make a calibration curve. The samples are then made at varying concentrations between the concentrations of the standards to determine the concentration of the metal in the sample.

### 3.5 Thermogravimetric Analysis and Differential Scanning Calorimetry

Thermogravimetric Analysis (TGA) measures the weight loss of a sample over a constant temperature using different gases. The TGA instrument is paired with a Differential Scanning Calorimeter (DSC). A DSC measures the amount of heat needed to keep the sample the same temperature as the reference. This measurement allows for endothermic and exothermic events to be measured as a function of temperature. The pairing of these two techniques can provide insight as to how the sample reacts in reducing, oxidizing, or inert atmospheres. It can be used to help

explain the endothermic and/or exothermic events, phase transitions, or even the temperature at which a material crystalizes.

### 3.6 Diffuse Reflectance Infrared Fourier Transform Spectroscopy

To discuss Diffuse Reflectance Infrared Fourier Transform Spectroscopy (DRIFTS) it is important to briefly discuss Fourier Transform Infrared Spectroscopy (FTIR) first. FTIR is a spectroscopy method that exploits that molecules will absorb frequencies that are the same as the vibrational frequencies occurring within the sample. The technique is labeled as such because it measures these frequencies in the infrared region (14000 – 10 cm<sup>-1</sup>) of the electromagnetic spectrum. The region can be broken up into three common regions near- (14000 – 4000 cm<sup>-1</sup>) mid- (4000 – 400 cm<sup>-1</sup>) and far- (400 – 10 cm<sup>-1</sup>) infrared. For the purpose of this discussion, the range will be limited to the mid-infrared region. The instrument uses a source near the IR region to create an illumination beam to be directed towards the sample. The sample then absorbs common frequencies and transmit the rest to be measured. Fourier transform implies that instead of individual frequencies being passed through the sample, several a shown on the sample at once. The instrument then mixes the frequencies and shines them on the sample again. The instrument then uses a mathematical logarithm to determine the absorptions that occurred at each frequency. This technique typically utilizes specular reflectance due to the smooth surface of the sample.

FTIR sample prep typically utilizes a powdered sample mixed with a non-absorbent matrix, such as potassium bromide (KBr) to dilute the sample. The sample and non-absorbent matrix are hand ground and then pressed into a pellet to be placed into the instrument. FTIR can be used for liquids and gases, however, that will not be discussed in this content.

Diffuse reflectance occurs when a sample has rough edges and scatters in multiple directions as opposed to specular reflectance utilizing a smooth surface. DRIFTS makes use of this scattering by using an integrated sphere to detect the variable scattering.

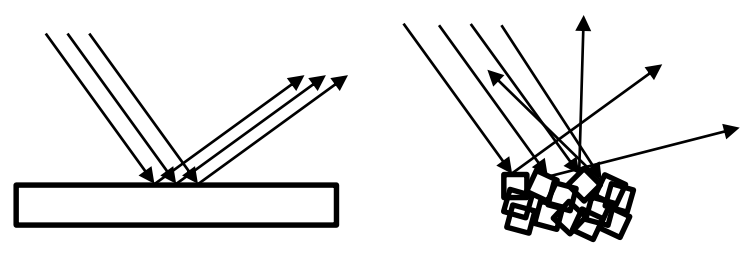


**Figure 3.3** A schematic diagram of specular versus diffuse reflectance.

DRIFTS can be applied to inorganic samples to exploit the energy needed to create a transition across the band gap.

No sample prep is needed unlike traditional FTIR, instead the powdered sample is placed into a cup like sample holder. If the sample is too absorbent, then the sample can be diluted with a non-absorbent matrix just like in FTIR. Ideal samples would have a particle size smaller than  $10 \mu m$ , the size of the incident radiation.

## 3.7 Archimedes Density Measurement

The Archimedes method was used to determine the density,  $\rho$ , of samples that were in pellet form from SPS. The Archimedes principle states that the weight of the sample in liquid is equal to the weight of the sample's volume. The method first measures the temperature of the ethanol to determine the density of the ethanol. Then the sample is weighed in air and a second time in ethanol. The weights were then used to calculate the density of the sample using the following equation.

$$\rho = \frac{A}{|P|} \rho_E$$
 Equation 3.7

Where A is the weight of the sample in air, |P| is the weight of the sample in ethanol, and  $\rho_E$  is the density of the ethanol at the temperature record. The density of thermoelectric samples is needed for other measurements which will be discussed in later sections.

## 3.8 Seebeck Coefficient and Resistivity

The Seebeck coefficient,  $\alpha$ , and the electrical resistivity,  $\rho$ , are measured together using two different instruments; one for low temperature (80 – 300 K) and one for high temperature (300 K – 580 K) measurements. For these measurements a sample is spark plasma sintered into a dense pellet and then cut into a rectangular shape. The Seebeck coefficient is measured by heating the sample to a temperature and then applying a temperature gradient across the pellet and measuring the thermal electromotive force. The same instrument is used to measure the electrical resistivity by applying a constant electrical current to two ends of the sample and measuring the voltage difference along its length. Each measurement regardless of high temperature or low temperature takes place under a vacuum atmosphere. The mounting of each sample is different and will be explained in the subsequent sections.

# 3.8a Low Temperature Measurements

For low temperature measurements two thin copper wires are epoxied going across the length of the rectangular pellet. The sample is set into an oven at 200 °C to set the epoxy. The rectangular pellet is vertically attached to a copper piece with silver epoxy and a heating mantle is attached to the top of the piece and the sample is again set into an oven at 200 °C to set the epoxy. Next a thermal grease is placed on the mount and the sample is screwed in place with a wire going under the copper base. Then four wires are soldered to the sample, attaching to the copper wire pieces and to the heating mantle on the top of the sample. These connections work to create a temperature gradient across the sample for the Seebeck coefficient measurement and to measure the resistivity across the sample.

Low temperature measurements presented in this thesis were done using a house made system that is Janis based and was connected to a cryostat.

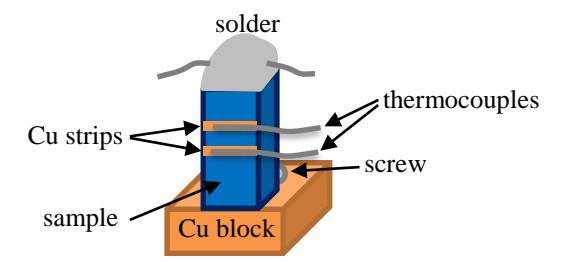


**Figure 3.4** A schematic diagram of a low temperature holder with sample and connections.

## 3.8b High Temperature Measurements

The base of the sample holder is made of carbon, a carbon block filler piece is placed on top of the base to both boost the height of the sample and in case the sample reacts with carbon the instrument is protected. The sample is then balanced on top of the carbon block with an additional carbon block being placed on top of the sample to protect the upper part of the sample holder. The sample holder is then slowly moved to clamp all of the pieces in place. Two spring loaded thermocouples are then moved in until they rest against the sample.

High temperature measurements presented in this thesis were made using an ULVAC ZEM-3 system.

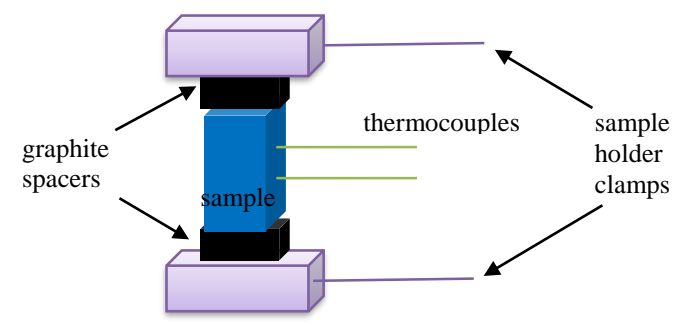


**Figure 3.5** A schematic diagram of a high temperature holder with sample and connections.

## 3.9 Laser Flash Analysis

Laser Flash Analysis (LFA) is used to measure the thermal diffusivity, a, of a sample. A disk shaped pellet is cut from the spark plasma sintered sample. The sample is then sanded to 1.0-1.5 mm thickness for this measurement and measures 10 mm in diameter. The instrument applies heat to one side of the disk and measures the time it takes for the heat to diffuse to the other side of the sample. The thermal diffusivity, can then be related to thermal conductivity,  $\kappa$ , through the following relationship.

$$A = \frac{\kappa}{\rho c_p}$$
 Equation 3.8

Where  $\rho$  is the density of the material and  $c_p$  is the specific heat of the sample. All diffusivity measurements presented in this thesis were done on a Netzsch LFA 457 Microflash instrument.

#### 3.10 Hall Effect Measurements

Hall effect measurements provide a method of calculating the carrier concentration, n, as well as the mobility,  $\mu$ , of the carriers from measuring the Hall voltage. Carriers refers to charge carriers which can be either electrons or holes depending on the material. When a voltage is passed across an electric conductor in the x-axis direction and a magnetic field is applied perpendicular to the electric current, then a voltage will occur transverse to these two fields. The voltage that is created is referred to as the Hall voltage.

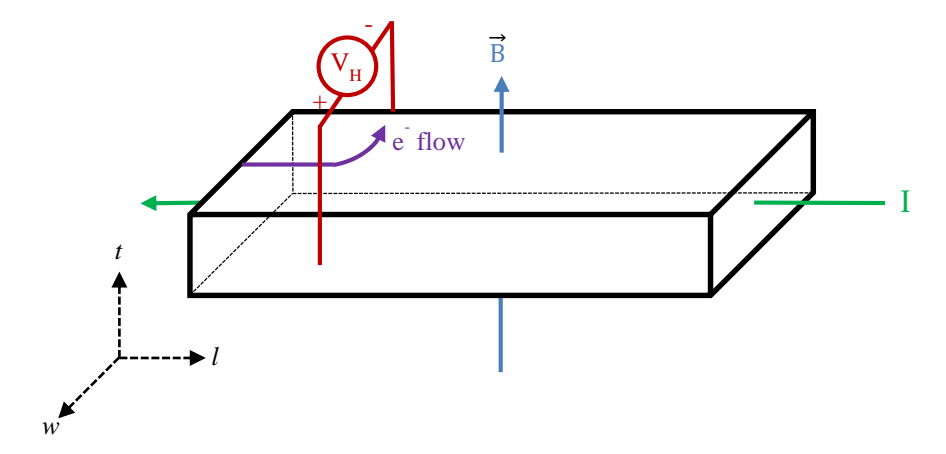


Figure 3.6 A schematic diagram of Hall effect measurement.

When a magnetic field is applied to an electric current a force referred to as the Lorentz force,  $\vec{F}$ , is created which follows the right hand rule of direction. The Lorentz force can be described by the following equation:

$$\vec{F} = q_0 \vec{E} + q_0 \vec{v} \times \vec{B}$$
 Equation 3.9

where  $q_0$  is the magnitude of the charge,  $\vec{E}$  is the electric field,  $\vec{v}$  is the velocity of the charge carriers and  $\vec{B}$  is the magnitude of the magnetic field. Note that all of the variables except the magnitude of the charge are vectors and are therefore directionality is important. The force causes the carries to build up on one side of the material creating an electric potential across to the material which is the Hall voltage. When the electric potential is formed the Lorentz force is balanced and the system is in a steady state where no force is acting upon the carriers, allowing the voltage to be measured. The Hall voltage,  $V_H$ , can then be represented as the following equation:

$$V_H = v_d w B$$
 Equation 3.10

where  $v_d$  is the drift velocity, w is the width of the material in the direction the  $V_H$  is being produced. The equation shows that the Hall voltage is directly proportional to the magnitude of the magnetic field. Current, I, can then be represented by the following:

$$I = q_0 nwtv_d$$
 Equation 3.11

where n is charge carrier concentration (sometimes referred to as charge carrier density), and t is the thickness of the sample. Bringing **Equation 3.10** and **Equation 3.11** together the Hall voltage can be written as:

$$V_{H} = \frac{IB}{q_{0}nt}$$
 Equation 3.12

Rearranging **Equation 3.12** for carrier concentration, the following is obtained:

$$n = \frac{IB}{V_H q_0 t}$$
 Equation 3.13

The carrier mobility is defined as:

$$\mu = \frac{1}{nq_0}$$
 Equation 3.14

Bringing **Equation 3.13** and **Equation 3.14** together, the carrier mobility can be calculated using the following equation:

$$\mu = \frac{V_H t}{BI\rho}$$
 Equation 3.15

Samples for Hall measurement have been spark plasma sintered and are cut into rectangular pellets. The samples should be about 1.0 mm in thickness. The sample is mounted lying flat on the largest face of the rectangular pellet. Using silver epoxy five platinum wires are attached to the sample to measure the resistivity as well as the Hall voltage. Hall measurements presented in this thesis were done using a house made system that is Lakeshore based and was connected to a cryostat.<sup>4</sup>

REFERENCES

#### REFERENCES

- (1) Percharsky, V. K.; Zavalij, P. Y. Fundamentals of Powder Diffraction and Structural Characterization of Materials, 2nd ed.; Springer: New York, 2009.
- (2) Flegler, S. L.; Heckman, J. W.; Klomparens, K. L. *Scanning and Transmission Electron Microscopy an Introduction*, 1st ed.; Oxford University Press: New York, 1993.
- (3) Egerton, R. F. *Physical Principles of Electron Microscopy, an Introduction to TEM, SEM, and AEM,* 1st ed.; Springer: New York, 2005.
- (4) Ramsden, E. *Hall-Effect Sensors: Theory and Application*, 2nd ed.; Newnes: Burlington, 2006.

#### Chapter 4

Synthesis of Bulk Thermoelectric Materials with Low Dimensionality

## 4.1 Synthesis: Successive Ion Layer and Adsorption Reaction

The SILAR technique was selected as the method to synthesize core-shell nanoparticles in large quantities. As discussed in a prior section the method was altered to accompany particles rather than films. Two sets of reactions were done using the SILAR method, the first used degassed water as a solvent, and the second utilized tetraethylene glycol dimethyl ether (tetraglyme) as a solvent. All materials were purchased from either Sigma Aldrich or Alfa Aesar and were at least 99.9+ % purity.

For the first set both CdS and PbS were purchased and used as is to be tried as cores for the coreshell materials. For the CdS cores, aqueous lead nitrate (Pb(NO<sub>3</sub>)<sub>2</sub>) was utilized as the cation source, and aqueous sodium sulfide nonahydrate (Na<sub>2</sub>S·9H<sub>2</sub>O) was used as the anion source for the shell material.

$$CdS + Pb^{2+} + S^{2-} \longrightarrow CdS/PbS$$
 (core/shell) **Equation 4.1**

For the PbS cores, aqueous cadmium chloride (CdCl<sub>2</sub>) was utilized as the cation source, and aqueous sodium sulfide nonahydrate (Na<sub>2</sub>S·9H<sub>2</sub>O) was used as the anion source for the shell material.

$$PbS + Cd^{2+} + S^{2-} \longrightarrow PbS/CdS$$
 (core/shell) **Equation 4.2**

At room temperature in a purge box, purged with nitrogen gas (N<sub>2</sub>) the aqueous cation solution was added to the core material and hand shaken in a vial for approximately 30 seconds. The powder was then allowed to settle and the excess liquid was pipetted from the vial. To wash the excess cations from solution, degassed water was then added to the vial, hand shaken for approximately 30 seconds, the powder was allowed to settle, and the excess liquid was pipetted from the solution.

This was repeated for the aqueous anion solution, which concludes one cycle of SILAR. The cycle was repeated twenty times for each sample.

For the second set of samples that were done using tetraglyme, cation sources remained the same however, the anion source was dried to become sodium sulfide (Na<sub>2</sub>S). All reactions in the second set were able to be done in a glovebox under a nitrogen atmosphere, which allowed the samples to be centrifuged for ease of decanting the excess liquid. The results for both sets of reactions are summarized in the following section along with a discussion of the characterization results.

#### 4.2 Results and Discussion

**Table 4.1** Summary of parameters used for both sets of SILAR reactions and the powder X-ray diffraction results.

Sample number	Core	Cation source	Anion source	Solvent	Decant method	PXRD results
1	CdS	$Pb(NO_3)_2$	$Na_2S\cdot 9H_2O$	water	pipet	PbS, CdS
2	PbS	CdCl <sub>2</sub>	Na <sub>2</sub> S·9H <sub>2</sub> O	water	pipet	PbS
3	CdS	Pb(NO <sub>3</sub> ) <sub>2</sub>	Na <sub>2</sub> S·9H <sub>2</sub> O	water	pipet	PbS, CdS
4	CdS	Pb(NO <sub>3</sub> ) <sub>2</sub>	Na <sub>2</sub> S	tetraglyme	centrifuge	PbS, CdS
5	PbS	CdCl <sub>2</sub>	Na <sub>2</sub> S	tetraglyme	centrifuge	PbS

From the summarized results in **Table 4.1** it can be noted that only CdS core reactions were able to produce the desired shell compound. The phases were identified using PXRD.

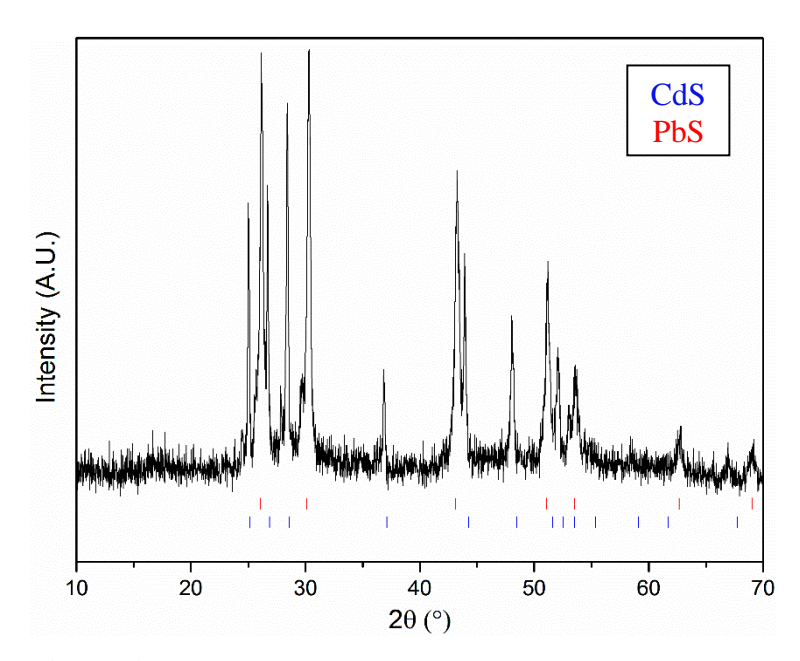


**Figure 4.1** PXRD pattern for sample 3 showing both CdS and PbS phases.

For samples that showed both the core and shell material, SEM and BSE were done to prove whether or not the samples formed core-shell materials or if the shell material precipitated separately forming a binary system. Several areas of sample were analyzed for each sample and showed similar results which will be discussed for sample 3 for continuity. Smooth areas were used for sampling to ensure that the shell would be seen if endotaxially grown onto the core. BSE was used to determine the uniformity of the composition of the sample. As shown in **Figure 4.2** the sample was smooth and the composition of the sample was homogeneous which would give rise to the sample being core-shell.

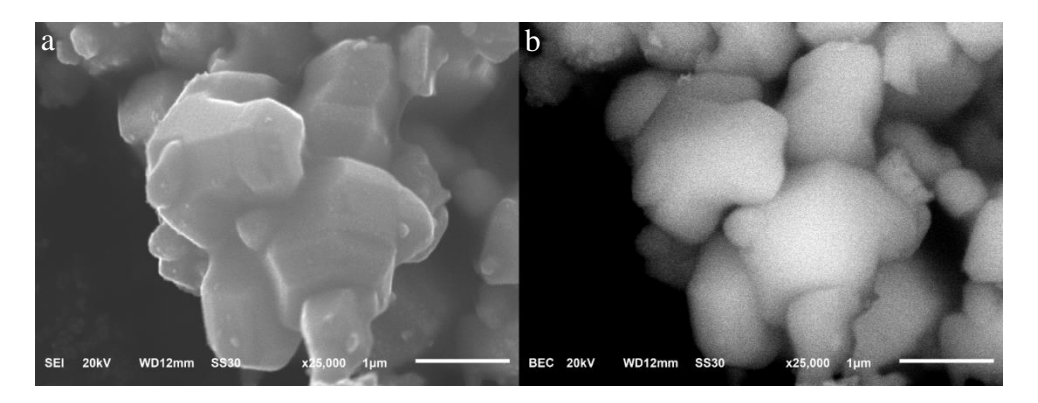
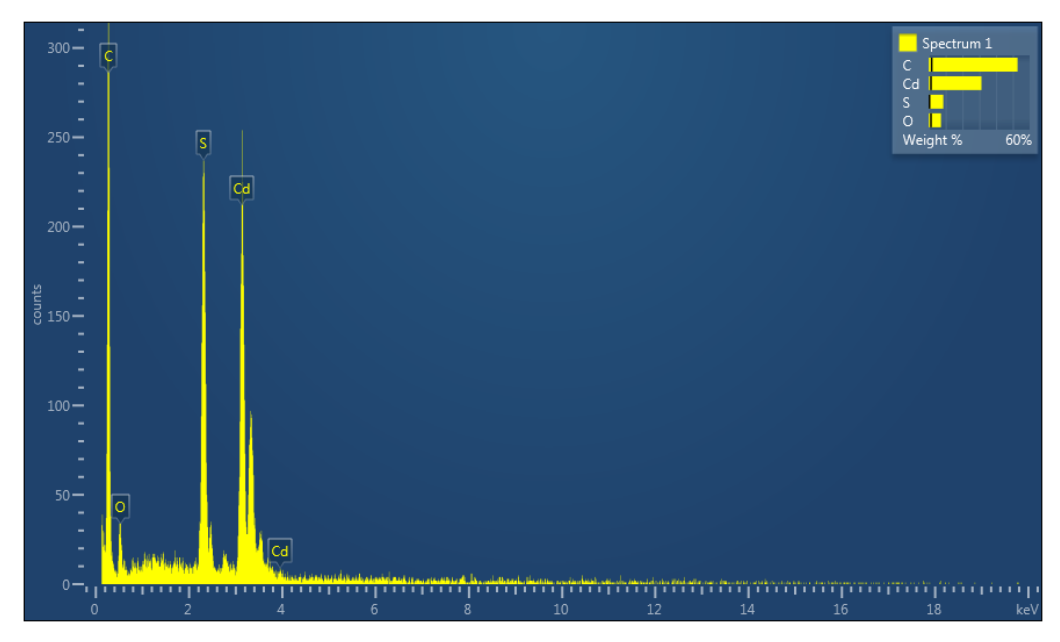


Figure 4.2 a. SEM image of sample 3 and b. BSE image of sample 3.

For each sample several areas were measured using EDS to ensure of the samples being core-shell.

A sample of an EDS spectrum for sample 3 is shown in **Figure 4.3**.



**Figure 4.3** EDS spectrum for sample 3 corresponding to **Figure 4.2** and showing the sample was composed of CdS.

For samples 1, 3, and 4 it was determined that core-shell materials were not formed, instead PbS precipitated from the solution creating a binary system. Separate areas of CdS and PbS were found in each sample, however, the two compounds never appeared on the same crystals.

Initial attempts at utilizing SILAR for powder materials were unsuccessful. It was determined that some parameters could be varied to determine why the samples were forming a binary system rather than core-shell materials. Some of the parameters that could be varied would be solvent

choice, number of cycles, temperature, as well as, core particle size. To try and narrow the scope of what would be altered, it was determined that core particle size would be varied.

## 4.3 Synthesis: Co-precipitation

A co-precipitation method was utilized to try and synthesize nanosized core materials. Each solution used methanol as a solvent to dissolve salts. A 125 mL solution of 0.044 M CdCl<sub>2</sub> and 0.045 M Pb(NO<sub>3</sub>)<sub>2</sub> was slowly titrated, approximately one drop per second, with 150 mL of 0.073 M sodium telluride (Na<sub>2</sub>Te). The reaction was done in a nitrogen atmosphere in a glovebox.

$$Pb^{2+} + Cd^{2+} + Te^{2-} \longrightarrow PbTe_{(s)} + CdTe_{(s)}$$
 Equation 4.3

The sample was centrifuged to separate the solvent from the precipitated powder formed. The excess liquid was decanted and the powdered was dried under vacuum for 5-10 minutes.

#### 4.4 Results and Discussion

A total of 2.9104 grams of sample were collected, giving a 91.3 % yield using this method. The PXRD pattern showed that both PbTe and CdTe were formed, in a cubic lattice. Since the peaks

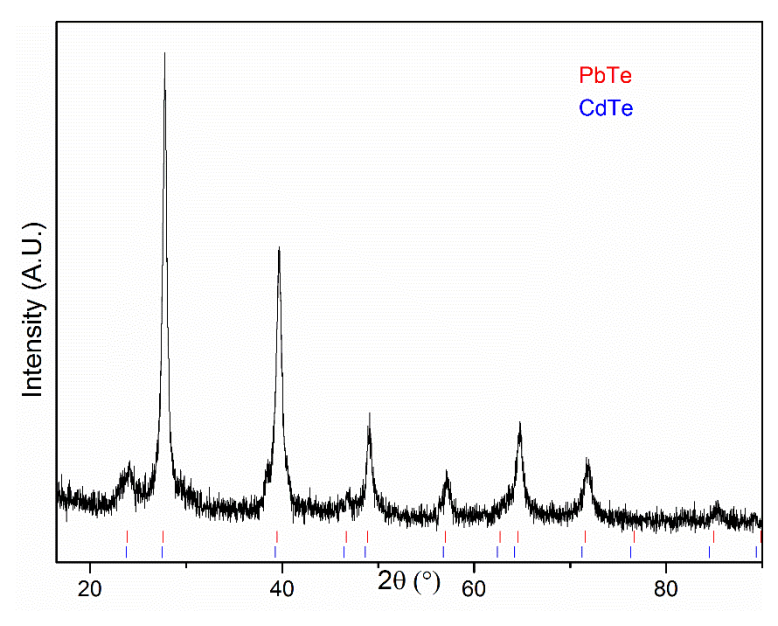


**Figure 4.4** PXRD pattern for co-precipitation method showing both PbTe and CdTe phases.

overlap for the cubic structures, EDS was used to determine that both PbTe and CdTe were present

in the sample. The PXRD showed broad peaks which can be indicative of small particle size, so the sample was prepped for TEM. TEM showed agglomerated nanoparticles of both PbTe and CdTe.

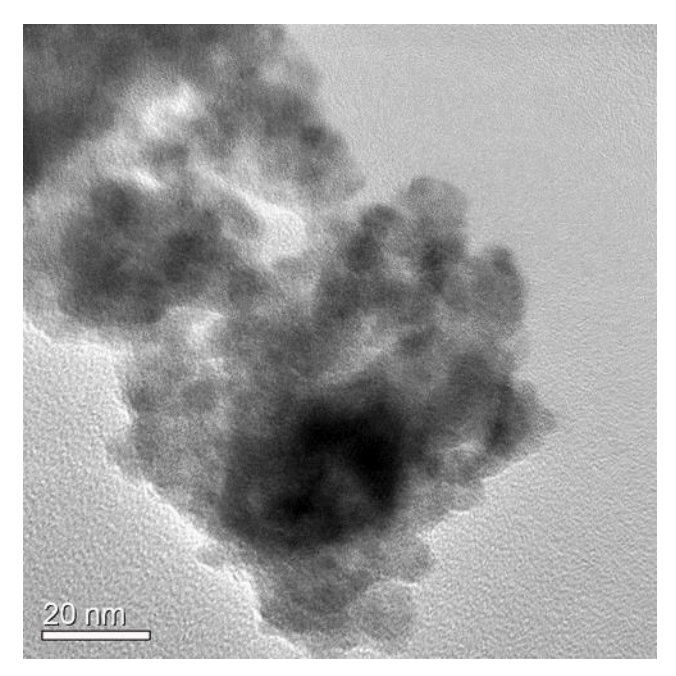


**Figure 4.5** TEM image of co-precipitation, showing both PbTe and CdTe nanoparticles.

The particles were varying in size with the majority being 20 nm or less in size.

Co-precipitation was able to give a viable route for synthesizing nanosized particles of both PbTe and CdTe. The method was able to produce a large quantity of sample however, was very tedious in how slow the precipitation proceeded to ensure small particles. It was determined that while this method could provide small particles it would be ineffective when it came to doping samples. Up until this point all approaches could be considered bottom-up approaches, could a top-down approach allow for ease of synthesis for these materials? To attempt a top down approach would mean a method would be needed that could take the desired bulk sample and manipulate it for a preferred nano product.

# 4.5 Effect of Ball Milling on Particle Size

It is well known that ball milling can alter the size of materials, decreasing particle size to some limit, which would allow for a top-down approach. This method would allow purchased micron-size particles to be milled until nanometer sized. To ensure ball milling would be efficient in creating nanosized particles for cores a series of experiments were run, the resulting samples were then PXRD and the pattern was processed using PM2K software to show a size distribution of particles. Approximately 3.0 grams of PbTe was placed in an agate jar with 4 agate beads to be milled at 400 rpm for 30 minutes, 60 minutes, 2 hours, 4 hours, and 8 hours.

#### 4.6 Results and Discussion

PXRD showed general broadening of peaks the longer the samples were milled. Before milling the purchased material had an average particle size of 80 nm. As the samples were milled the average particle size decreased until an approximate limit of 30 nanometers. Although ball milling allowed for the average particle size to decrease there remained a vast distribution of particle sizes in each sample, as shown in **Figure 4.6**.

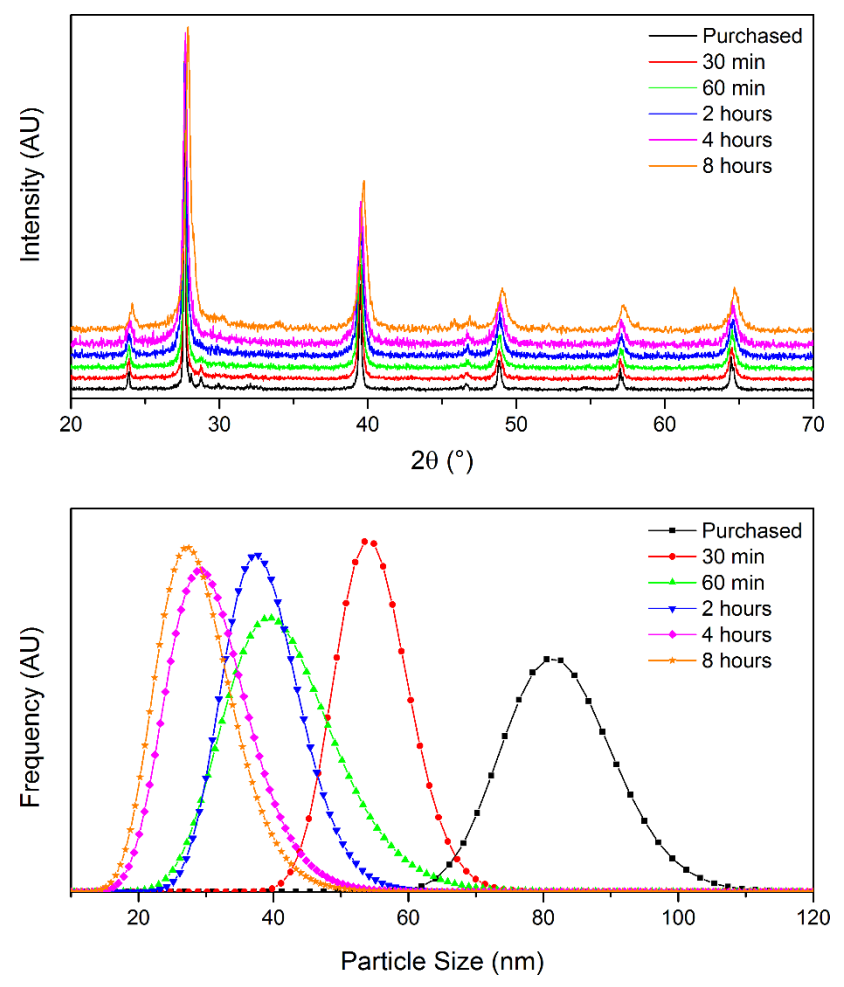


**Figure 4.6** PXRD pattern and PM2K calculated size distribution results for the ball milling of purchased PbTe over various milling times.

In addition to calculation software, TEM was done to ensure the accuracy of the software. TEM agreed with the PM2K software that after milling for four hours the particles were an average of 30 nm.

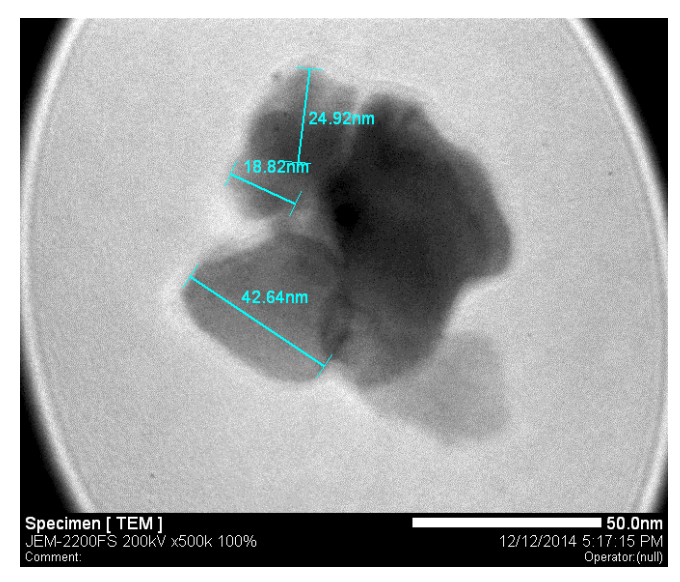


**Figure 4.7** TEM image, and measurement of particles after four hours of ball milling.

Ball milling offers an alternative route to obtaining nanoparticles. This route allows for materials to be either purchased or synthesized on the micron-scale, and milled down to nanometer scale. Since the materials should be doped nanoparticles, a bulk synthesis that allows for ease of doping should be sought.

### 4.7 Synthesis: Sol-gel

It was established for the first time that sol-gel method could be used as a method to produce bulk amounts of doped material. A procedure was established for synthesis of both lead telluride and cadmium telluride. For the synthesis of lead telluride lead was dissolved separately first by adding 0.015 mol of Pb to 4 mL of nitric acid. The lead solution is then mixed with an aqueous solution of 0.015 mol of telluric acid (Te(OH)<sub>6</sub>) and 0.20 mol of citric acid. The solution was allowed to stir until it became transparent, then 10 mL of ethylene glycol was added. The solution is then allowed to stir for 24 hours, and then slowly heated on the hotplate until the solution becomes gel like. Heating temperatures for the sample were determined by TGA-DSC. It was determined from the TGA-DSC curve that the solution should be heated to 420 °C. The gel was heated over six hours to 420 °C, held at temperature for 12 hours, and then allowed to cool to room temperature.

A gray powder was collected and hand ground before being placed into a reducing atmosphere. Loose powder was placed in an alumina boat in between two alumina boats filled with  $P_2O_5$  and heated in a quartz tube under  $H_2$  flow to 350 °C for 48 h to ensure that all carbonates are removed from the powder.

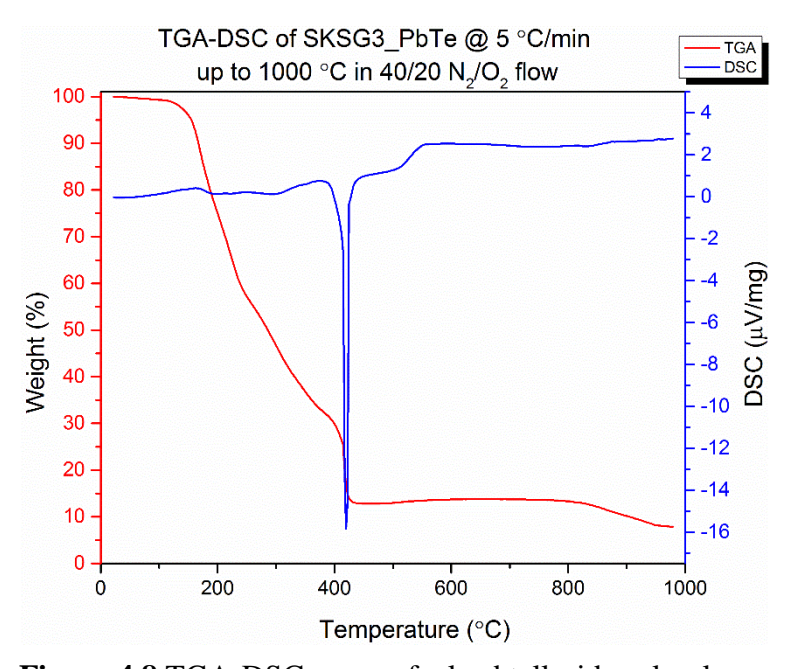


**Figure 4.8** TGA-DSC curve of a lead telluride sol-gel.

A similar procedure was established for the synthesis of cadmium telluride. An aqueous solution was made by adding 0.02 mol of cadmium acetate dehydrate (Cd(OOCCH<sub>3</sub>)<sub>2</sub>•2H<sub>2</sub>O), 0.02 mol of (Te(OH)<sub>6</sub>), 0.2 mol of citric acid, and 4 mL of nitric acid. The solution was allowed to stir until it became transparent, then 10 mL of ethylene glycol is added. The solution is then allowed to stir for 24 hours, and then slowly heated on the hotplate until the solution becomes gel like. Heating temperatures for the sample were determined by TGA-DSC. It was determined from the TGA-DSC curve that the gels should be heated to 500 °C. The gel was heated over six hours to 500 °C, held at temperature for 12 hours, and then allowed to cool to room temperature. A gray powder was collected and hand ground before being placed into a reducing atmosphere. Loose powder was

placed in an alumina boat in between two alumina boats filled with  $P_2O_5$  and heated in a quartz tube under  $H_2$  flow to 350 °C for 48 h to ensure that all carbonates are removed from the powder.

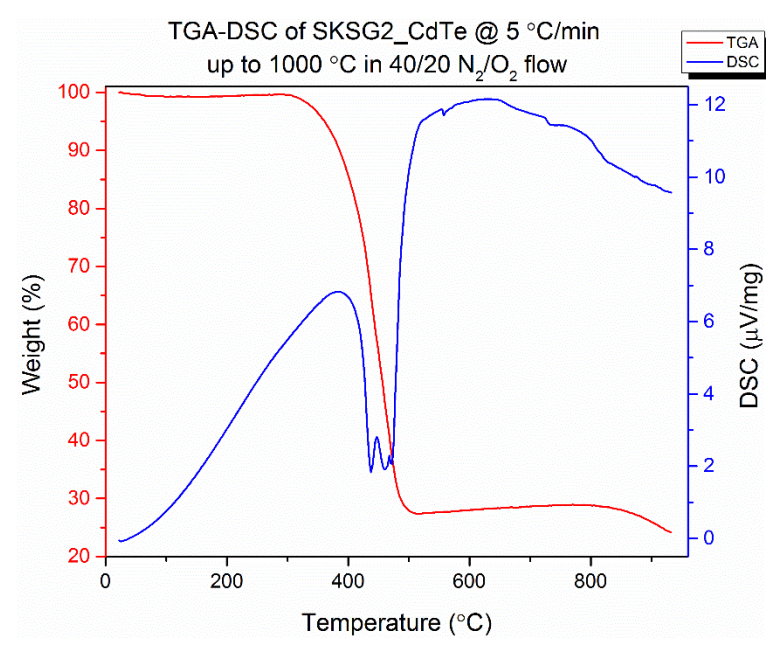
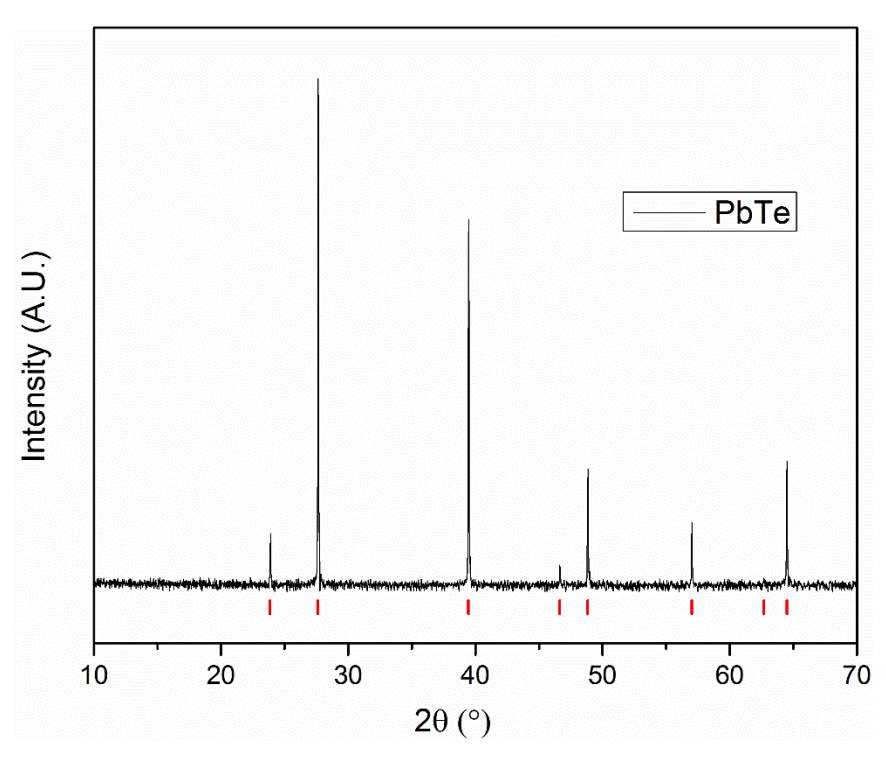


Figure 4.9 TGA-DSC curve of a lead telluride sol-gel.

### 4.8 Results and Discussion

After being heated in a reducing atmosphere the materials were characterized via powder x-ray diffraction measurement to determine the purity of the samples. The PXRD pattern of both PbTe and CdTe showed that the samples were pure.



**Figure 4.10** PXRD pattern of PbTe, synthesized by the sol-gel method.

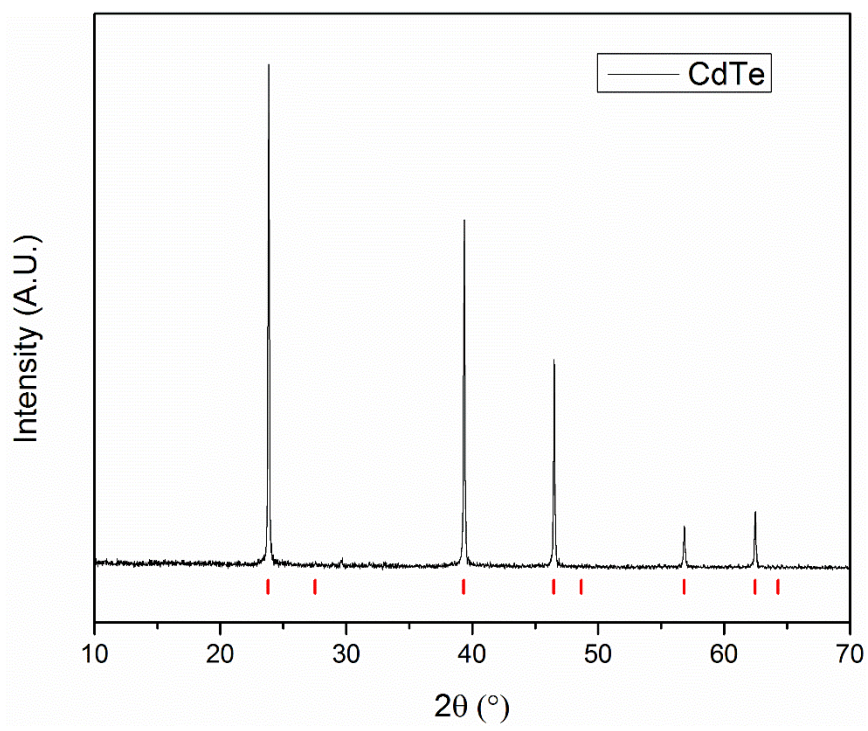


**Figure 4.11** PXRD pattern of CdTe synthesized by the sol-gel method.

After it was shown that the sol-gel could be exploited to produce 3-5 grams of each materials, the synthesis was redone with 2 % sodium (Na) doping. The PXRD pattern of either sample doped samples did not appear different than the PXRD pattern of the undoped samples due to the low percentage of doping.

Following the synthesis of both 2 % sodium doped PbTe and 2 % sodium doped CdTe, the samples were individually ball milled to generate nanoparticles. The samples were milled at 500 rpm, milling for 5 minutes, pausing for one, and set to repeat for 48 times, for a total of 4 hours of milling. The samples were milled in agate jars along with agate beads instead of stainless steel to ensure the samples would not be contaminated with iron from the jars and beads.

After generating nanoparticles of doped materials, a series of spark plasma sintering experiments was performed to determine an optimal heating temperature. The goal of this was to control particle growth as much as possible while sintering the samples to high density pellets. A 1:1 mole ratio of 2 % sodium doped PbTe and 2 % sodium doped CdTe was ball milled together for the SPS experiment and labeled as SKBM13\_KWSG5\_KWSG6. Sample SKBM11\_KWSG5\_KWSG6 was split into three separate samples to be tested at varying temperatures (300 °C, 427 °C, and 550 °C). Each sample was heated at a rate of 100 °C/min, and held for 5 minutes under approximately 40 MPA (2.1 kN). Following SPS, the samples were sanded and cut for Seebeck and resistivity measurements. Before measurements, the samples were examined using DRIFTS to determine if quantum-confinement was present as well as HR-SEM to determine if nano scale sizes of particles were preserved.

Three 1:1 mole ratio of 2 % sodium doped PbTe and 2 % sodium doped CdTe samples were analyzed via DRIFTS: a hand ground sample, a ball milled sampled, and a SPS sample. The graphs were normalized to 0.4227 eV.

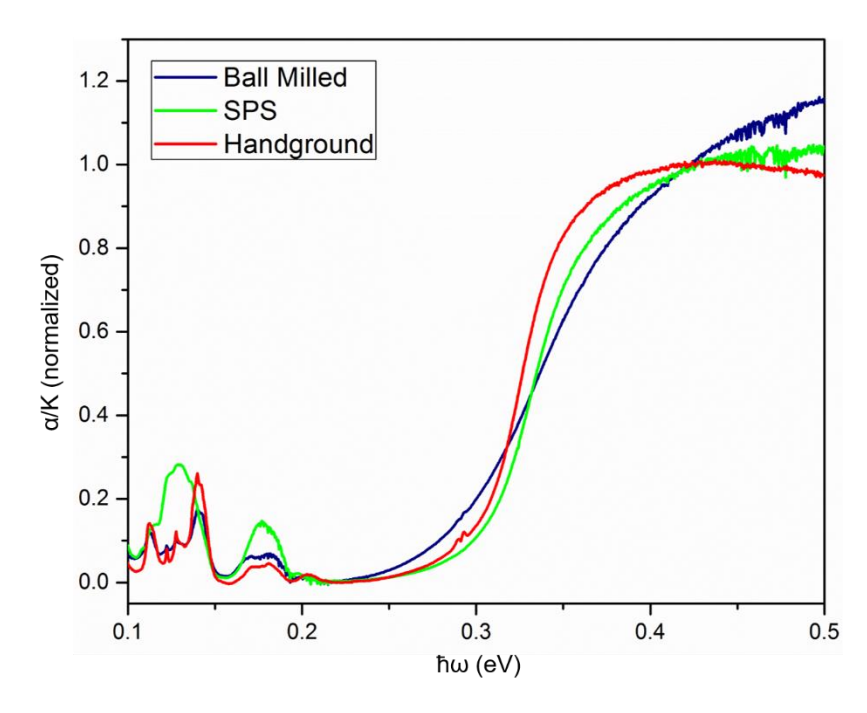


**Figure 4.12** Normalized Kubelka Munk function for raw data for three 1:1 mole ratio of sodium doped lead telluride to sodium doped cadmium telluride samples synthesized via sol-gel.

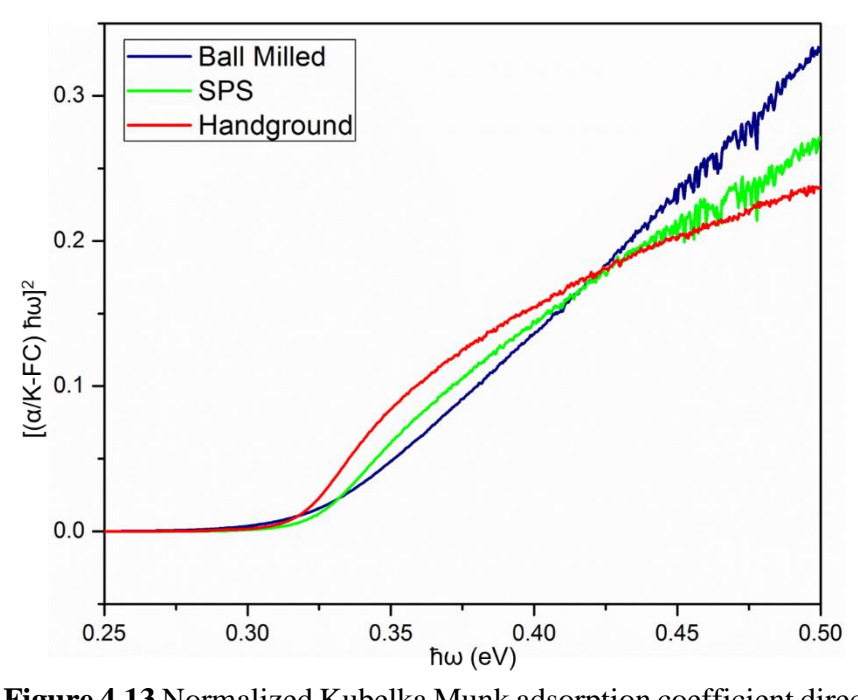


**Figure 4.13** Normalized Kubelka Munk adsorption coefficient direct gap fit for three 1:1 mole ratio of 2 % sodium doped lead telluride to 2 % sodium doped cadmium telluride samples synthesized via sol-gel.

The adsorption coefficient was calculated using Kubelka Munk analysis  $F(R) = \frac{\alpha}{K} = \frac{(1-R)^2}{2R}$  where R is the fractional reflectance,  $\alpha$  is the adsorption coefficient, and K is the scattering coefficient. The results of DRIFTS confirmed that the materials were not quantum-confined by ball milling or after SPS. There was minimal shift in the energy when the curves were extrapolated to the x-axis of the graph. It was determined that all of the samples produced by sol-gel and treated by ball milling contained agglomerated particles. This was seen both by HR-SEM as well as TEM.

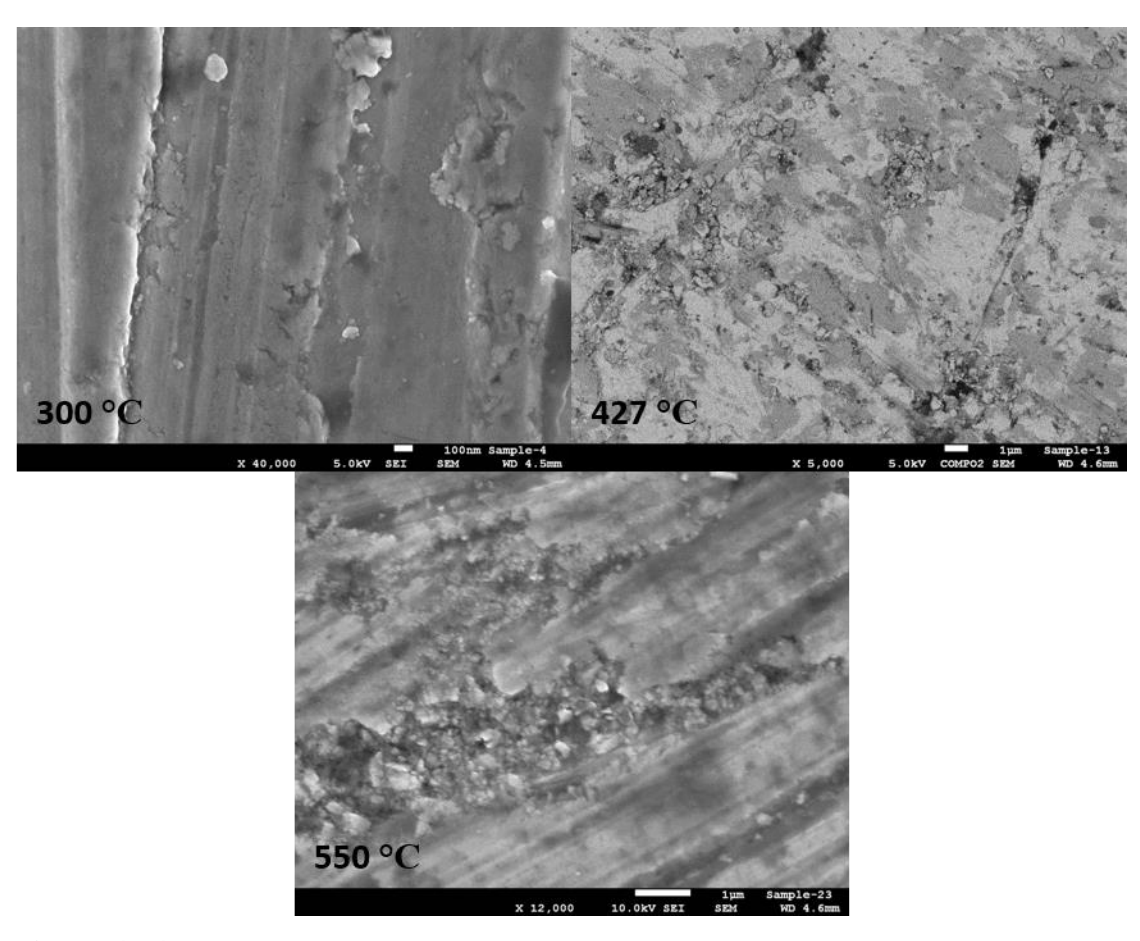


**Figure 4.14** HR-SEM images of sample SKBM13\_KWSG5\_KWSG6 SPS at varying temperatures to determine nano-scale integrity.

From the HR-SEM images it was determined that some nanoparticles remained intact, however, there was a great deal of agglomeration and micron-sized grain boundaries in all three samples.

Despite these results it was decided that the 300 °C sample should still be measured for the Seebeck coefficient and resistivity to have a comparison for future samples. To determine if particle growth would be a concern during measurements the sample was run three times to 600 °C, in the forward and reverse direction to determine if there was an effect on the measurement.

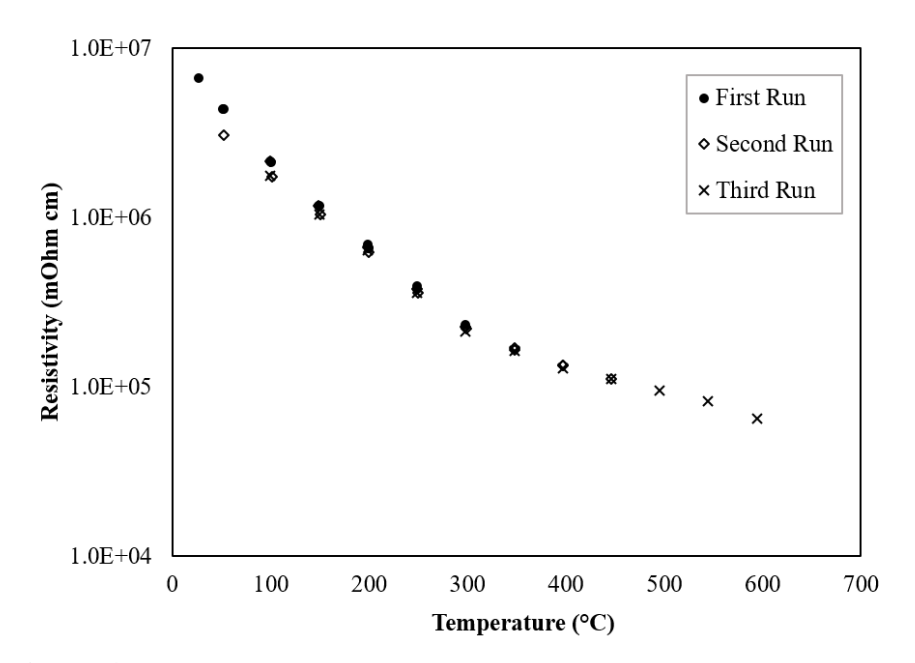


**Figure 4.15** Plot of resistivity versus temperature for 550 °C SPS sample, synthesized via sol-gel, run three times for comparison.

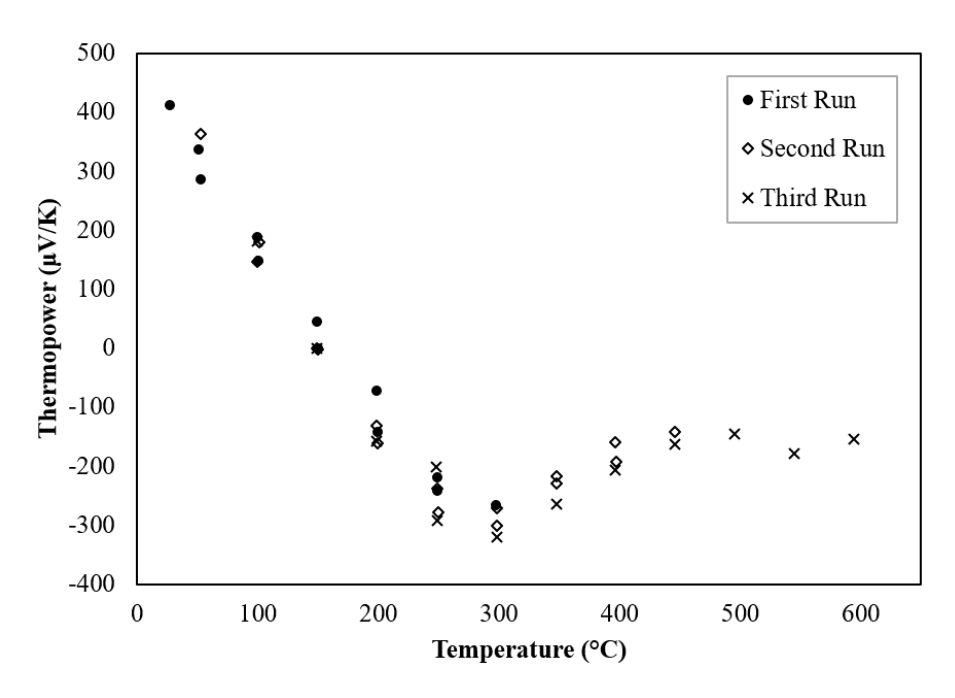


**Figure 4.16** Plot of thermopower versus temperature for 550 °C SPS sample, synthesized via sol-gel, run three times for comparison.

The results of the resistivity shown in **Figure 4.15** showed that the sample was more resistive than was typical for doped lead telluride samples. The Seebeck measurement shown in **Figure 4.16** showed that the intrinsic carriers began to take effect during the measurement near 200 °C. The high resistivity of the sample led to the investigation of the 2 % sodium doped PbTe separately from the 1:1 mol mixture of 2 % sodium doped PbTe and 2 % sodium doped CdTe. The unmixed sample was labeled as SKBM16\_SKSG36.

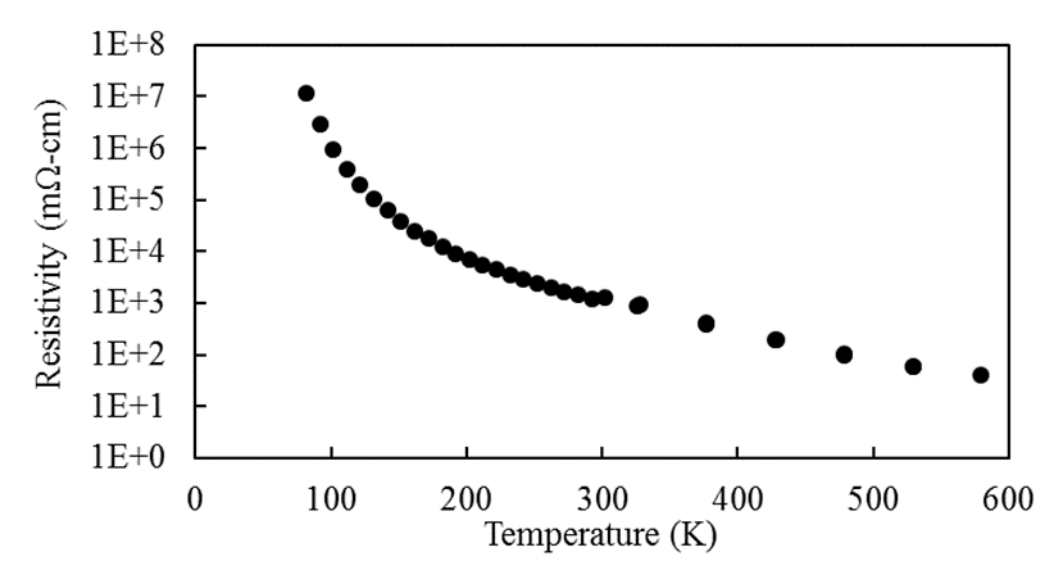


**Figure 4.17** Plot of resistivity versus temperature for SKBM16\_SKSG36 synthesized via sol-gel method.

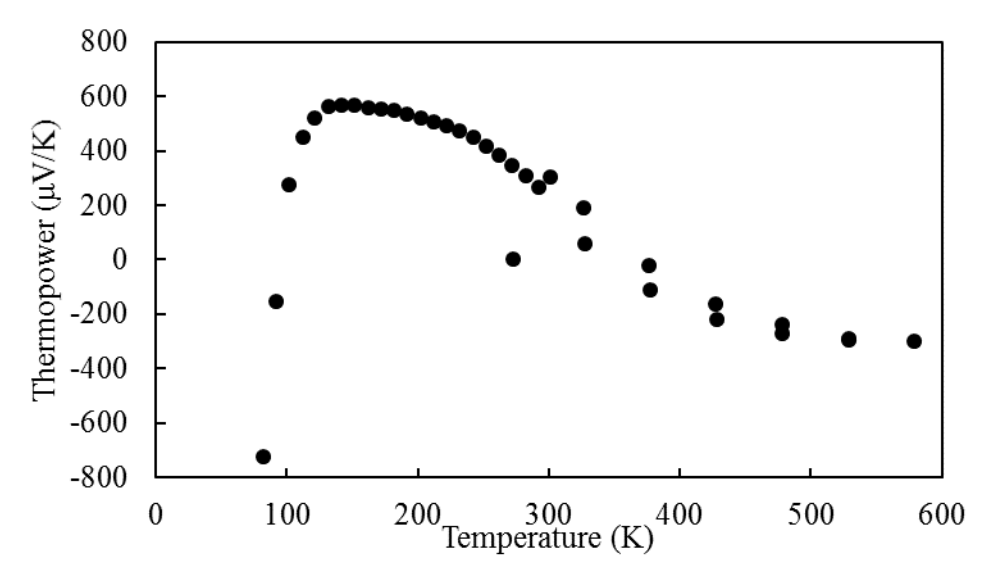


**Figure 4.18** Plot of thermopower versus temperature for SKBM16\_SKSG36 synthesized via sol-gel method.

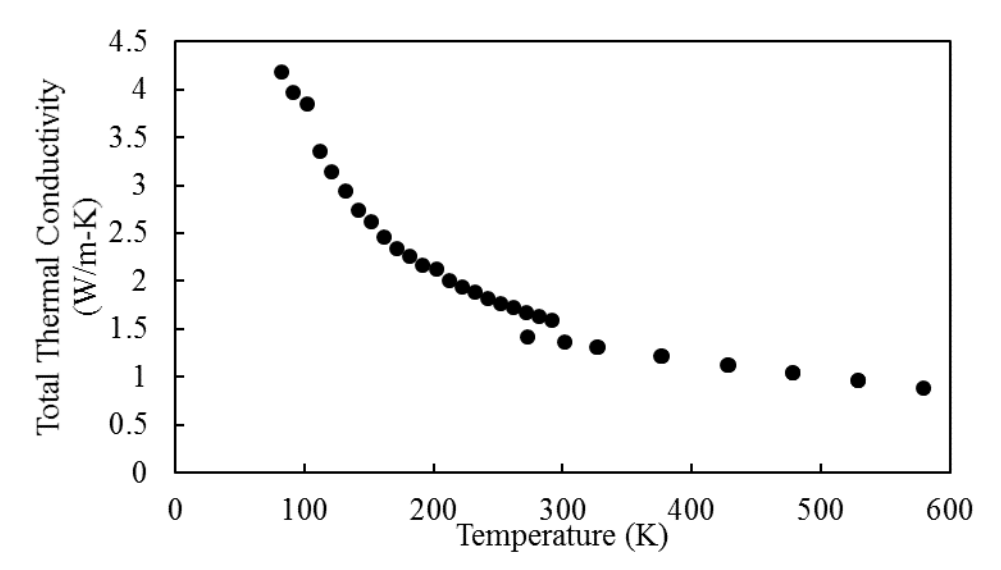


**Figure 4.19** Plot of total thermal conductivity versus temperature for SKBM16\_SKSG36 synthesized via sol-gel method.

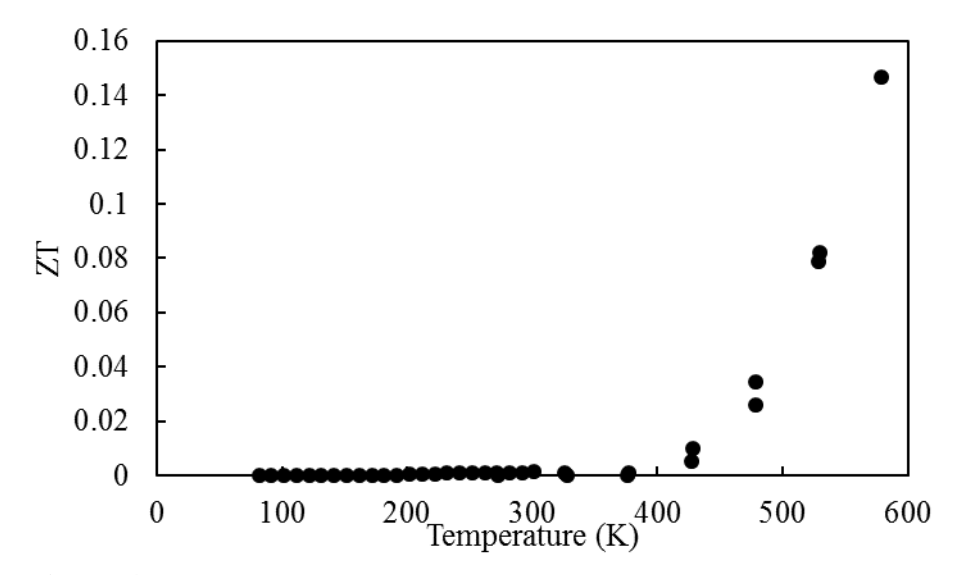


**Figure 4.20** Plot of ZT versus temperature for SKBM16\_SKSG36 synthesized via sol-gel method.

As shown in **Figure 4.17** the resistivity of the individual lead telluride remained higher than expected for a bulk doped lead telluride sample. It was determined that the synthetic method was to be called into question. Traditionally oxide materials are more resistive than doped semiconductors, it was speculated that the samples contained oxygen, which would not have been qualitatively or quantitatively noted in the characterization methods being used. To determine if the aqueous method being used was affecting the thermoelectric character of the samples, an inert method was selected for comparison.

### 4.9 Synthesis: Ampoule Method

All of the samples made by the ampoule method were synthesized in quartz ampoules due to the high melting temperatures of the materials. The quartz ampoules were carbon coated 2-3 times prior to use to ensure the samples would not stick to the quartz ampoule after heating. All samples were loaded into the ampoule in a glovebox under a nitrogen atmosphere. After being loaded in a glovebox, the ampoules were closed and attached to a Schlenk line. After being attached to the Schlenk line the ampoules were placed under vacuum, and flame sealed.

Lead telluride samples were made by adding 0.015 mol of Pb powder, and 0.015 mol of Te shot to a carbon coated quartz ampoule. The ampoule was then heated to 1050 °C over 6 hours, and held for 10 hours. After heated the ampoules were allowed to cool back to room temperature. After cooling the ampoules were placed back into the glovebox to be opened. An ingot was collected from the ampoule and ball milled to produce a powder for further analysis of the sample. All samples were milled at 500 rpm for at least 4 hours, some were milled longer if it was found that the ingot had not fully broken into powder. The same procedure was done for doped samples, 2 % of Na was added with the initial elements.

Cadmium telluride was attempted in the same ampoule method as the lead telluride. In a glovebox under nitrogen, 0.02 mol of Cd powder, and 0.02 mol of Te shot were added to a carbon coated

ampoule. The temperature for the ampoules were varied to 1100 °C, 1050 °C, and 900 °C. Unfortunately, the cadmium telluride ampoules at 1100 °C and 1050 °C all resulted in shattered or melted ampoules. At the lowest temperature the ampoules cracked and a mixed oxide compounds were formed.

#### 4.10 Results and Discussion

The PXRD pattern of PbTe by the ampoule method showed the sample was pure and could be used for further measurements. In addition to the undoped sample, a 2 % Na doped PbTe sample was synthesized for a comparison between the doped sample and an undoped PbTe sample. The undoped sample was labeled as SKBM18\_SKAmp23 and the 2 % sodium doped sample was labeled as SKBM11\_SKAmp15.

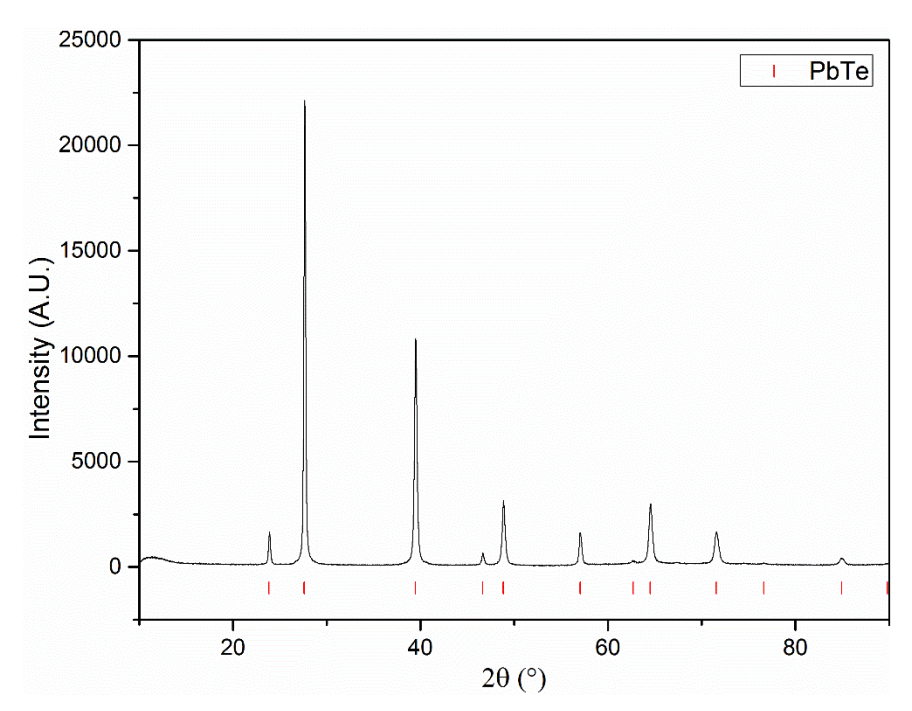


**Figure 4.21** PXRD pattern for an ampoule sample showing pure PbTe phase.

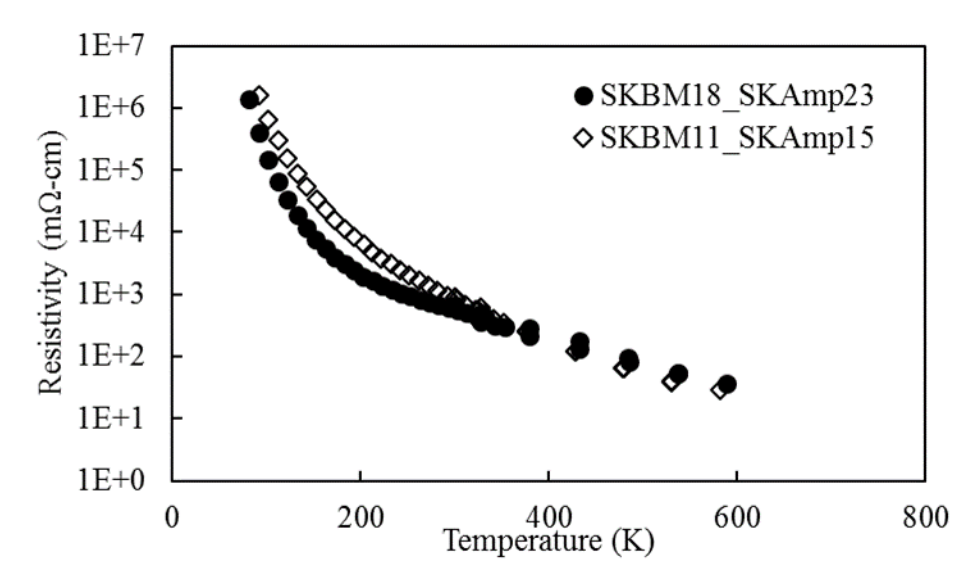


**Figure 4.22** Plot of resistivity versus temperature for SKBM18\_SKAmp23 and SKBM11\_SKAmp15 synthesized via ampoule method.

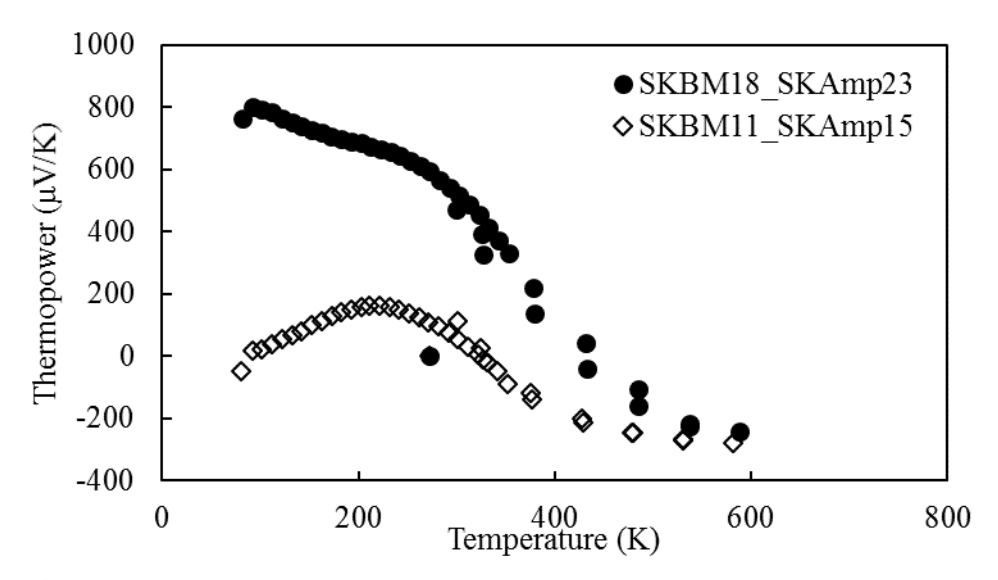


**Figure 4.23** Plot of thermopower versus temperature for SKBM18\_SKAmp23 and SKBM11\_SKAmp15 synthesized via ampoule method.

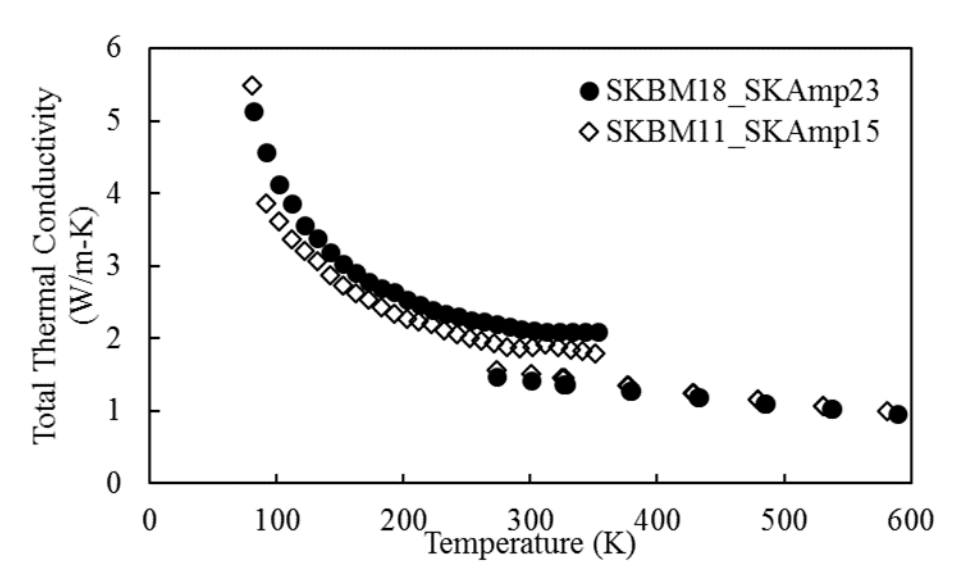


**Figure 4.24** Plot of total thermal conductivity versus temperature for SKBM18\_SKAmp23 and SKBM11\_SKAmp15 synthesized via ampoule method.

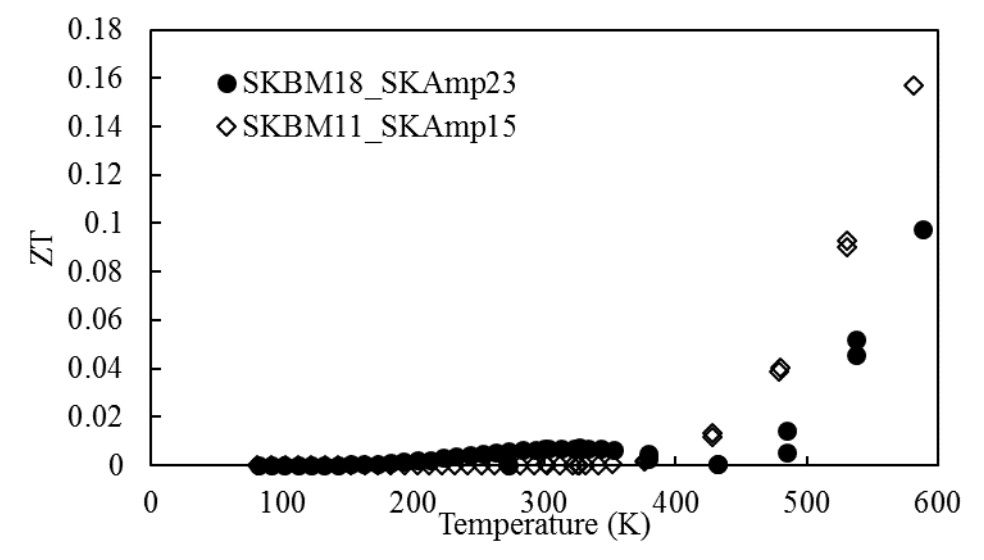


**Figure 4.25** Plot of ZT versus temperature for SKBM18\_SKAmp23 and SKBM11\_SKAmp15 synthesized via ampoule method.

The inert atmosphere method did not produce better results than the sol-gel method. The resistivity of the samples remained high and the thermopower still showed a sign change. It was determined that the dopant needed to be called into question and the carrier concentration should be measured via Hall effect measurement. Due to the brittleness of the samples it should be noted that the undoped SKBM18\_SKSKAmp23 sample broke and an additional sample was used, labeled as SKBM19\_SKAmp24.

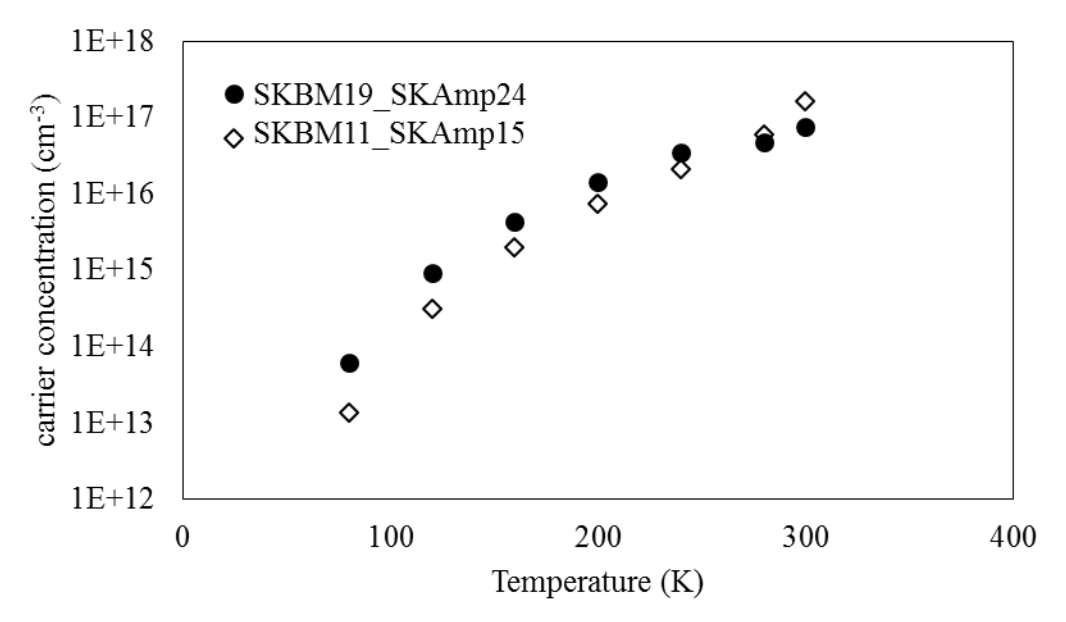


**Figure 4.26** Graph depicting carrier concentration versus temperature for both SKBM19\_SKAmp24 and SKBM11\_SKAmp15 synthesized via ampoule method.

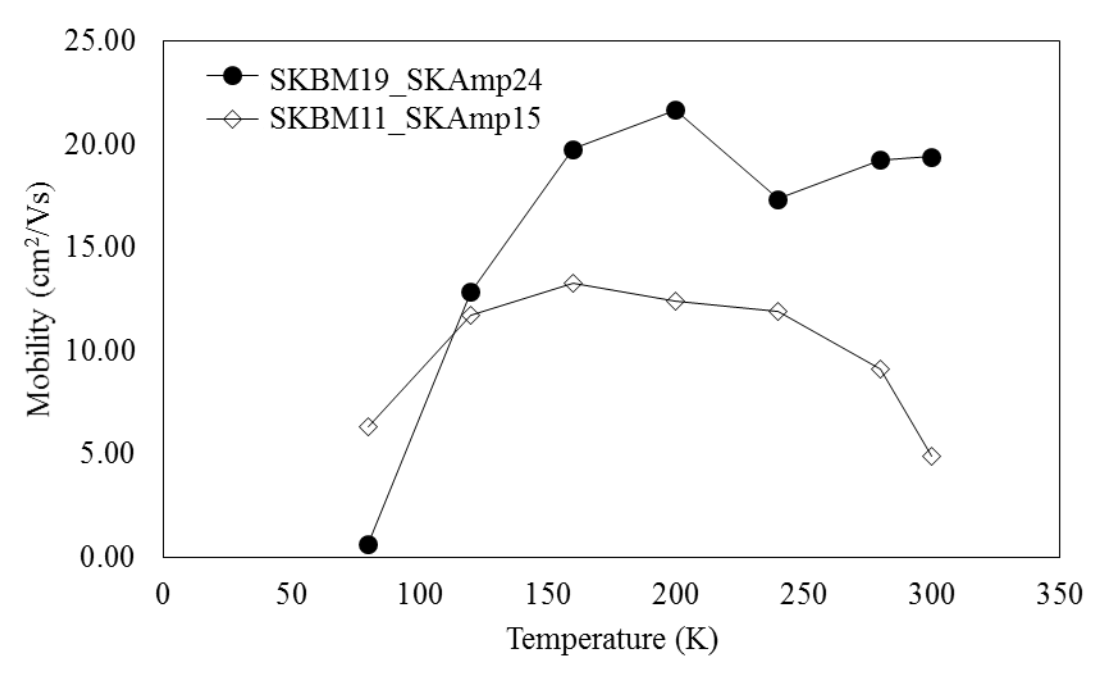


**Figure 4.27** Graph depicting carrier mobility versus temperature for both SKBM19\_SKAmp24 and SKBM11\_SKAmp15 synthesized via ampoule method.

The carrier concentration was lower than expected for a lead telluride sample doped with 2 % sodium. A 1 % doped PbTe sample has a mobility two orders of magnitude larger (in the 200 – 300 cm²/Vs range) than the measured mobility for either of the ampoule samples. The carrier concentration increased with temperature which is to be expected since as temperature increases electrons can become more thermally excited to move.

### 4.11 Conclusions for the Quantum-Confined Thermoelectric Project

Quantum-confined thin-films have shown an enhancement in both the Seebeck coefficient as well as the thermal conductivity providing an overall enhancement in the figure of merit. The goal of this project was to show an enhancement in the figure of merit of bulk materials through quantum-confinement of the materials. Several parameters were examined and it was determined two routes could be implemented to obtain the desired materials: one was core-shell nanoparticles, and the other two composite system made up of nanoparticles.

While SILAR offers a method of layering thin films it has yet to be modified and optimized for powdered materials. The binary crystal system formed verified that instead of an endotaxial growth of a shell on the core material, separate crystals of the desired shell material precipitated. The electromagnetic attraction of the ions to the core material proved to be problematic in creating the shell. It can be studied in greater detail the attraction of different ions for the endotaxial growth on particles without a potential as a guide for the ions. In a hurried attempt to show proof of concept, purchased micron-sized particles were utilized as cores, it is thought that this could have led to the binary system forming. This led to the search for a method to produce bulk quantities of nanoparticles to be utilized as core materials for SILAR. Due to separate crystals forming it was determined these samples would not proceed to thermoelectric measurements.

Co-precipitation offered a facile but slow method of making nanoparticles to be utilized in the SILAR method. Nanoparticles were synthesized in hopes of making endotaxial growth easier during SILAR. Nanoparticles were successfully synthesized using this method. The lead telluride particles were below the magnitude of the exciton Bohr radius. Unfortunately, at this time it was determined that the synthesis method was inadequate in terms of externally doping the samples. In addition to doping posing a problem, it was found large quantities of solvent (approximately one liter) was needed per 250 - 300 milligrams which would be problematic when scaling up for the 3 - 5 grams needed for thermoelectric measurements. Due to both of these difficulties these samples were never used for thermoelectric measurements.

While the first two methods used in the project were considered bottom up approaches where pieces of the project are used to build the desired sample, it was determined that trying a top down approach could give different perspective to the project. Ball milling is a technique known to decrease the particle size. Ball milling permitted for samples that were synthesized on the micron-

scale, doped, to be milled into nano sized particles. After just four hours of intermittent milling the samples were milled from micron-sized particles to nanoparticles for lead telluride, with the average size below the magnitude of the exciton Bohr radius. The next step in the project would be to determine a synthetic method that would produce bulk quantities of doped material to be milled from micron-sized particles to nanoparticles.

Sol-gel was sought as a method to produce bulk quantities of doped telluride materials. While sol-gel technique is typically used for oxide materials, it was used for the first time to provide a facile method of synthesizing pure lead telluride and cadmium telluride materials. Sol-gel method provided enough materials as well as a route for doping for these materials to have thermoelectric measurements done. Materials were made in doped bulk quantities to test the parameters of SPS for the materials to be pressed into dense pellets. These samples were then used for thermoelectric measurements. The resistivity measurement showed that these samples had higher resistivity than reported for lead telluride materials. It is supposed that the samples contained residual oxide from the synthetic technique, causing a high resistivity in the material. The thermopower measurement showed a change in dominate carrier, which implied a lack of doping. It was determined an inert atmosphere technique would allow a comparison to the sol-gel method.

Ampoule method was used as an inert atmosphere technique for a comparison to sol-gel. The results of the thermoelectric measurements were very similar to that of the sol-gel samples, and not agreeable to lead telluride samples produced by other groups. Hall effect measurements gave some insight into the lack of doping control in both synthetic methods. The doped ampoule sample shifted the temperature at which the intrinsic electron carriers dominate measurements to a lower temperature, implying that a semi-conductor was produced.

## 4.12 Future Work for the Quantum-Confined Thermoelectric Project

Providing proof of concept that quantum-confined bulk materials can show an enhancement in thermoelectric properties has provided several challenges. One of the many challenges has been doping of the materials. Quenching ampoules can provide better control over doping of materials. In addition to quenching ampoules, other dopants and concentrations could be investigated for a comparison. The sol-gel method also provided many challenges as it was implemented as a new technique for these materials. The reduction step of this technique was limited by using hydrogen gas and other reduction methods were never explored. Other dopants and concentrations could also be implemented to ensure doping of these materials.

Once these synthetic methods are optimized for producing bulk quantities of doped materials, the materials would be implemented for core materials in the SILAR method. This technique would then need optimization in attempt to showing quantum-confinement which would then be measured using DRIFTS. Finally, all samples would have thermoelectric measurements taken, to determine a correlation between the bulk quantum-confined materials and thermoelectric parameters.

REFERENCES

# REFERENCES

(1) Dughaish, Z. H. Lead Telluride as a Thermoelectric Material for Thermoelectric Power Generation. *Phys. B Condens. Matter* **2002**, *322* (1-2), 205–223.

# Chapter 5

Lanthanum Nickelate T`-Ln<sub>n+1</sub>Ni<sub>n</sub>O<sub>2n+1</sub> Family

## 5.1 Synthesis of La<sub>4</sub>Ni<sub>3</sub>O<sub>10</sub> and La<sub>4</sub>Ni<sub>2.8</sub>Cu<sub>0.2</sub>O<sub>10</sub>

Sol-gel was the method used to synthesize La<sub>4</sub>Ni<sub>3</sub>O<sub>10</sub> by adding 0.01 mol La<sub>2</sub>O<sub>3</sub>, 0.015 mol Ni(OH)<sub>2</sub> to an aqueous solution of 0.2 mol citric acid, and 4 mL of nitric acid. It was stirred until it became a transparent homogeneous solution, and then 10 mL of ethylene glycol was added. The solution is then allowed to stir for 24 hours, and then slowly heated on the hotplate until the solution becomes gel like. The gel was heated over six hours to 600 °C, held at temperature for 12 hours, and then allowed to cool to room temperature. The powder collected was then ground with a mortar and pestle and pelleted into 3/4" pellets. The pellets were placed into an alumina boat, and placed into a large tube furnace and heated over six hours to 1150 °C. The pellets were held at 1150 °C for 24-48 hours under flowing O<sub>2</sub>. The pellets were removed for intermittent grinding, and PXRD to determine if the final product had fully formed. The sample was heated for a total of 192 hours.

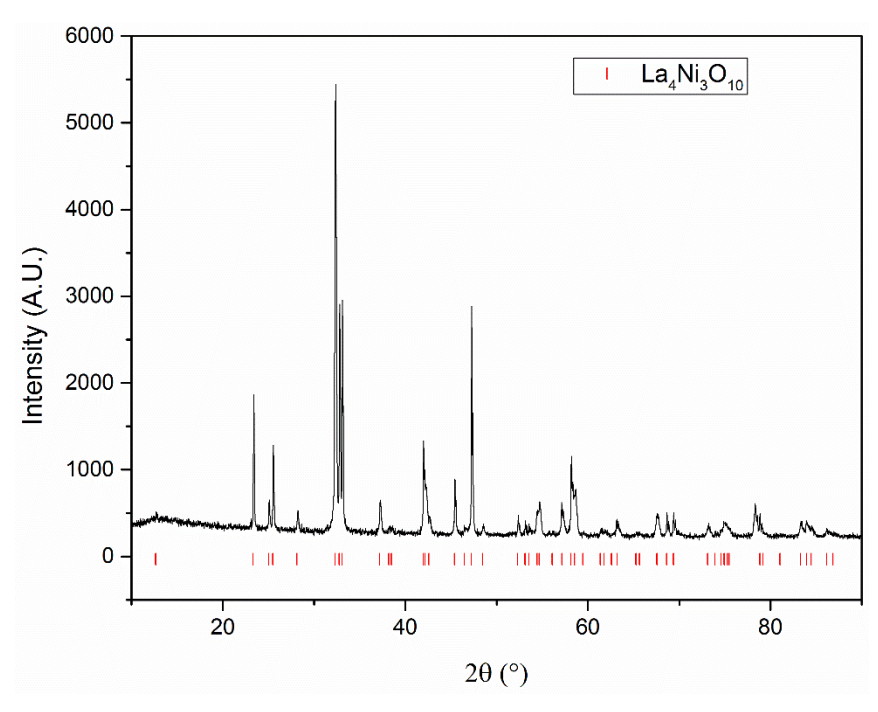


**Figure 5.1** PXRD pattern of  $La_4Ni_3O_{10}$  synthesized via sol-gel method.

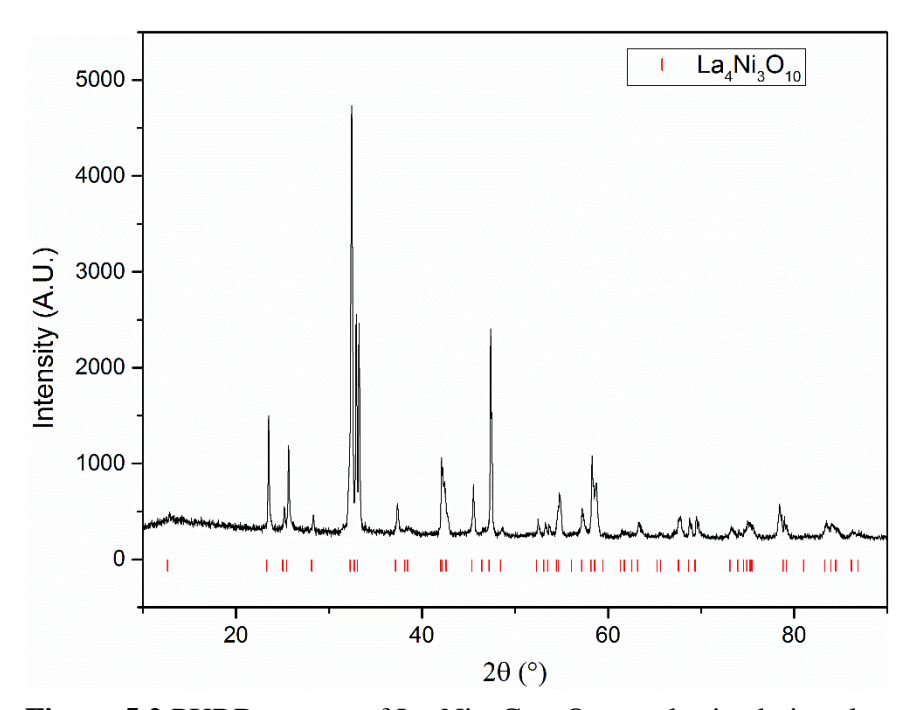
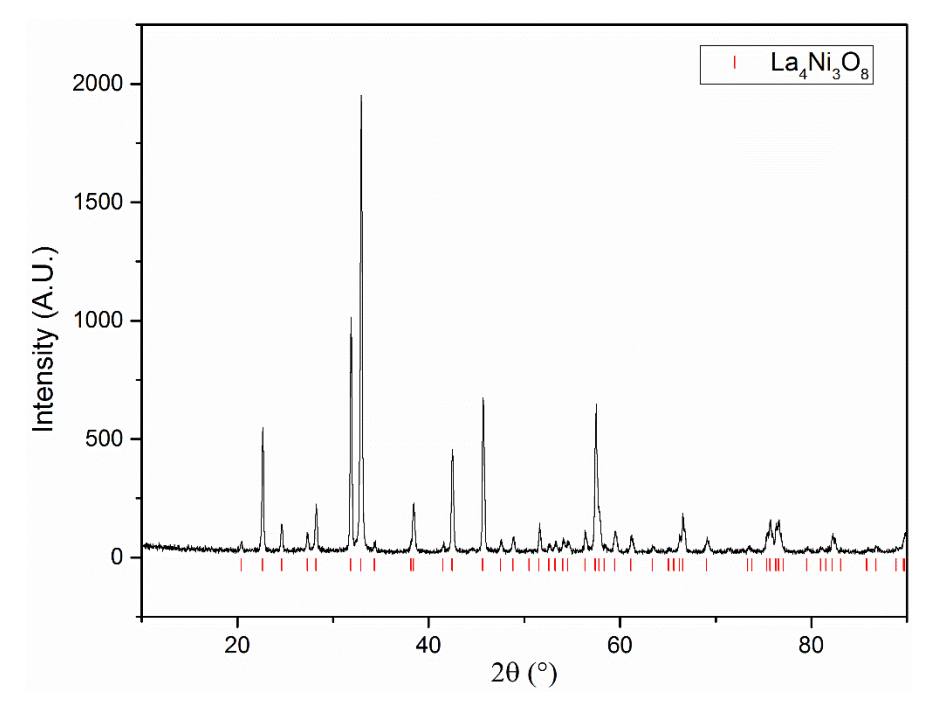


Figure 5.2 PXRD pattern of  $La_4Ni_{2.8}Cu_{0.2}O_{10}$  synthesized via solgel method.

# 5.2 Reduction to La<sub>4</sub>Ni<sub>3</sub>O<sub>8</sub> and La<sub>4</sub>Ni<sub>2.8</sub>Cu<sub>0.2</sub>O<sub>8</sub>

After pure phase  $La_4Ni_3O_{10}$  and  $La_4Ni_{2.8}Cu_{0.2}O_{10}$  were formed, reduction was done using  $H_2$  (g). Loose powder was placed in an alumina boat in between two alumina boats filled with  $P_2O_5$  and heated in a quartz tube to 325 °C for 60 h under a hydrogen atmosphere to reduce the samples to  $La_4Ni_3O_8$  and  $La_4Ni_{2.8}Cu_{0.2}O_8$  respectively.



**Figure 5.3** PXRD pattern of La<sub>4</sub>Ni<sub>3</sub>O<sub>8</sub> synthesized via sol-gel method and reduced using hydrogen gas.

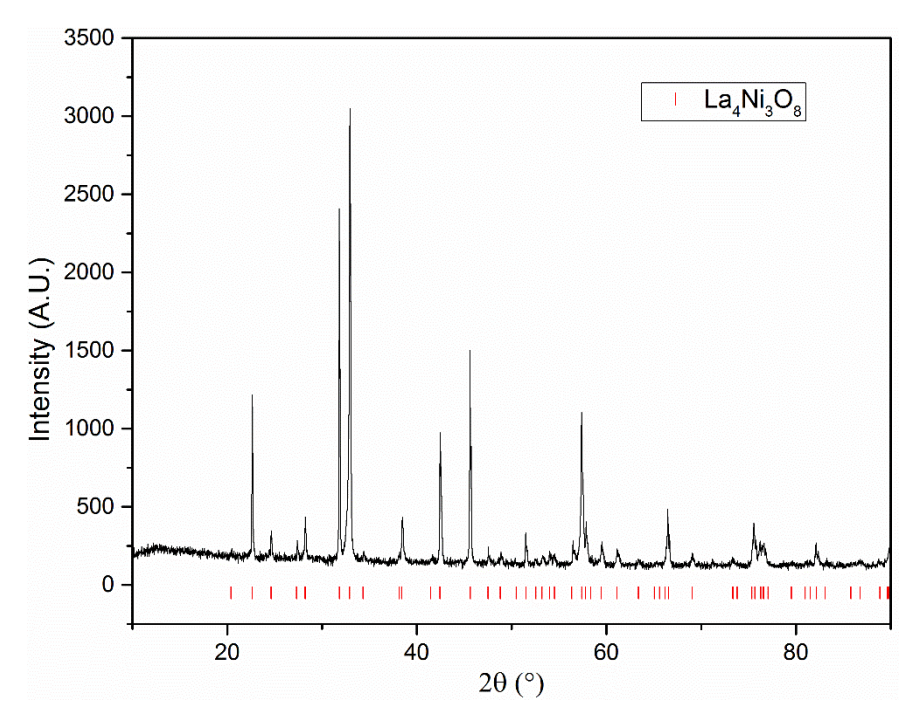


**Figure 5.4** PXRD pattern of La<sub>4</sub>Ni<sub>2.8</sub>Cu<sub>0.2</sub>O<sub>8</sub> synthesized via solgel method and reduced using hydrogen gas.

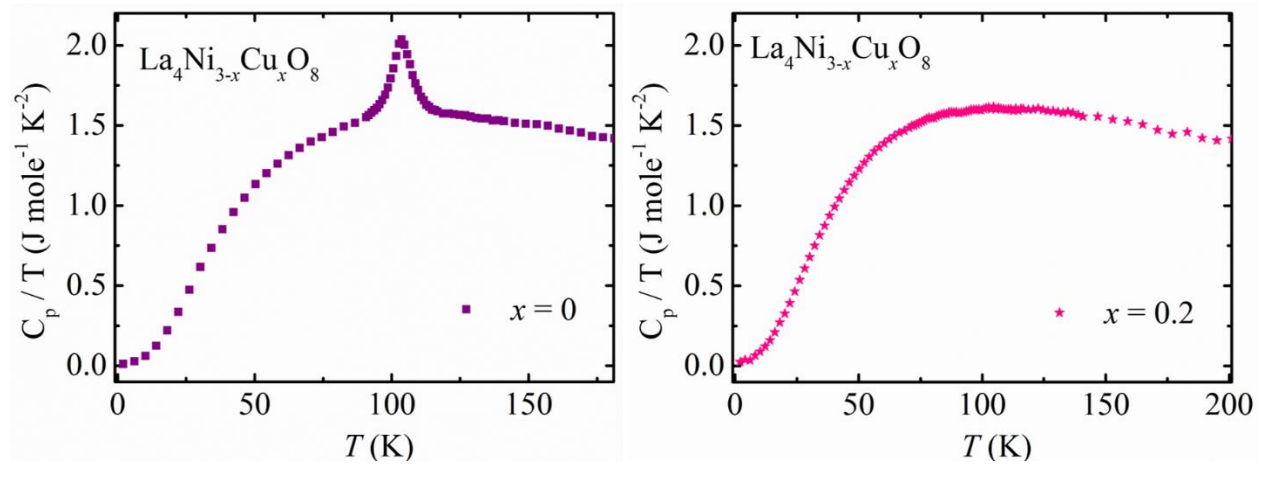


**Figure 5.5** Specific heat measurements for La<sub>4</sub>Ni<sub>3</sub>O<sub>8</sub> and La<sub>4</sub>Ni<sub>2.8</sub>Cu<sub>0.2</sub>O<sub>8</sub>, shown respectively. The 105 K phase transition due to charge ordering of the Ni<sup>1+</sup>/Ni<sup>2+</sup> metals, while this ordering becomes suppressed in the doped sample with Cu<sup>2+</sup> replacing the Ni in the square planar orientation.

# 5.3 Synthesis of LaNi<sub>1-x</sub>Cu<sub>x</sub>O<sub>3</sub>

Sol-gel was the method used to synthesize LaNiO<sub>3</sub> by adding 0.01 mol La<sub>2</sub>O<sub>3</sub>, 0.02 mol Ni(OH)<sub>2</sub> to an aqueous solution of 0.2 mol citric acid, and 4 mL of nitric acid. It was stirred until it became a transparent homogeneous solution, and then 10 mL of ethylene glycol was added. The solution is then allowed to stir for 24 hours, and then slowly heated on the hotplate until the solution becomes gel like. The gel was heated over six hours to 450 °C, held at temperature for 12 hours, and then allowed to cool to room temperature. The powder collected was then ground with a mortar and pestle and pelleted into 3/4" pellets. The pellets were placed into an alumina boat, and placed into a large tube furnace and heated over six hours to 850 °C. The pellets were held at 850 °C for 24-48 hours under flowing O<sub>2</sub>. The pellets were removed for intermittent grinding, and PXRD to determine if the final product had fully formed. The sample was heated for a total of 192 hours. After the pure sample was formed the sample was stored in a vial placed in a glovebox under a N<sub>2</sub> atmosphere.

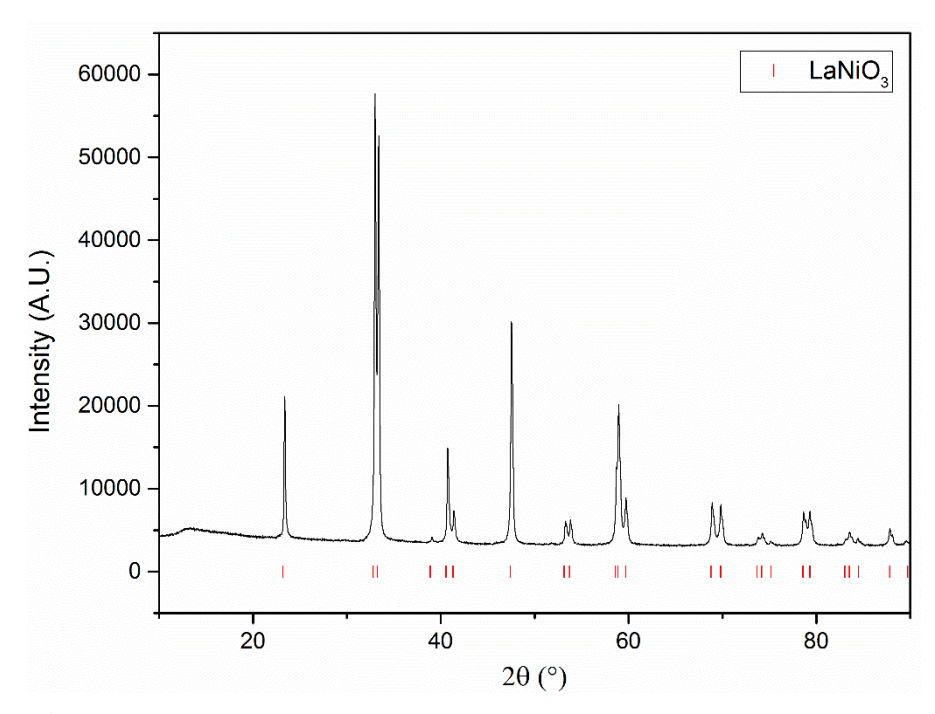
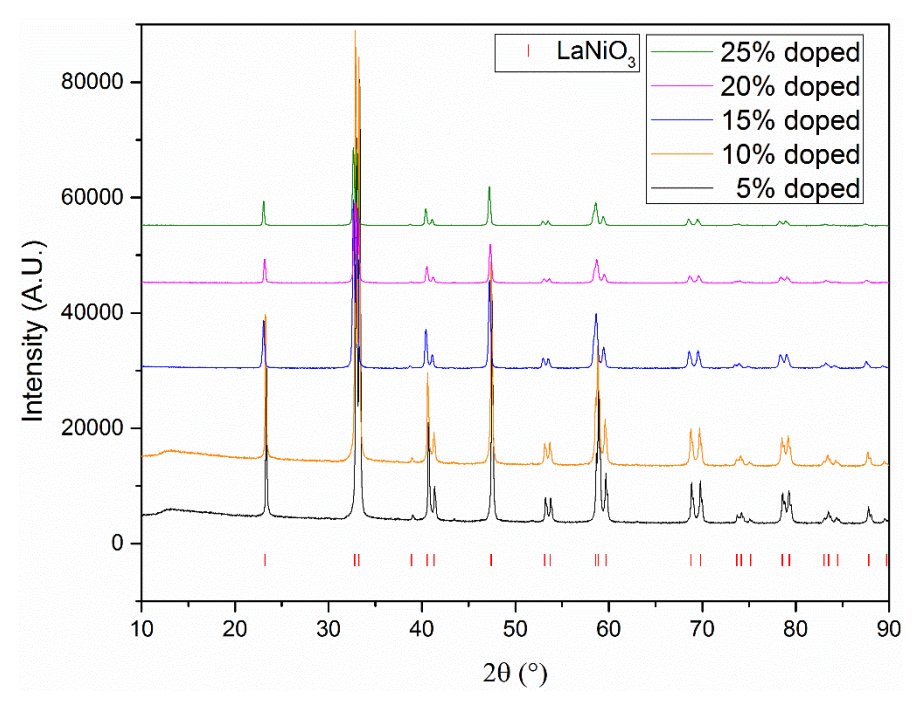


Figure 5.6 PXRD pattern of LaNiO $_3$  synthesized via sol-gel method.

The same procedure was followed for the synthesis of  $LaNi_{1-x}CuxO_3$  where x = 0.05, 0.10, 0.15, 0.20, and 0.25. The samples were heated for a combined total of 216 hours, 216 hours, 192 hours, 240 hours, and 240 hours respectively.



**Figure 5.7** PXRD pattern of  $LaNi_{1-x}Cu_xO_3$  where  $x=0.05,\,0.10,\,0.15,\,0.20,$  and 0.25 synthesized via sol-gel method.

Each compound of LaNi<sub>1-x</sub>Cu<sub>x</sub>O<sub>3</sub> where x = 0.00, 0.05, 0.10, 0.15, 0.20, and 0.25 was successfully synthesized using first the sol-gel method and then the ceramic method. After pure phase samples were synthesized, EXPO2014 software package was used to determine the cell parameters using TREOR for each sample. These are summarized in **Table 5.1**.

**Table 5.1** Summary of cell parameters and volumes for hexagonal LaNi<sub>1-x</sub>Cu<sub>x</sub>O<sub>3</sub> series.

Doping (x)	a (Å)	b (Å)	c (Å)	a (°)	β (°)	γ (°)	Volume (Å <sup>3</sup> )
0.00	5.44417	5.44417	13.10603	90	90	120	336.4
0.05	5.46470	5.46470	13.14890	90	90	120	340.0
0.10	5.46067	5.46067	13.13706	90	90	120	339.3
0.15	5.46830	5.46830	13.15177	90	90	120	340.6
0.20	5.47124	5.47124	13.16567	90	90	120	341.3
0.25	5.47497	5.47497	13.16925	90	90	120	341.9

The volume was plotted against the amount of dopant to determine if a trend was present, signifying the doping of the cell. A general increase was seen as an increase in dopant with the exception of 5 % doping.

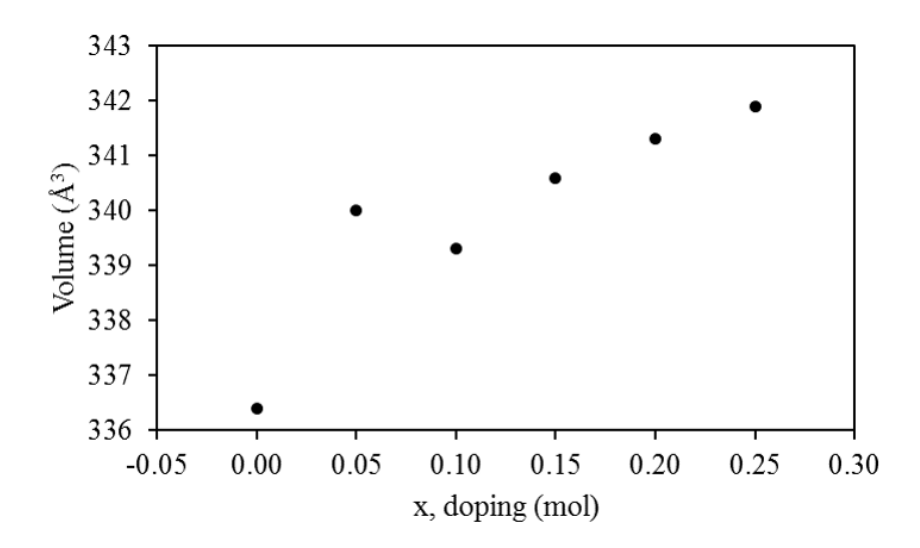


**Figure 5.8** Plot of volume ( $\mathring{A}^3$ ) versus x, dopant in LaNi<sub>1-x</sub>Cu<sub>x</sub>O<sub>3</sub> series.

### 5.4 Reduction of LaNi<sub>1-x</sub>Cu<sub>x</sub>O<sub>3</sub>

The samples were further processed by reducing them using a solvothermal method established by a previous researcher, Dr. Blakely. LaNi<sub>1-x</sub>Cu<sub>x</sub>O<sub>3</sub> and 30 mol equivalents of sodium hydride (NaH) were ground with a mortar in pestle in a glovebox under nitrogen atmosphere. The mixture was then loaded into a 45 mL Parr autoclave with 20 mL of anhydrous pentane and sealed while in the glovebox. The autoclave was then removed and placed into an oven, heated to 200 °C and held for 10 days (240 hours). Previously, Blakely reported using this method resulted in >95 % LaNiO<sub>2</sub> and <5 % La<sub>2</sub>Ni<sub>2</sub>O<sub>5</sub>. After heating the autoclaves were cooled to room temperature and returned to the glovebox. Upon being opened in the glovebox the samples were washed with anhydrous isopropyl alcohol to remove any sodium hydroxide formed as well as the excess of NaH unused. After drying the samples were PXRD using a dome sample holder, which was loaded in a glovebox.

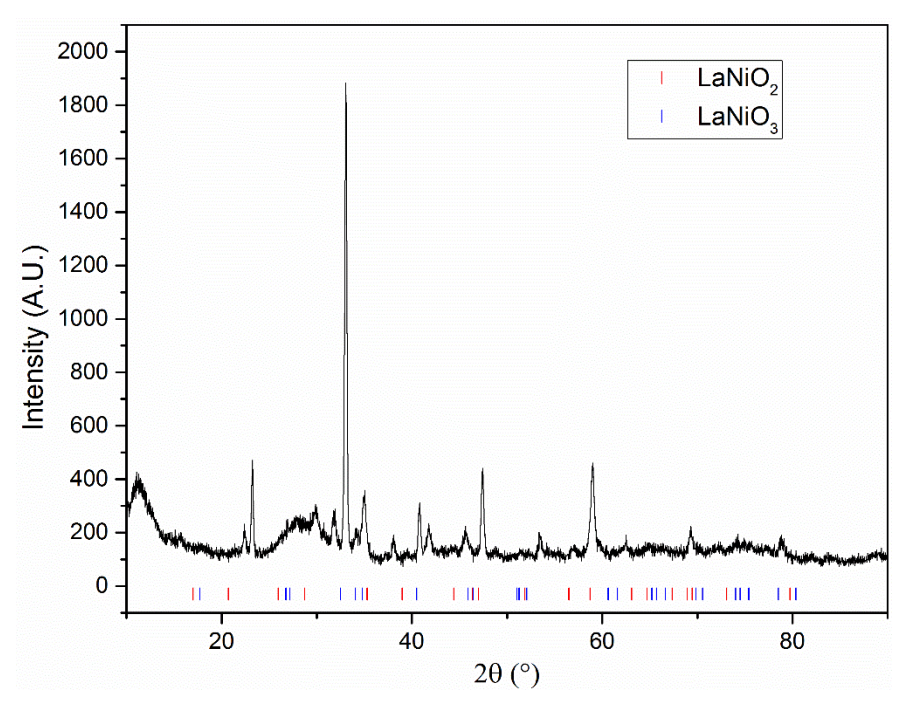


**Figure 5.9** PXRD pattern of  $LaNi_{0.95}Cu_{0.05}O_3$  reduced using the solvothermal method.

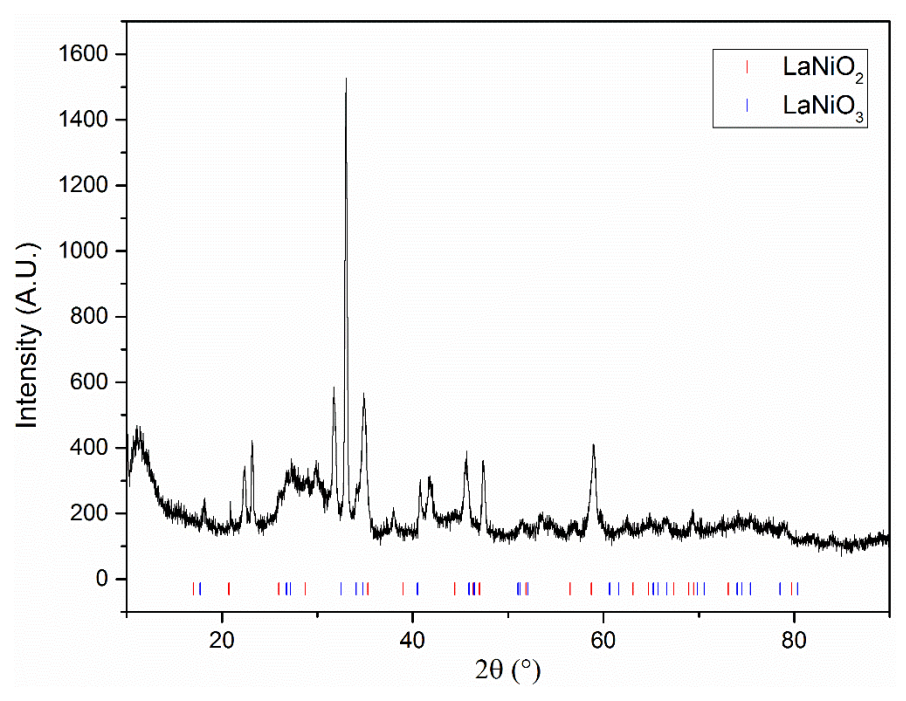


**Figure 5.10** PXRD pattern of  $LaNi_{0.90}Cu_{0.10}O_3$  reduced using the solvothermal method.

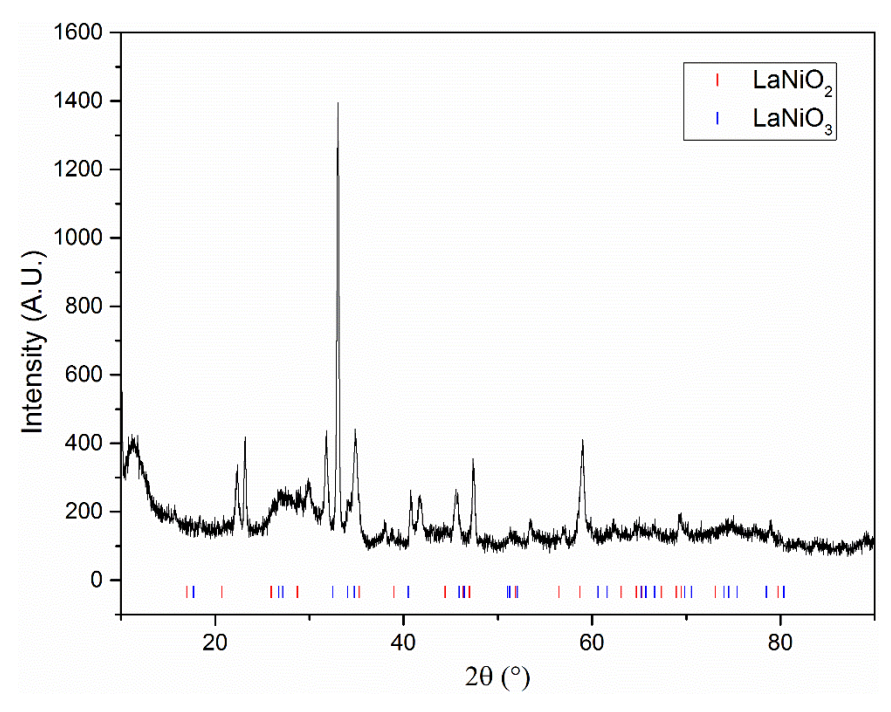


**Figure 5.11** PXRD pattern of  $LaNi_{0.85}Cu_{0.15}O_3$  reduced using the solvothermal method.

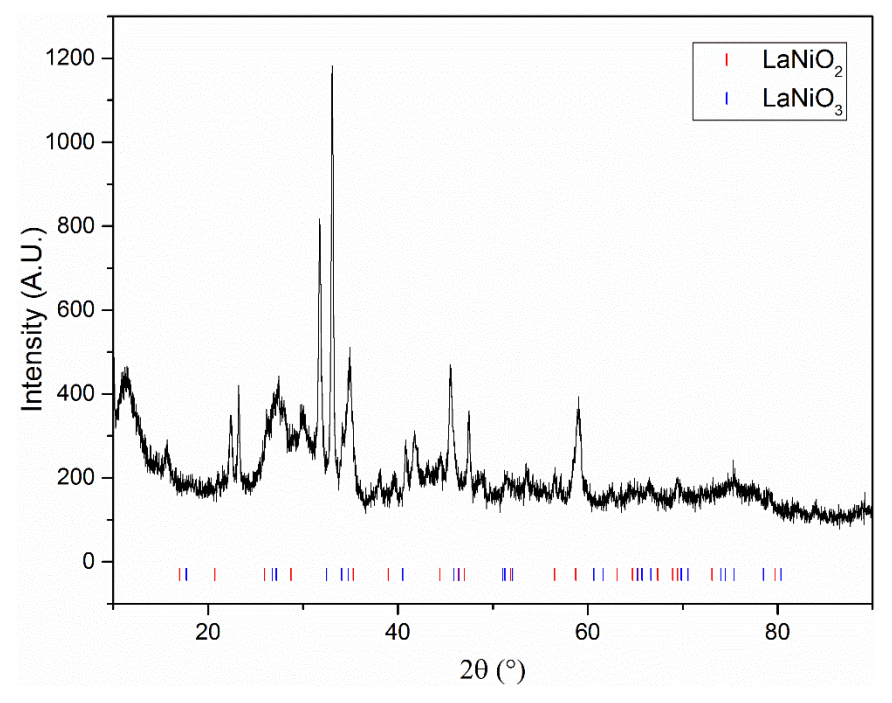


**Figure 5.12** PXRD pattern of  $LaNi_{0.80}Cu_{0.20}O_3$  reduced using the solvothermal method.

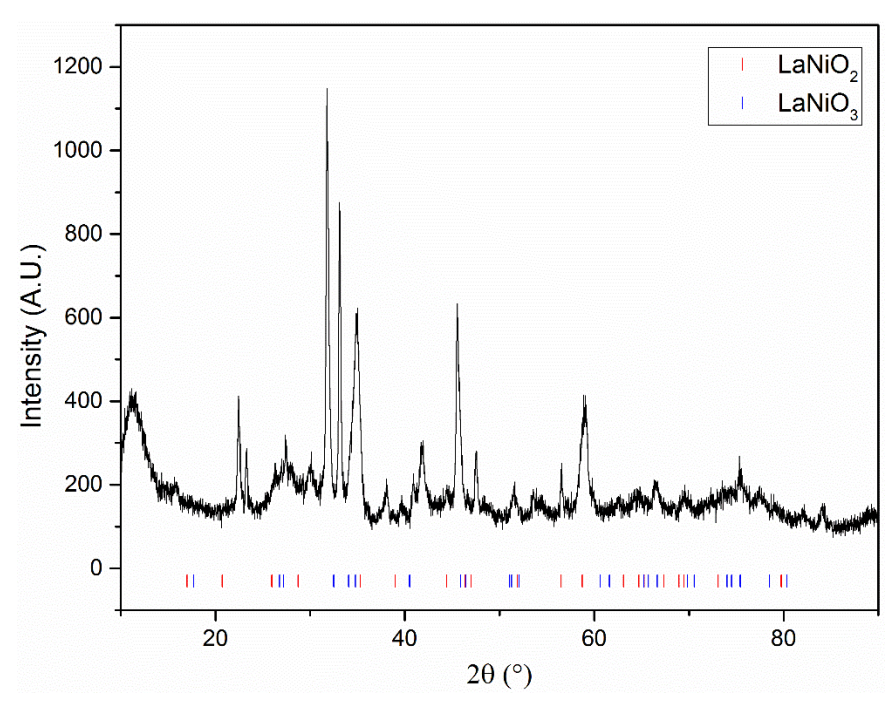


**Figure 5.13** PXRD pattern of  $LaNi_{0.75}Cu_{0.25}O_3$  reduced using the solvothermal method.

All of the reduced samples showed mix phases of LaNiO<sub>3</sub> and LaNiO<sub>2</sub>, with the 5 % doped sample being the only sample with more LaNiO<sub>2</sub> phase. After powder x-ray diffraction measurements were carried out, TOPAS software package was used to determine the cell parameters for each sample. The results of this are summarized in **Table 5.2**.

Table 5.2 Summary of cell parameters and volumes for tetragonal LaNi<sub>1-x</sub>Cu<sub>x</sub>O<sub>2</sub> series.

Doping (x)	a (Å)	c (Å)	$\alpha = \beta = \gamma$ (°)	Volume (ų)
0.05	3.97090	3.36740	90	53.10
0.10	3.98510	3.23460	90	51.74
0.15	4.05330	3.12190	90	51.29
0.20	4.03700	3.14100	90	51.19
0.25	3.99870	3.11246	90	49.77

The volume was plotted against the amount of dopant to determine if a trend was present, signifying the doping of the cell. A general decrease was seen as an increase in dopant with the exception of 20 % doping. The decrease in volume with an increase with dopant was a curious trend observed for these samples. It could be speculated that the decrease in volume is due to the Cu atoms disrupting the Ni-Ni metal interactions between layers, since the a parameter was increasing with the doping, and the c parameter was decreasing. Further investigation into these samples is needed to determine correct cause of the volume decrease.

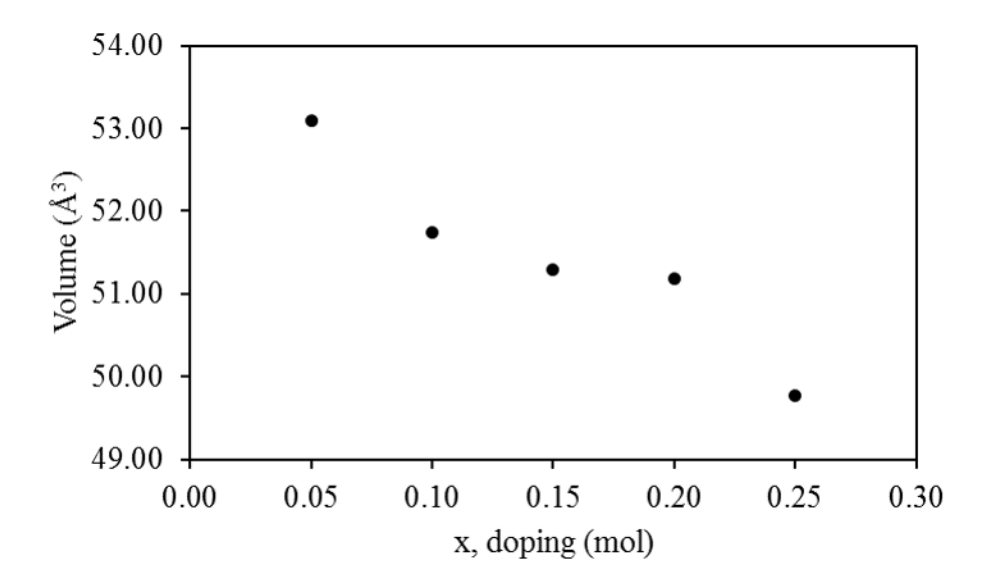


**Figure 5.14** Plot of volume (Å<sup>3</sup>) versus x, dopant in LaNi<sub>1-x</sub>Cu<sub>x</sub>O<sub>2</sub> series.

It should be noted that both the 20 % and 25 % samples had large errors associated with the cell parameter calculation due to the large amount of LaNiO3 phase present in each sample. The cell parameters were included to show that a trend was present in all five samples, however, purer samples will give more accurate cell parameters.

# 5.5 Conclusion for the T`-Lanthanum Nickelate Project

The La<sub>4</sub>Ni<sub>3</sub>O<sub>10</sub> and La<sub>4</sub>Ni<sub>2.8</sub>Cu<sub>0.2</sub>O<sub>10</sub> were both synthesized through traditional sol-gel and ceramic techniques. The materials were able to be reduced by low temperature heating in hydrogen gas, to La<sub>4</sub>Ni<sub>3</sub>O<sub>8</sub> and La<sub>4</sub>Ni<sub>2.8</sub>Cu<sub>0.2</sub>O<sub>8</sub>. The materials were measured for specific heat, while La<sub>4</sub>Ni<sub>3</sub>O<sub>8</sub> is

known for its phase transition near 105 K, the doped sample, La<sub>4</sub>Ni<sub>2.8</sub>Cu<sub>0.2</sub>O<sub>8</sub> suppresses this transition by replacing the Ni<sup>1+</sup>/Ni<sup>2+</sup> with Cu<sup>2+</sup> in square planar coordination.

Traditional synthetic methods allowed for the doped series of LaNi<sub>1-x</sub>Cu<sub>x</sub>O<sub>3</sub> to be successfully synthesized for the first time. The cell parameters showed an agreeable trend, increasing with increasing dopant, other than the 5 % doped LaNiO<sub>3</sub>. A repeat of this experiment would determine if the 5 % doped compound is truly an outlier or if it was error in synthesis and calculation. A new method of low temperature solvothermal reduction allowed for an attempt to reduce the doped series, producing Cu doped LaNiO<sub>2</sub> for the first time. The 5 % doped compound showed a majority phase of LaNiO<sub>2</sub>, however, LaNiO<sub>3</sub> was still a prominent phase. The 10 % - 25 % doped compounds showed a majority phase of LaNiO<sub>3</sub> and a minor phase of LaNiO<sub>2</sub>. The cell parameters for the LaNi<sub>1-x</sub>Cu<sub>x</sub>O<sub>2</sub> series showed interesting results in respect to the decrease in volume with increase in dopant. The trend could be attributed to the Cu atoms disrupting the Ni-Ni metal interactions between layers. While the 20 % and 25 % dopant cell parameters contained a large error due to small amounts of LaNiO<sub>2</sub> phase being present, the 25 % continued the volume trend.

## 5.6 Future Work on the T`-Lanthanum Nickelate Project

The La<sub>4</sub>Ni<sub>3-x</sub>Cu<sub>x</sub>O<sub>8</sub> samples have been submitted for further characterization using both  $\mu$ -SR and solid state NMR measurements. These measurements will provide more insight as to how the materials electrons are correlating, and can provide more information as to the characteristics of these materials.

Further characterization of LaNi<sub>1-x</sub>Cu<sub>x</sub>O<sub>2</sub> series of compounds is necessary for insight to this trend, and more information about this series. While not high phase purity samples, they give promise to the successful synthesis of pure phase LaNi<sub>1-x</sub>Cu<sub>x</sub>O<sub>2</sub> series, which could provide insight as to whether d9 metal infinite square planar layers is the key to high temperature superconductivity.

REFERENCES

# REFERENCES

(1) Blakely, C. K. Ph.D. Dissertation, Michigan State University, 2014.

#### Chapter 6

#### Conclusions

The overall goal of these projects was to enhance two areas of science, thermoelectrics and high temperature superconductors, by means of low dimensionality. Low dimensionality is not a new notion to the sciences, nevertheless, it has not been exploited to the fullest in all areas. Low dimensionality took on different roles for each project, for thermoelectrics it was nanoparticles and quantum-confined materials, while for T`-lanthanum nickelates it was infinite layers in the unit cell of the material. While the goal for each project was different, the route of achieving success lies in the dimensionality of the materials while on varying scales.

The overall objective of the thermoelectric project was to improve bulk thermoelectric materials through quantum-confinement. While this objective still needs completing, several achievements came from the project. A novel facile method was implemented for the synthesis of bulk telluride materials. For the first time pure telluride materials were synthesized using the sol-gel method. The SPS parameters for the entirety of the project were optimized for future use. It was also determined that DRIFTS could be implemented in determining if the bulk materials were quantum-confined. These successes will aid in the exploration for proof of concept; that like thin-films, bulk thermoelectrics can be enhanced through quantum-confinement.

The objective of the T`-lanthanum nickelates project was to determine the influence of infinite layers in the materials. While there have been many who have claimed to have made analogues to the high temperature superconducting cuprates, none have both isoelectronic and isostructural to the materials. The d9 Ni<sup>1+</sup> square planar layers in the T`-lanthanum nickelate family of materials is both isoelectronic and isostructural to the Cu<sup>2+</sup> infinite-layer compounds. The project is not without difficulty as synthesizing the metastable phase has been challenging throughout several

decades. To achieve the metastable phase of pure LaNiO<sub>2</sub> a new topotactic oxygen deintercalation method needed to be implemented. A solvothermal reduction of the parent compound, LaNiO<sub>3</sub>, allowed for the successful synthesis of a new set of compounds, LaNi<sub>1-x</sub>Cu<sub>x</sub>O<sub>2</sub> (x = 0.05, 0.10, 0.15, 0.20, and 0.25). The method of reduction needs optimizing for these materials, nonetheless, once optimized the investigation of these materials could provide a model for monovalent transition metal d9 ion.

The pursuit of low dimensionality in materials is not without challenges, nevertheless, these challenges have helped to find innovative synthetic methods. The low dimensionality of materials allows for the exploit of unique properties not present in the higher dimensional material. These unique properties could be the crucial to enhancing thermoelectrics for industrial use as well as the theory behind high temperature superconductors.